The energy scale of the 3-flavour Lambda parameter

DISSERTATION

zur Erlangung des akademischen Grades
doctor rerum naturalium
(Dr. rer. nat.)
im Fach Physik
Spezialisierung: Theoretische Physik

eingereicht an der
Mathematisch-Naturwissenschaftlichen Fakultät
der Humboldt-Universität zu Berlin

von
Herrn Dipl.-Phys. Mattia Bruno

Präsident der Humboldt-Universität zu Berlin
Prof. Dr. Jan-Hendrik Olbertz

Dekan der Mathematisch-Naturwissenschaftlichen Fakultät
Prof. Dr. Elmar Kulke

Gutachter/innen:
1. Prof. Dr. Rainer Sommer
2. Prof. Dr. Giancarlo Rossi
3. Prof. Dr. Michael Müller-Preussker

Tag der mündlichen Prüfung: 24/07/2015

Abstract

In lattice computations all dimensionful observables have to be expressed in units of a reference scale and its determination is often the first step before proceeding to other quantities.

In this thesis we describe the scale setting strategy for a new set of large-volume ensembles generated within the CLS effort. The simulations have been carried out including up, down and strange quark fields, discretized a là Wilson and following the $O(a)$-improvement program. The gauge field dynamics is implemented with the improved Lüscher-Weisz action.

To overcome the freezing of topology in simulations at small lattice spacings, open boundary conditions in the time direction have been adopted, together with twisted-mass reweighting, a technique to regularize and stabilize the fermionic contributions in the infrared region.

In this thesis we discuss their implications on mesonic spectral quantities. We compute the lattice spacings, for our four values of β, using the pseudo-scalar decay constants, extracted in the presence of open boundary conditions. In addition to that, we determine the observable t_0 and extrapolate it to the continuum.

Zusammenfassung

Alle dimensionsbehafteten Gitter-QCD-Observablen müssen in Einheiten einer Referenzskala ausgedrückt werden und die Bestimmung dieser ist häufig der erste Schritt in der Berechnung anderer Observablen.

In dieser Arbeit beschreiben wir eine *scale setting*-Strategie für eine neue Satz an Ensembles mit großem Volumen, die von CLS generiert worden sind. Die Simulationen enthalten up, down und strange $O(a)$-verbesserte Wilson-Fermionenfelder. Die Eichfelddynamik ist mit Lüscher-Weisz-Wirkung implementiert.

Um das *freezing* der Topologie bei kleinen Gitterabständen zu überwinden, wurden offene Randbedingungen in Zeitrichtung verwendet. Außerdem wurde *twisted mass reweighting* eingesetzt, eine Technik, um die Fermionbeiträge in der Infrarotregion zu stabilisieren und zu regularisieren.

In dieser Arbeit diskutieren wir deren Auswirkungen auf mesonische Spektralgrößen. Wir berechnen die Gitterabstände für unsere vier β Werte unter Verwendung der pseudoskalaren Zerfallskonstanten, die wir aus den Simulationen mit offenen Randbedingungen extrahieren.

Außerdem bestimmen wir die Observable t_0 und extrapolieren sie zum Kontinuum.

Contents

Introduction

The laws of physics are described by four fundamental pieces: electromagnetic and weak interactions, the strong force and gravity. In particular Quantum Field Theories have been experimentally confirmed (within the ranges of energies so far explored) to be the best descriptive and predictive theories for particle physics. In some sense, QFTs blend together the laws of Quantum Mechanics and Special Relativity and open a new window in the understanding of natural phenomena in terms of symmetries. Intrinsic properties of particles are now understood as the behavior under transformations of some symmetry group. For instance, a relativistic theory must possess Lorentz invariance and depending on the way the various fields transform under such symmetry, they have different properties, such as the spin number. Electroweak and strong interactions are described in terms of local symmetries, the gauge symmetries, realized by adjoint representations of specific Lie Groups. Global symmetries, such as chiral or flavor transformations, constrain the spectrum of hadrons.

Since the physics of accelerators and colliders began, a whole zoo of particles has been discovered. Their interactions and properties are described by the so-called Standard Model, a renormalizable and local QFT, with $U(1) \times SU(2) \times SU(3)$ gauge symmetry, which provides an excellent description of the fundamental forces, gravity excluded. It depends on 3 gauge couplings (one for each group) which determine the strength of the corresponding forces, 3 lepton and 6 quark masses. In the SM, neutrinos are assumed to be massless. Instead, recent discoveries on neutrino oscillations demonstrated that they do have masses, pointing to physics beyond the Standard Model. Nevertheless they also set bounds on these masses, that confirmed that the massless approximation for neutrinos is adequate in high-energy processes.

The last fundamental component of the SM is the Brout-Englert-Higgs boson [1, 2, 3], which has been finally discovered by the LHC experiment (ATLAS and CMS [4, 5]). The Higgs mechanism gives masses to the $W^{\pm}$ and Z bosons without violating gauge invariance, and its corresponding scalar field introduces two additional parameters in the SM: the Higgs mass and the quartic coupling (whereas the fermion masses can be replaced by Yukawa couplings between quarks/leptons and the Higgs field).

Hence a fundamental question, which still remains, despite all the open problems beyond the SM (e.g. explanation of dark matter), concerns the nature of these free parameters. In particular the gauge coupling constants show a hierarchy in the strength, efficiently described by their names, which puts Quantum Chromodynamics, the theory of strong interactions (given by the $SU(3)$ gauge symmetry), under a particular light.

The present work is focused on the study of this peculiar coupling constant, within the framework of QCD alone.

In Euclidean space-time, QFTs can be defined by correlations functions. Given an action S depending on a set of different fields ϕ, an observable O (we omit possible additional dependences on kinematic variables) in the path integral formalism, is obtained according to

$$\langle O \rangle = \mathcal{Z}^{-1} \int [\mathcal{D}\phi] O e^{-S[\phi]} , \quad \mathcal{Z} = \int [\mathcal{D}\phi] e^{-S[\phi]} .$$

Once all the n-point correlators are known, the theory may be considered to be solved. In some peculiar cases (e.g. Conformal field theories in 2-D) additional symmetries or lower dimensions help to constrain the Green's functions and analytically compute some of them.

In perturbation theory, the interaction term of the action in the path integral is expanded in the coupling constant and observables become "asymptotic series" of the form (assuming a certain dependence on the coupling)

$$\langle O \rangle = \bar{g}^2 O_1 + \bar{g}^4 O_2 + O(\bar{g}^6) .$$

Such expansions are valid if the (renormalized) coupling $\bar{g}$ is small enough.

A very important feature of non-abelian Yang-Mills theories is *asymptotic freedom*: the coupling constant becomes small at very high energies, where the theory becomes weakly-interacting. Therefore, perturbation theory is valid only in some range of energies $[\mu_0, \infty)$, with $\mu_0 \approx 10\,\mathrm{GeV}$, where it matches experiments for scattering processes. At this point some natural questions arise: how large are the neglected contributions $O(\bar{g}^k)$ for energies much below the electroweak scale? And, how can we obtain the "complete" result of $\langle O \rangle$?

On top of these questions, many problems of QCD (and QFTs) clearly demand non-perturbative methods. Many interesting phenomena, such as *chiral symmetry breaking* or *confinement*, require a non-perturbative formulation of the theory in order to be studied. In this respect, QCD is extremely beautiful, because it is formulated in a very simple and elegant way, but the question whether one and the same theory provides a full description of strong interactions from hadron physics and bound states to jets processes, in collider experiments, is fascinating and needs to be investigated precisely.

The only-known non-perturbative formulation of a QFT is through the discretization of space-time. The regularized QFT can consequently be "solved" by the numerical evaluation of the path integral, which is achieved by Monte Carlo (MC) simulations, compatibly with cpu resources.

When K.G.Wilson introduced the lattice regularization of QCD he was trying to explain one of the problems mentioned before, the confinement of quarks. In nature quarks

(and in general states carrying a color charge) are always bound in a color singlet. Given the transformation properties of the fundamental representation of $SU(3)$, this translates into either a meson $q\bar{q}$, a pair of quarks in the fundamental and anti-fundamental representation, or a baryon, a triplet of quarks. Perturbative computations are relevant only at high energies, where this long distance behavior is factorized in parton distribution functions and hard scattering processes involve quarks and gluons. On the other hand, the physics at low energies can be efficiently described in terms of hadronic degrees of freedom by an effective approach (see Chapter 5). This motivated Wilson in developing an innovative strategy to attack these problems: lattice QCD.

The elegance of this formalism is the possibility to formulate non-perturbatively QCD as a first-principle theory, without relying on approximations, e.g. in the effective theory approach. For example, the computation of the hadron spectrum is one of the greatest successes of the Lattice Community and provides a solid test of the theory by comparison with experimental values. Beyond that Lattice QCD proved to be also a fundamental predictive tool. The spectral properties of QCD at low energies are entirely described by a small set of mesons dictated by an approximately realized chiral symmetry for 3 flavors of quarks. From this simple observation *chiral perturbation theory* (ChPT), the low-energy effective description of QCD, has been developed. The masses of the up, down and strange quarks are small enough to be implemented as perturbations of a theory of Goldstone bosons: the pseudo-scalar octect mesons. For energies up to the ρ meson mass, ChPT provides a prediction for many quantities as a function of the pion and kaon mass. Lattice QCD, where artificially large quark masses can be simulated, is the perfect ground to test ChPT and determine its couplings.

Within the ranges of effective theories, the results from Lattice QCD computations are particularly relevant for the effective weak Hamiltonian. Indeed, in many electro-weak processes the QCD contribution can be factorized out in some matrix elements: for example, the pion to vacuum transition, usually called pion decay-constant, is required in leptonic decays $\pi \to l\bar{\nu}$. Similar non-perturbative results provided by the Lattice Community are used to extract CKM matrix elements, such as V_{ub} where at the moment there is some tension among different determinations.

Chiral symmetry is of central importance in the formulation of QCD on a lattice. Most of the discretizations of the fermion Lagrangian break this symmetry explicitly and the way it is recovered, when the lattice spacing is removed, is a crucial test of the validity of this approach. However, the same reasoning can be reversed such that the restoration of chiral symmetry can be used to improve the theory at finite lattice spacing and obtain results which require very mild extrapolations. In Chapter 2 we will introduce the discretized theory and explain the aforementioned problems related to the breaking of chiral symmetry. We will also present the basic ideas behind the technique used to "accelerate"

the convergence to the continuum limit, usually known as *Symanzik's improvement program*.

Once the theory is discretized, it is particularly suitable for numerical simulations. Path integral expectation values can be computed through Monte Carlo processes: firstly one needs to formulate an algorithm capable of generating a set of (gauge) field configurations; secondly one needs to define observables in the lattice formulation which can be measured on this set of configurations. Expectation values become then simple averages of these measurements, and errors can be treated by statistical means.

An important aspect of lattice calculations is the use of computer resources. In the last decades the performances of cpus and memories increased almost at an exponential rate, and the Lattice Community heavily profited from this. However, even if the increase of physical power of machines was necessary, what really made new corners in parameter space accessible to simulations are many theoretical and algorithmic developments.

As we will see in the next Chapters, the contribution of the fermions is the most demanding task in practical simulations. Indeed, in the early 90's, when such technological and conceptual advances were not yet at hand, the simulations being performed were *quenched*. The hadron spectrum, as a property of QCD, was known with already good precision, but it was measured from simulations where the action in the exponent of the path integral was the pure Yang-Mills one. This means, from a diagrammatic point of view, that fermion loops were not included in the computations.

Quenched simulations are less expensive, because only local updates are needed. Fermions on the other hand require the inversion of the Dirac operator, which is a "global" operation. On top of this, the more singular is this operator, the more demanding will be the inversion. Indeed the first simulations with *dynamical* fermions were at very high masses, where this problem does not occur. Nowadays, the first simulations with pions as light as in nature are finally possible thanks to algorithmic (and some theoretical) progresses. Some of them have been employed in this study and they are described in Chapter 3 and Chapter 4.

Assuming that fermions are not a problem anymore, there is a second practical issue in lattice computations. QFT and QCD require renormalization and the lattice spacing a plays the role of a natural cutoff for ultraviolet physics. However results from lattice computations must be extrapolated to the *continuum limit*, defined at $a = 0$, and therefore a prescription on how to send $a \to 0$ is required also in this case. We leave this discussion to Chapter 1, where we will review the basic renormalization properties of the lattice formulation. Clearly, when a is reduced and the volume in physical units is kept constant (or above a certain threshold where finite size effects are under control) the number of points to be added to the simulations grows. On top of this naive scaling, a second obstacle is present in simulations at small lattice spacing: the growth of *autocorrelations*,

known as *critical slowing down*.

In other words, there exists a correlation among successive configurations within a *Markov chain*. When a is reduced this correlation increases, which means that simulations have to be longer to target the same statistical precision.This statement, however, depends on the measured observable. Indeed it has been demonstrated that some peculiar quantities, related to the topology of the gauge fields, are particularly sensitive to this dramatic scaling of the autocorrelations, which has been measured in a quenched study [6].

The topological charge is an object strongly related to the classical dynamics of the gauge fields. Configurations generated from a Markov process are instead very rough and a smoothing procedure is needed to remove the high frequencies and be able to measure the charge at finite lattice spacing. Only recently [7, 8], a theoretically sound smoothing/smearing technique has been devised. It is known as *Wilson flow* and allows the computation of topological properties in the continuum in a controlled manner. Thanks to the Wilson flow, in Refs. [8, 9] it has been demonstrated that one of the sources of the critical slowing down of simulations is the presence of barriers between different topological sectors. These barriers grow with a high power of $1/a$ and prevent the Markov process from correctly sampling the whole field space at small lattice spacings.

Therefore if the simulation is "stuck" in one topological sector the topological charge is *frozen* and the simulation is no more ergodic. In Ref. [10] it has been shown that imposing Dirichlet boundary conditions in the time direction, on the field strength tensor, cures the freezing of the charge (also the fermions are required to satisfy certain boundary conditions). These boundary conditions (BC) are called *open boundary conditions* and their pictorial description is that instantons can flow in and out of the lattice through the temporal "open" boundaries.

After their proposal [11], open BC have been used for the first time in large volume simulations in Ref. [12] and this thesis is based on the analysis of those gauge-field configurations. Therefore in Chapter 3 we will describe the problems related to topology freezing in simulations with periodic BC and how they are cured by the open boundaries, by support of numerical results.

Since many years, the ALPHA collaboration[1] is involved in a large-scale project, whose principal goal is the computation of the strong coupling constant α_s, from low to high energies, where the matching with perturbation theory can be reliably done. The strategy is divided in two main branches. On the one hand finite-size and recursive techniques are used to compute the running of the coupling non-perturbatively in terms of an "intermediate" scale. On the other hand, large-volume simulations are used to renormalize the theory by computing a quantity, known in physical units from experiments, which is later used to convert all quantities (renormalization scale of the running coupling included)

[1] http://www-zeuthen.desy.de/alpha/

in MeV or fm. This thesis is focused on the second part, namely the computation of a reference scale for lattice simulations.

As first-principle results, lattice computations, at present, are still based on some restrictions and assumptions. Firstly, isospin breaking is usually neglected and the light quarks, up and down, are assumed degenerate. Isospin effects are in any case expected to be small and they will become relevant in the future decades, when lattice computations will be able to provide sub-percent results in the continuum limit with controlled systematic errors. At that point, QED effects will be included as well.

Secondly, heavy quarks are excluded from the simulations. For example, bottom-related observables, e.g. B-meson decay constants, can be obtained in an Effective-Theory approach (see for instance Ref. [13]), but sea strange and charm effects have been included only in the last years in lattice computations. Recently we have studied the effects of a dynamical charm quark on low-energy hadronic scales [14] and we estimated such contributions to be on the level of a few permille. In this thesis we will analyze ensembles including only a dynamical strange field in the generation of gauge-field configurations. However, since we will reach a few percent accuracy on our reference scales, we will be able to safely neglect the effects of a heavy sea quark.

The manuscript is organized as follows: in Chapter 1 we will review the basic renormalization properties of the discretized theory together with the strategy to compute α_s, in order to explain which is the role of the present work. In the Second Chapter we will introduce the lattice formulation and describe its properties. In Chapter 3 we will address the Monte Carlo techniques used to simulate the theory, their problems and the solutions adopted (aforementioned topology freezing and open BC). In the Chapters 4 and 5 a description of the set of ensembles produced and of the measurements of mesonic spectral quantities will be given. Finally in Chapter 6 we will describe the strategy to set the scale with those.

1 Renormalization

In quantum field theories the objects of primary interest are correlation functions from which physical observables, e.g. cross sections, can be computed. They are completely determined by the structure of the Lagrangian, whose kinetic term is usually quadratic in the fields, thus making the free theory analytically solvable. Once interactions are switched on, correlation functions can be evaluated by expanding the expectation values around the free theory in powers of the coupling constant. This is the perturbative approach often visualized through Feynmann diagrams.

At tree-level, the lowest order in the perturbative expansion, the propagation of a particle is unchanged w.r.t. the free theory. Beyond that, the first correction is given by a second particle traveling in a virtual loop placed between the end points of the correlator. Such virtual particle possesses an "unphysical" momentum, which must be integrated out. Depending on the structure of the interactions and on the particles involved, the integrated functions may not fall to zero fast enough at infinity, thus making the loop-integrals divergent. Therefore beyond tree-level a *regulator* is needed to make the loop contributions finite. For example the following 4-dimensional integral can be regularized either by imposing a hard cutoff Λ on the (integrated) momentum, or by analytically continuing the integral from 4 to $4-2\epsilon$ dimensions

$$\int d^4q \frac{1}{(q^2+m^2)((q+p)^2+m^2)} \sim \begin{cases} \Omega_3 \int^\Lambda dq\; q^{-1} + O(q^{-2}) & = \Omega_3 \ln \Lambda \quad +\text{finite} \\ \Omega_{4-2\epsilon} \int dq\; q^{-1-2\epsilon} + O(q^{-2}) & = A\epsilon^{-1} \quad +\text{finite} \end{cases}$$

In both cases the singularities re-appear once the limits $\Lambda \to \infty$ or $\epsilon \to 0$ are taken. However the usefulness of these approaches, in particular of the second one known as *dimensional regularization*[1], is that now a classification of the divergences is possible and the Lagrangian can become predictive again with the addition of suitable *counter-terms* to cancel the infinities.

Note that these counter-terms must be of the same structure of the already existing operators in the Lagrangian, e.g. the mass counter-term for a scalar field must be of the form $\delta m^2 \phi^2$. Theories requiring a new set of operators and couplings at every higher loop-level are called non-renormalizable. On the contrary, if only a redefinition of the bare couplings and masses (denoted by the subscript 0) into renormalized ones, is sufficient to absorb the divergences, the theory is renormalizable and predictive at all energies.

[1]Note that the Λ-regularization of the integral breaks Lorenz invariance, instead of dimensional regularization which preserves also gauge symmetry.

A more convenient way to deal with renormalization is to introduce *renormalization factors* Z and renormalized parameters and fields

$$\phi_{\rm R} = Z_\phi \phi\,, \quad g^2_{\rm R} = Z_g g_0^2\,, \quad m^2_{\rm R} = Z_m m_0^2\,, \tag{1.1}$$

such that the Lagrangian depending on those produces finite results. In dimensional regularization they can be expanded as $Z = 1 + \sum_n \epsilon^{-n} b_n g_0^{2n} + c$, and this method of "subtracting" the ϵ-poles defines the well-known *minimal subtraction scheme* (MS). The series of coefficients b_n depend on the renormalized quantity associated to the Z factor, while c, which is a finite contribution, can be used to conveniently cancel some finite terms in Feynmann diagrams. A particular choice of c is given by the relation $2/\bar{\epsilon} = 2/\epsilon + \log(4\pi) - \gamma_{\rm E}$ which defines the popular $\overline{\rm MS}$ scheme.

The Lagrangian is dimensionful $[\mathcal{L}] = [m]^4$, so what happens when it is dimensionally continued to $[\mathcal{L}] = [m]^{4-2\epsilon}$? Scale transformations do not change the kinetic term in the Lagrangian, which fixes the (engineering) dimensions of the fields. Interaction terms[2], however, require an appropriate rescaling of the couplings under these transformations, thus giving an explicit dependence on an arbitrary mass μ of the renormalized Lagrangian

$$\mathcal{L}_{\rm bare}(g_0, m_0) = \mathcal{L}_{\rm R}(\mu^{2\epsilon} g_{\rm R}, m_{\rm R})\,, \quad g_{\rm R} = \mu^{-2\epsilon} Z_g g_0\,. \tag{1.2}$$

The presence of μ through the coupling constant keeps trace in Feynmann diagrams of the fact that we are in $4-2\epsilon$ dimensions and therefore an explicit dependence must also be present in the Z factors. To understand the role of μ we consider first a physical observable P (depending on generic momenta p_i) computed from the two Lagrangians

$$P(p_i, g_{\rm R}, m_{\rm R}, \mu) = P(p_i, g_0, m_0)\,, \tag{1.3}$$

and then we evaluate the derivative w.r.t. $\log\mu$, which gives the famous *renormalization group equations* [15, 16]

$$\left[\mu\frac{\partial}{\partial\mu} + \beta(g_{\rm R})\frac{\partial}{\partial g_{\rm R}} - \gamma_m(g_{\rm R}) m_{\rm R}\frac{\partial}{\partial m_{\rm R}}\right]_{g_0, m_0} P = 0\,, \tag{1.4}$$

where we have introduced the β-function and the mass anomalous dimension[3]

$$\beta(g_{\rm R}) = \mu\frac{\partial g_{\rm R}}{\partial\mu}\,, \quad \gamma_m(g_{\rm R}) = -\frac{1}{m_{\rm R}}\mu\frac{\partial m_{\rm R}}{\partial\mu}\,. \tag{1.5}$$

From the definitions of the renormalized coupling discussed above it is clear that both functions can be evaluated perturbatively, in particular the β-function at $\epsilon = 0$ is given by

$$\beta(g_{\rm R}) = -b_0 g_{\rm R}^3 - b_1 g_{\rm R}^5 + O(g_{\rm R}^7)\,, \tag{1.6}$$

[2]Here the formulae hold for the scalar interacting theory ϕ^4 and QCD.

[3]For later convenience we have already considered a mass-independent renormalization scheme where there is no dependence on $m_{\rm R}$ in β and γ. This is the case in the $\overline{\rm MS}$ scheme.

where the one- and two-loop coefficients for QCD with $N_{\rm f}$ flavors are

$$(4\pi)^2 b_0 = 11 - \frac{2}{3}N_{\rm f}\,, \quad (4\pi)^4 b_1 = 102 - \frac{38}{3}N_{\rm f}\,. \tag{1.7}$$

Eq. (1.4) describes how a change in μ is compensated by a change in the renormalized coupling and masses such that P is kept fixed. The first one can be completely absorbed in a scale transformation which, in other words, is equivalent to a redefinition of the momenta p_i. Therefore the renormalization scale μ corresponds to the physical energy at which the process is considered. In particular fixing the renormalized coupling at some energy $\tilde{\mu}$ and integrating the β-function up to $\mu' = e^t\tilde{\mu}$ defines a *running coupling*, which at one-loop is

$$g^2_{\rm R}(t) \approx \frac{g^2_{\rm R}(0)}{1 + 2b_0 t g^2_{\rm R}(0)} \overset{t\to\infty}{\to} 0\,. \tag{1.8}$$

Eq. (1.8), together with the positive sign of b_0 in eq. (1.7) ($N_{\rm f} = 6$ in QCD), tells us that at high-energies non-abelian gauge theories become *asymptotically free* [17, 18]. This behavior suggests that the condition on $g_{\rm R}(0)$ can be replaced by the integration constant of the β-function at small $g_{\rm R}$[4]

$$\Lambda = \mu e^{-\frac{1}{2b_0 g^2_{\rm R}}} (b_0 g^2_{\rm R})^{-b_1/2b_0^2} \exp\Big\{ -\int_0^{g_{\rm R}} dx \Big[\frac{1}{\beta(x)} + \frac{1}{b_0 x^3} - \frac{b_1}{b_0^2 x}\Big]\Big\}\,. \tag{1.9}$$

To summarize, in the case of mass-less QCD we start from a theory depending only on one dimensionless coupling and after renormalizing it, a new infrared scale appears, $\Lambda_{\rm QCD}$, which is completely fixed by the UV regime of the theory.

Since it is scheme-dependent and in the following Chapters we will mention more schemes, it is important to understand how different couplings and Λ-parameters can be related. Similarly to the steps in eq. (1.3) and eq. (1.4), from the invariance of physical observables under the choice of the renormalization conditions, two different schemes $g_{\rm R}$ and $g'_{\rm R}$ can be related by a finite renormalization

$$\beta'(g'_{\rm R}) = \beta(g_{\rm R})\frac{\partial g'_{\rm R}}{\partial g_{\rm R}}\,, \quad g'_{\rm R} = g_{\rm R} + c_1 g^3_{\rm R} + O(g^5_{\rm R})\,. \tag{1.10}$$

In principle all the coefficients of the perturbative expansion of β' are scheme-dependent and different from eq. (1.7). However a few lines of algebra show that b_0 and b_1 are universal

$$\begin{gathered}\beta\frac{\partial g'_{\rm R}}{\partial g_{\rm R}} = -b_0(g^3_{\rm R} + 3c_1 g^5_{\rm R}) - b_1 g^5_{\rm R} + O(g^7_{\rm R}) \quad \leftarrow \quad g^3_{\rm R} = g'^3_{\rm R} - 3c_1 g'^5_{\rm R} + \dots \\ \beta'(g'_{\rm R}) = -b_0 g'^3_{\rm R} - b_1 g'^5_{\rm R} + O(g'^7_{\rm R})\,.\end{gathered} \tag{1.11}$$

[4]Note that the integral of $1/\beta(x)$ in the square brackets converges at $x = 0$ only thanks to the subtraction of the one and two-loop terms.

Moreover only the finite coefficients c_1 and b_0 are needed to relate the two integration constants

$$\frac{\Lambda'}{\Lambda} = \exp\left[\frac{c_1}{b_0}\right]. \tag{1.12}$$

1.1 The continuum limit

In the previous Section we have mentioned two different ways to regularize divergences in QFTs. The hard momentum cutoff is less popular because in general it breaks the Lorenz and gauge invariance of the theory. A solution to the latter problem can be found by discretizing space-time on a lattice, where non-abelian gauge theories can be formulated preserving gauge symmetry. This is the topic of the Chapter 2, whereas in the following we investigate how the theory in the continuum is recovered. The key point to introduce the lattice discretization, is the possibility to compute correlation functions non-perturbatively, by a direct evaluation of the path integral through numerical simulations.

As a regulator, the lattice spacing a needs to be removed ($a \to 0$) keeping physical observables finite, pretty much as for ϵ in dimensional regularization. Let us assume to have at disposal a set of non-perturbatively-computed (dimensionless) physical observables P_i: in general they will depend on the combination aq, q being the norm of the Euclidean momentum of the process, g_0 and the set $\{am_i\}$. The renormalization path is somewhat different w.r.t. what we have seen in the previous section, since now we want to understand in which direction the bare parameters have to be changed to reach $a = 0$, while keeping the physics fixed. These renormalization conditions can be implemented by demanding that

$$P_i(aq, g_0, \{am_i\}) = \mathcal{P}_i\,, \quad i = 1, \cdots N_{\rm f} + 1\,, \tag{1.13}$$

with $\mathcal{P}_i$ a fixed value in the continuum limit of P_i. Note that $N_{\rm f}+1$ conditions are needed to fix all the free parameters in the theory, namely the coupling g_0 and $N_{\rm f}$ masses. Generic observables (different from those chosen in eqs. (1.13) and computed with the values of g_0 and am_i obtained by solving eqs. (1.13)) will differ from their continuum counter-part by terms of $O(a^p)$, with $p > 1$, called *scaling violations*. Their coefficients are completely fixed by the choice of the functions P_i, which hence define a renormalization scheme.

To remove these lattice artifacts, the measured observables must be extrapolated to the limit $a \to 0$. To understand how this limit is reached we consider the derivative of eq. (1.13) w.r.t. $\log(a)$

$$\left[a\frac{\partial}{\partial a} - \beta_{\rm lat}(g_0)\frac{\partial}{\partial g_0} + \sum_i \gamma_{\rm lat}(g_0) m_i \frac{\partial}{\partial m_i}\right] P_i = O(a^p \mu^p)\,, \tag{1.14}$$

where we have introduced the lattice β-function (and γ-function)

$$\beta_{\rm lat}(g_0) = -a\frac{dg_0}{da}\,. \tag{1.15}$$

Eq. (1.14) describes how a change in the bare parameters g_0 and m_i can compensate the removal of the cutoff $a \to 0$, while keeping the physics fixed. Note that we assume the observable P_i to be physical quantities, meaning that they do not have divergences.

Physical observables starting at order g_0^2 in perturbation theory can be used to define a renormalized coupling. The force F, between a pair of static quarks, is a suitable candidate, as it can be extracted in lattice simulations from the large time behavior of Wilson Loops (for convenience we consider a massless theory)

$$\bar{g}^2_{q\bar{q}}(a\mu, g_0) = \frac{4\pi}{C_F} r^2 F(r/a, g_0)\,, \quad \mu = 1/r\,, \quad C_F = 4/3\,. \tag{1.16}$$

Therefore $P_i = \bar{g}_{q\bar{q}}$ in eq. (1.14) gives a relation between $\beta_{\rm lat}$ and the β-function evaluated in the continuum theory up to lattice artifacts

$$\frac{\partial \bar{g}_{q\bar{q}}}{\partial g_0}\beta_{\rm lat}(g_0) = \mu\frac{\partial \bar{g}_{q\bar{q}}}{\partial \mu} = \beta^{\rm cont}_{q\bar{q}}(\bar{g}_{q\bar{q}}) + O(a^p\mu^p)\,. \tag{1.17}$$

Eq. (1.17) resembles a lot eq. (1.10) which, in the previous section, has been used to demonstrate the universality of b_0 and b_1. Therefore the results obtained in eq. (1.11) can be extended also to the case of $\bar{g}_{q\bar{q}}$, which is a well-defined renormalized coupling. According to the expansion in eq. (1.10) it can be related to[5] $g_{\rm R}$ at one-loop, through the coefficient $c_{1,\overline{\rm MS}q\bar{q}}$. Hence it follows that also for $\beta_{\rm lat}$, up to two loops, the following expression holds

$$\beta_{\rm lat}(g_0) = -b_0 g_0^3 - b_1 g_0^5 + O(g_0^7) + O(a^p\mu^p)\,, \tag{1.18}$$

with b_0 and b_1 taken from eq. (1.7). Using the perturbative result in eq. (1.18) we can finally find the location of $a = 0$ in parameter space

$$\beta_{\rm lat} = -a\frac{\partial g_0}{\partial a} \approx -b_0 g_0^3 \quad \overset{g_0\to 0}{\to} \quad a \propto e^{-1/(2b_0 g_0^2)}\,. \tag{1.19}$$

The critical point in $\beta_{\rm lat}$, dictated by asymptotic freedom, is fundamental to guarantee the existence of the continuum limit. Similarly as in eq. (1.9) the integration constant $\Lambda_{q\bar{q}}$ can be defined at small $\bar{g}_{q\bar{q}}$ and only the aforementioned coefficient $c_{1,\overline{\rm MS}q\bar{q}}$ is necessary to relate it to $\Lambda_{\overline{\rm MS}}$.

[5] Note that we use the notation from the previous Section when referring to dimensional regularization or MS, $\overline{\rm MS}$ schemes.

1.2 The hadronic scheme

The renormalization conditions in eqs. (1.13) define a scheme through the choice of the set of P_i. A popular choice within the lattice community is to use ratios of hadronic masses, which define the so-called *hadronic scheme*. Imagine for a fixed value of g_0 to perform several simulations with different values of the bare quark masses. Hadron masses can be computed from the exponential decay of suitable correlation functions and they are known usually with a good precision from experiments (e.g. proton, pions, kaons, etc.). For example fixing $N_{\rm f}$ of the following ratios

$$\frac{am_h}{am_{\rm proton}} = \text{phys.value}\,, \quad h = K, \pi, \ldots \tag{1.20}$$

to the value they have in nature, removes the dependence on the bare parameters, apart from g_0. Suppose to have extracted also an excited state am_Δ from one of the previous correlators: its value in physical units can be obtained by using the experimental number of the proton mass

$$m_\Delta = am_\Delta(g_0, am)\frac{m^{\rm exp}_{\rm proton}}{am_{\rm proton}}\Big[1 + O(a^p)\Big]\,. \tag{1.21}$$

The size of the scaling violations on the r.h.s. determines how far m_Δ, for this choice of g_0, is from its continuum counter-part. To correctly renormalize the theory, the procedure above must be repeated for smaller and smaller values of g_0 and eventually extrapolate the results to $a = 0$.

In this process a *reference scale* has been used: the proton mass fixed the lattice spacing for each value of the bare coupling

$$a(g_0) = \frac{am_{\rm proton}}{m^{\rm exp}_{\rm proton}}\,. \tag{1.22}$$

As an alternative to hadron masses, fixing a renormalized coupling automatically fixes a (length) scale. If we consider the definition given in eq. (1.16), we obtain

$$\bar{g}^2_{q\bar{q}} = const \quad \to \quad r_c^2 F(r)|_{r=r_c} = c\,, \tag{1.23}$$

where two popular choices are $c = 1.65$ and 1, defining r_0 [19] and r_1 [20] respectively.

Hence the choice of the reference scale is crucial in taking the continuum limit because it changes the relative discretization errors in the extrapolations of the observables. Even if at $a = 0$ the choice of the scale does not matter anymore, since results converge to common values, on the practical level it can play an important role as we will discuss in the next Section.

1.3 The reference scale

In eq. (1.22) the errors from the lattice computation count as much as those of the experimental determination of the proton mass. Therefore a first requirement for a reference scale is an experimental accuracy sufficiently better than the corresponding lattice computation[6]. In addition to that a "good scale" must satisfy certain requirements, such as

- precision: observables with high statistical precision are preferable;
- discretization errors: the lattice artifacts introduced by the scale should be as small as possible, as they add up to those of the observable under study (note that this is a statement relative to the specific observable, since, sometimes, compensations take place);
- computational cost: from the practical point of view, the computer resources, needed to compute the observables for scale setting, should be relatively small compared to other interesting quantities.

We have already presented in eq. (1.21) the possibility to use baryon masses, such as the proton or the Omega baryon. They can be computed from the large time behavior of the corresponding correlation functions, whose signal, however, deteriorates fast, due to a problem known as *signal-to-noise decay*. Indeed the identification of a plateau, with a good control over systematic errors (coming from excited states at short distances) and statistical accuracy (the longer the plateau the more precise is the average), can be difficult as depicted in Figure 1.1, taken from Ref. [21].

For baryonic observables the criterion on precision is often not satisfied, even if they show small lattice artifacts. On the contrary mesonic correlation functions have an approximately constant signal-to-noise ratio which allows to extract masses with excellent precision. However, meson masses are usually employed to renormalize the N_{f} bare quark masses. Therefore interesting candidates for scale setting are the corresponding decay constants, to be defined below, which can be obtained with per-cent accuracy and satisfy all the requirements listed above. They have longer plateaus and an excellent control over systematic errors is usually achieved.

Our analysis will be concentrated on those. In Chapters 5 and 6 we will describe the measurements and the extraction of spectral quantities from two-point correlators within our specific setup, together with the main strategy to compute the lattice spacing.

[6] Clearly the observable must be known from experiments. This is not the case for $\bar{g}_{q\bar{q}}$ since confinement prevents the interquark potential from being measurable. Hence r_0 can be used only at some intermediate stage, e.g. when tuning some parameters to target a particular point in the renormalized theory. Note that phenomenological models based on $c\bar{c}$ potential predict a value for r_0 which is roughly 0.5 fm.

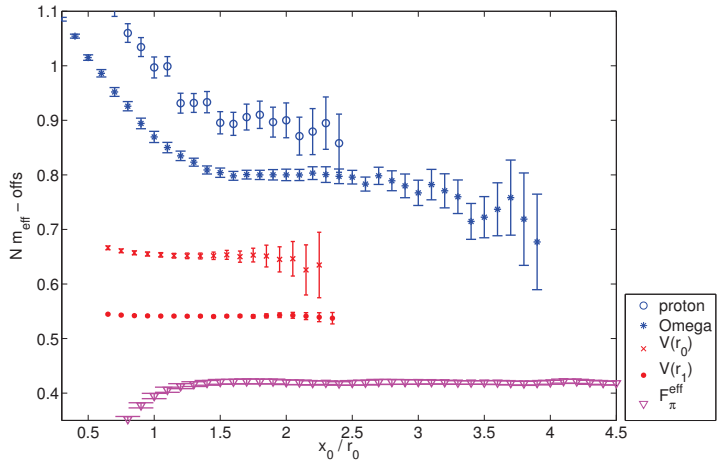

Figure 1.1: Plateaus for various observables often used to set the scale in lattice simulations, taken from Ref. [21]. The normalization of the vertical axis is such that a direct quantitative comparison can be made immediately in the plot.

1.4 The running of the coupling

Despite the fact that a reference scale is the central object to take the continuum limit, it is often not interesting from a physical point of view. The main goal beyond this thesis is the computation of the Λ parameter for QCD with 3 flavors. Therefore we present here the main strategy adopted by the ALPHA Collaboration, in which this thesis enters through the scale determination.

By means of numerical simulations, the running of a non-perturbatively defined coupling can be computed at low energies, evolved up to the regime where perturbation theory holds, and eventually run to infinite energy by using PT. Even though it sounds very promising, several technical obstacles obscure its feasibility. Firstly, if we want to evolve $\bar{g}_{q\bar{q}}$ to energies around 10 GeV we need to compute the interquark force at very small distances, $r \approx 0.02\,\mathrm{fm}$. Hence, a much smaller lattice spacing would be required to keep discretization effects under control, but, at present, simulations are performed at $a \geq 0.05\,\mathrm{fm}$[7]. Secondly, to control finite-size effects the physical volume should be large enough (usually $m_\pi L \geq 4$ for full QCD) and, when the lattice spacing is decreased, L/a grows up to the point where the computational cost is exceedingly large. All in all, we

[7]This argument holds also for other definitions of renormalized couplings, since the renormalization scale is $\mu = 1/r$.

have many scales involved

$$\frac{1}{L} \ll 130\,\mathrm{MeV} \ll \mu \approx 10\,\mathrm{GeV} \ll \frac{1}{a}\,, \tag{1.24}$$

which define the limits of this approach, since we can only use limited resources and lattices with $L \gg 100a$ would be needed.

In Ref. [22] Lüscher, Weisz and Wolff proposed to identify the renormalization scale with the size of the volume L. In practice, instead of trying to avoid finite size effects, their idea is to make use of them to obtain a definition for a coupling, running with L. This approach simplified tremendously eq. (1.24), because simulations at small volumes and couplings are technically easier to run and the *step scaling method* allows to go to high energies.

Let us assume to start with a simulation in a volume $L/a = 8$, whose renormalized coupling is $\bar{g}^2 = u$. If we run a second simulation at the same value of the bare coupling, but with $L/a = 16$, the new renormalized coupling defines the scaling function with step 2, $u' = \bar{g}^2(2L) \equiv \Sigma(2, u, a)$. If we now perform a set of simulations in different volumes, e.g. $L/a = 6, 10, 12$, where each time we tune g_0 such that the renormalized coupling is always u, from the corresponding runs in the "double-volumes" $L/a = 12, 20, 24$, $\sigma(2, u) = \lim_{a/L\to 0} \Sigma(2, u, a)$ can be extrapolated to the continuum limit.

This procedure can be recursively iterated, by starting now from a simulation with $L/a = 8$ but a different $\bar{g}^2$. In the end we will have a determination of $\sigma(2, u)$ for a certain range of u, where the largest renormalized coupling corresponds to the longest length L_{max}. Since σ is a discrete version of the β-function, the running of the coupling at energy $2^k/L_{\mathrm{max}}$ can be obtained as

$$\bar{g}^2(2^{-k} L_{\mathrm{max}}) = \sigma(2, u^{k+1})\,. \tag{1.25}$$

Once the non-perturbative β-function is known, the Λ parameter can be extracted in the SF scheme and related to the $\overline{\mathrm{MS}}$ scheme according to eq. (1.12). All in all the general strategy is divided in two steps:

- run finite-volume simulations (FV) to compute the coupling in a range of energies from $1/L_{\mathrm{max}}$ to $2^n/L_{\mathrm{max}}$, as described above, and at $2^n/L_{\mathrm{max}}$ connect to perturbation theory and extract Λ_{SF};
- perform large volume simulations to renormalize the theory in the hadronic scheme (HS), by computing a *reference scale* f_{had}.

Part I	Part II	
HS	$\mathrm{FV}(1/L_{\mathrm{max}}) \to \mathrm{FV}(2/L_{\mathrm{max}}) \to \cdots \to$	$\mathrm{FV}(2^n/L_{\mathrm{max}})$
$\downarrow$		$\downarrow$
$L_{\mathrm{max}}[\,\mathrm{fm}]$		$\mathrm{PT}(2^n/L_{\mathrm{max}} \to \infty)$

The Λ parameter in the $\overline{\text{MS}}$ scheme can eventually be computed by evaluating

$$\Lambda_{\overline{\text{MS}}} = f_{\text{had}}^{\text{exp}} \times \exp\left[\frac{c_{1,\overline{\text{MS}}\,\text{SF}}}{b_0}\right] \times \frac{\Lambda_{\text{SF}} L_{\text{max}}}{f_{\text{had}} L_{\text{max}}}\,, \tag{1.26}$$

and once Λ is obtained in units of some hadronic scale, all references to the intermediate steps disappear.

1.4.1 The Schrödinger Functional

This thesis is focused on Part I of the previous diagram, therefore we summarize here only-briefly the main features of the FV simulations.

Since the connection with perturbation theory is done at high energies, the coupling obtained from the FV scheme must be expanded as well in powers of g_0, to do the matching. In a finite box, Feynman rules and perturbation theory are the same as in infinite volume only if suitable boundary conditions in the time direction are chosen, such as twisted or Dirichelet BC[8]. The setup used by the ALPHA collaboration relies on Dirichelet BC, whose path integral defines a Schrödinger Functional (SF), name coming from its quantum-mechanical interpretation.

Such boundary conditions automatically provide an infrared cutoff $\sim 1/T$ [24], T being the temporal extent of the lattice. Therefore simulations at zero quark masses, which are practically impossible in large volumes as we will see in Chapter 4, are here feasible. This feature has been extensively exploited to define and compute *massless* renormalization schemes [25].

A second important property of the SF is its renormalization. Dirichelet BC clearly break translation invariance in time. Hence, when considering the renormalized theory, mixing with additional operators, which before were protected by the symmetry, are now to be expected and new divergences appear. In the case of the SF it has been proven [26] that no additional boundary counter-terms are required, and the usual renormalization of the bare coupling and masses, is sufficient to cancel all the divergences.

Finally, the boundaries induce a particular background gauge field B in the action. The path integral can consequently be expanded, at weak coupling, around the background solution and a definition of a renormalized coupling, as a function of B, can be obtained [27].

The SF has been used also to compute renormalization factors of local currents, since at the boundaries it is possible to construct gauge-invariant operators, which can be used to evaluate correlation functions and define renormalization or improvement conditions for the usual operators in the bulk. In fact in this work we heavily profit from many such results obtained with the SF setup, and its new development, the chirally rotated

[8] Problems arise from the presence of physical zero modes in periodic boundary conditions [23]. The basic idea to avoid this problem is to choose boundary conditions "incompatible" with them.

SF [28, 29]. Covering also those would go beyond the scope of the thesis and therefore we leave these topics to the reader (see for instance Refs. [30, 31, 32, 33]), and we turn now to the introduction of Lattice QCD.

2 Lattice QCD

In this Chapter we describe the lattice formulation of QCD, which dates back to Wilson's famous paper in 1974 [34]. The first step consists in introducing the lattice spacing a thus discretizing the Euclidean space-time. If we consider the Fourier transform of any field living in a discretized space-time, it is easy to show that π/a defines a cutoff for the momenta. Moreover, if space has maximum extent L, momenta become discrete as well ($p_\mu = 2\pi n/L$). Hence, the underlying QFT, with infinite degrees of freedom, can be recovered by sending $a \to 0$ only after the thermodynamic limit $L \to \infty$. Since we are interested in local QFTs, we replace derivatives with the usual forward and backward finite differences. From here and through rest of the thesis the notation for covariant derivatives is

$$a\nabla_\mu \psi(x) = U_\mu(x)\psi(x + a\hat{\mu}) - \psi(x)\,, \tag{2.1}$$

and for lattice partial derivatives

$$a\partial_\mu f(x) = f(x + a\hat{\mu}) - f(x)\,. \tag{2.2}$$

The backward derivatives are expressed with the symbols $\nabla^\star_\mu$ and $\partial^\star_\mu$ and the symmetric ones are always explicit in the formulae. To keep a light notation we do not introduce the distinction between lattice and continuum definitions as we will clarify in the text when the latter will be used[1].

2.1 The pure gauge theory

The Yang-Mills action in Euclidean space-time

$$S = -\frac{1}{2g_0^2}\int d^4x\ \mathrm{tr}\left\{F_{\mu\nu}F_{\mu\nu}\right\}, \quad F_{\mu\nu} = \partial_\mu A_\nu - \partial_\nu A_\mu + [A_\mu, A_\nu]\,, \tag{2.3}$$

describes the behavior of gluons (photons if the gauge group is abelian) without quarks and is invariant under gauge transformations.

In order to construct a theory, which preserves the same symmetry at finite lattice spacing, we need to consider the parallel transporter[2] between two adjacent sites x and

[1] Note that for free fermions there is no difference between ∇ and ∂ but obviously the two definitions will be used to keep the same formulae for the free and the interacting theory.

[2] The parallel transporter connects two points in space-time and under a gauge transformation $\Lambda(x) \in SU(N)$ it becomes $\Lambda(x)U_\mu(x)\Lambda^{-1}(x + a\hat{\mu})$.

$x + a\hat{\mu}$, called $U_\mu(x)$. In the lattice language $U_\mu(x)$ is represented by a *link* and it is a member of the Lie Group $SU(N)$, with $N = 3$ for QCD. From the transformation laws of the links U under the gauge symmetry, it emerges that only products of links along *closed paths* can generate gauge-invariant quantities, once the trace over the color space has been taken. Therefore, from the smallest of such paths, namely the *plaquette* p, the action at finite lattice spacing can be constructed as follows

$$S_g = \frac{1}{g_0^2} \sum_p \mathrm{tr}\left\{1 - U(p)\right\}, \tag{2.4}$$

where the sum runs over all the oriented plaquettes and $U(p)$ denotes the product of links U around p. S_g is real and in the formal limit $a \to 0$, with classical fields $A_\mu(x)$, reproduces eq. (2.3). An advantage of the lattice formulation is that gauge fixing is not required, since the theory is formulated in terms of elements of the group and not of the algebra as eq. (2.3).

From the plaquette action it is possible to construct a Hilbert space and to prove that the theory, defined by the partition function

$$\mathcal{Z} = \prod_{x,\mu} dU_\mu(x) e^{-S_g[U]} \tag{2.5}$$

is unitary [34]. Despite the non-perturbative treatment of $\mathcal{Z}$ via Monte Carlo simulations, weak- and strong-coupling expansions also exist. The latter, which is essentially an expansion in the characters of the group, shows, qualitatively, the two most interesting low-energy phenomena of Yang-Mills theories: confinement of static color charges and the presence of a massive state. However, it is far from being a proof in the continuum renormalized theory.

2.2 Fermions on the lattice

If we want to investigate full QCD, the fermionic fields must be included in eq. (2.5). We start, as before, from the free theory, which is described by the Dirac langragian $\mathcal{L} = (\gamma_\mu \partial_\mu + m_0)\psi$ (in Euclidean space time), and we follow the recipe in the substitutions of derivatives with finite differences[3]. The free fermionic propagator in momentum space is (α and β are spinor indices)

$$S^{-1}_{\alpha\beta}(p) = \left[m_0 + \sum_\mu i\gamma_\mu \tilde{p}_\mu\right]_{\alpha\beta}, \quad \tilde{p}_\mu = \frac{1}{a}\sin(p_\mu a), \quad p_\mu \in \left[0, \frac{2\pi}{a}\right], \tag{2.6}$$

[3]Replacing ∂_μ with symmetric finite differences.

which, in the continuum limit, describes 2^3 "spatial" copies of the same state with energy $m^2 + \vec{P}^2$

$$E^2 = m^2 + \frac{1}{a^2}\sum_k \sin^2(ap_k) \overset{a\to 0}{\to} m^2 + \vec{P}^2\,, \quad a\vec{p} = (n_1, n_2, n_3)\pi + a\vec{P}\,. \tag{2.7}$$

In addition to this, the time-slice propagator $S(x_0, \vec{p})$ exhibits other 2 poles. In fact, once the integral $\int dp_0$ is transformed into a contour integral in the complex plane, one encounters two poles which contribute to the final result. All in all, we have found that the physics described by a naively discretized Dirac Lagrangian corresponds to 2^D free relativistic fermions in the continuum limit, instead of 1, called *doublers*. In an interacting theory this effect manifests itself in the degeneracy of diagrams with fermion loops in the vacuum polarization, for example.

The reason of the doubling problem can be traced back to the order of the differential operator in the kinetic term in the Lagrangian. Apart from spinor indices, this is the real difference between a scalar and a fermionic field on the lattice. The fact that they obey a second and first order differential equations respectively, translates in a different relation between continuum and discrete momenta. In fact, the inverse propagator of a scalar field (obeying the Klein-Gordon equation of motion)

$$S^{-1}(p) = \Big[m_0 + \sum_\mu i\gamma_\mu \hat{p}_\mu\Big]\,, \quad \hat{p}_\mu = \frac{2}{a}\sin\left(\frac{p_\mu a}{2}\right), \tag{2.8}$$

corresponds only to one physical state with energy[4]

$$E^2 = m^2 + \frac{4}{a^2}\sum_k \sin^2\left(\frac{p_k a}{2}\right) \overset{a\to 0}{\to} m^2 + \vec{P}^2\,, \quad a\vec{p} = a\vec{P}\,. \tag{2.9}$$

2.2.1 Chiral symmetry and Wilson fermions

Hence, following this reasoning, we could argue that a possible solution to the doubling problem relies in "increasing" the order of the Dirac operator by adding a Laplacian. In order to avoid spoiling the continuum limit, Wilson's solution has been

$$S_{\mathrm{W}} = a^4\sum_x \overline{\psi}(x)\frac{1}{2}\Big[\gamma_\mu(\nabla_\mu + \nabla^\star_\mu) + 2m_0 - ar\nabla_\mu\nabla^\star_\mu\Big]\psi(x) = a^4\sum_x \overline{\psi}(x) D_{\mathrm{W}}\psi(x)\,. \tag{2.10}$$

We note immediately that the Laplacian disappears in the continuum limit, as it should be for an irrelevant operator. Moreover, if we look closer we note the following properties: firstly, the so-called Wilson term (applied to plane waves with momentum p)

$$-\frac{ar}{2}\nabla_\mu\nabla^\star_\mu \to \frac{ar}{2}\hat{p}^2 = \frac{2r}{a}\sum_\mu \sin^2\left(\frac{p_\mu a}{2}\right) = \frac{r}{a}\sum_\mu(1 - \cos(p_\mu a)) \tag{2.11}$$

[4]Note that the Brillouin zone is a torus manifold, thus periodic in all directions.

adds a term of $O(a^{-1})$ to the dispersion relation, such that states which before had the same energy at $ap_\mu = \pi$ now receive an infinite contribution in the continuum limit and only the corner $ap_\mu = (0,0,0,0)$ in the Brillouin zone survives[5]; secondly, the action in eq. (2.10) is invariant under parity (P), charge (C) and time reversal (T) transformations; thirdly, the discretized Wilson operator possesses an additional symmetry, $\gamma_5 D_{\mathrm{W}} \gamma_5 = D_{\mathrm{W}}^\dagger$, called γ_5-*hermiticity*; finally, similarly to the mass term, it breaks the invariance of the Lagrangian under chiral symmetry

$$\{a\hat{p}^2, \gamma_5\} \neq 0\,, \tag{2.12}$$

which is restored only in the continuum limit.

The last property enlightens the connection between the doubling problem and chiral symmetry, a connection which has been established and demonstrated by Nielsen and Ninomiya in 1981 [35]. Their theorem states that it is not possible to formulate a (free) fermion action whose Dirac operator D (we indicate with $\tilde{D}$ its Fourier transform) fulfills simultaneously all the following conditions:

1. $D(x)$ is local;
2. $\tilde{D}(p) = i\gamma_\mu p_\mu + O(a)$, hence it reproduces the correct physics as $a \to 0$;
3. $\{\gamma_5, D\} = 0$;
4. $\tilde{D}(p)$ has one single zero corresponding to a particle.

When we derived the naive formulation of lattice fermions we kept condititions 1,2,3 and it turned out that $S(p)$ produced 16 copies of identical relativistic fermions. Wilson's proposal, on the other hand, gives up on chiral symmetry and maintains the action local and doubler-free.

At this point, we are ready to switch on the gauge interaction and discuss Wilson's formulation of QCD. As in the continuum, the Yang-Mills action is added to the fermionic one, whose normal partial derivatives have been replaced by the covariant ones. Full QCD can therefore be regularized on the lattice, with Wilson's gauge action eq. (2.4) together with N_{f} Wilson's fermions eq. (2.10)

$$S = S_g + \sum_{f=1}^{N_{\mathrm{f}}} \left[a^4 \sum_x \overline{\psi}_f(x) D_{\mathrm{W}}(m_{0,f}) \psi_f(x) \right]. \tag{2.13}$$

[5]This is valid for a generic value of r. However, Wilson's choice $r = 1$ removes the doubling also at finite lattice spacing.

In the rest of the thesis we will frequently refer to the bare masses via the *hopping parameter* $\kappa_f = (2am_{0,f} + 8)^{-1}$. In fact, through a rescaling of the spinor fields the Wilson action for a single flavor f can be re-written as (we have chosen $r = 1$)

$$S_{\mathrm{W}}^f = \sum_x \overline{\psi}_f(x)\Big\{1-\kappa_f \sum_{\mu=0}^{3}\Big[(1-\gamma_\mu)U_\mu(x)\delta_{x,x+a\hat{\mu}}+\delta_{x,x-a\hat{\mu}}(1+\gamma_\mu)U_\mu^\dagger(x)\Big]\Big\}\psi_f(x)\,. \quad (2.14)$$

In the presence of a mass term $\overline{\psi}\psi$ in the continuum QCD Lagrangian, chiral symmetry is broken. However, the limit where all bare quark masses vanish corresponds to the point where chiral symmetry is fully restored, as both vector and axial currents have zero divergences (as we will see in the next Section). Therefore, the renormalization of the mass can be only multiplicative since, for zero bare quark masses, the renormalized quark masses computed through the divergence of the axial current is also zero, schematically

$$\text{at } m_0 = 0\,, m_{\mathrm{R}} = 0 \quad \rightarrow \quad \text{at } m_0 \neq 0\,, m_{\mathrm{R}} = Z_m m_0\,. \quad (2.15)$$

However, for the action in eq. (2.14), in the limit where all bare masses are sent to zero chiral symmetry is still broken by the irrelevant operator $-ar\nabla_\mu^\star\nabla_\mu$. In particular, to achieve vanishing renormalized masses (up to cutoff effects), the bare masses have to be tuned to a *critical* value m_{cr}, which is a function of g_0 only. Hence, the bare *subtracted* quark masses, defined by $m_{\mathrm{q},f} = m_{0,f} - m_{\mathrm{cr}}$, are those multiplicatively renormalized (not $m_{0,f}$), since the breaking of chiral symmetry shifts the chiral point by a value m_{cr}. Note that when moving from degenerate to non-degenerate quark masses

$$M = M_0 - m_{\mathrm{cr}}\mathbb{1} = \mathrm{diag}(m_{\mathrm{q},1}, m_{\mathrm{q},2}, \ldots, m_{\mathrm{q},N_{\mathrm{f}}})\,, \quad (2.16)$$

the renormalization pattern becomes even more complicated since singlet and non-singlet (scalar) renormalization factors differ. In the next Section we will delineate the full renormalization pattern up to $O(a^2)$.

Eventually a regularized theory for QCD has been developed. As we have seen once a symmetry is explicitly broken at the level of the Lagrangian, the renormalization pattern becomes in general more complicated. For composite operators the mixing with additional operators which, in the presence of the symmetry are otherwise protected, is expected. We now discuss the Ward Identities (WI) involving some of those.

2.2.2 Ward Identities

At the classical level Nöther's theorem relates the presence of a continuous symmetry of the Lagrangian to conserved currents and charges. Once the theory is quantized (path

integral formulation) current conservation is "promoted" to expectation values of correlation functions of local operators[6]

$$\langle \delta O \rangle = \langle \delta S O \rangle \,, \quad \rightarrow \quad \langle \delta S O \rangle = 0 \Big|_{\delta O = 0} \,, \tag{2.17}$$

known as *Ward-Takahashi identities* [36, 37]. Note that in anomalous WIs an additional term, the *anomaly*, appears in eq. (2.17). According to Fujikawa derivation [38], it comes from the non-invariance of the integration measure in the path integral. Non-unitary transformations generate a non-trivial Jacobian $J \neq 1$, whose variation δJ is indeed the anomaly.

The formal continuum theory with N_f mass-less fermions is invariant under $U_L(N_\mathrm{f}) \times U_R(N_\mathrm{f})$ chiral transformations and the introduction of a positive mass matrix $M_0 = \mathrm{diag}(m_{0,1}, \ldots, m_{0,N_\mathrm{f}})$ breaks it to a smaller subgroup. From the variation of the action δS deriving from a generic $SU(N_\mathrm{f})_L \otimes SU(N_\mathrm{f})_R$ transformation (which we rewrite in the usual infinitesimal vector-axial form)

$$\delta\psi = i\Big[\alpha_V^a \frac{\lambda^a}{2} + \alpha_A^a \gamma_5 \frac{\lambda^a}{2}\Big]\psi \,, \quad \delta\overline{\psi} = -i\overline{\psi}\Big[\alpha_V^a \frac{\lambda^a}{2} - \alpha_A^a \gamma_5 \frac{\lambda^a}{2}\Big] \,, \quad \lambda^a \in \mathfrak{su}(N_\mathrm{f}) \,, \tag{2.18}$$

according to eq. (2.17), the following Ward Identities can be obtained[7]

$$\langle \partial_\mu V_\mu^a(x) O(y) \rangle = \left\langle \overline{\psi}(x) \left[\frac{\lambda^a}{2}, M_0 \right] \psi(x) O(y) \right\rangle , \tag{2.19}$$

$$\langle \partial_\mu A_\mu^a(x) O(y) \rangle = \left\langle \overline{\psi}(x) \left\{ \frac{\lambda^a}{2}, M_0 \right\} \psi(x) O(y) \right\rangle . \tag{2.20}$$

They are best known as Partially Conserved Vector and Axial Current relations (PCVC and PCAC respectively). The former defines a conservation condition for the local vector current $V_\mu = \overline{\psi}(x)\gamma_\mu\psi(x)$ for degenerate masses, while the latter is recovered only in the limit $M_0 \to 0$, called *chiral limit*. The local currents appearing in the PCAC relation are the usual axial and pseudo-scalar quark bilinears[8]

$$A_\mu^a(x) = \overline{\psi}(x) \frac{\lambda^a}{2} \gamma_\mu \gamma_5 \psi(x) \,, \quad P^a(x) = \overline{\psi}(x) \frac{\lambda^a}{2} \gamma_5 \psi(x) \,. \tag{2.21}$$

Let us turn to the lattice theory, in particular to Wilson fermions. Applying the vector rotation, $\alpha_A = 0$ in eq. (2.18), to the action in eq. (2.14), we note that the variation of the

[6] We indicate the action with S, composite operators with O and their variations under a given symmetry transformation as δO and δS.

[7] Note that we keep $x \neq y$ to avoid contact terms. Eq. (2.19) and eq. (2.20) are still in the continuum theory.

[8] The matrix M_0 can always be expanded as $m_0 \mathbb{1} + m_{0,a}\lambda^a$, ergo the r.h.s. of eq. (2.19) and eq. (2.20) corresponds to the pseudo-scalar operator P.

action is simply $\delta S \propto \sum_x \partial^\star_\mu \tilde{V}_\mu(x)$, with $\partial^\star_\mu$ the lattice backward derivative. The lattice current $\tilde{V}_\mu(x)$, called point-split vector current,

$$\begin{aligned}\tilde{V}_\mu(x) =& \frac{1}{2}\Big[\overline{\psi}(x)\frac{\lambda^a}{2}(\gamma_\mu - 1)U_\mu(x)\psi(x+a\hat{\mu}) + \\ & \overline{\psi}(x+a\hat{\mu})\frac{\lambda^a}{2}(\gamma_\mu + 1)U^\dagger_\mu(x)\psi(x)\Big]\,,\end{aligned} \tag{2.22}$$

is conserved in the limit of degenerate masses, as in the continuum, thus leading to $Z_{\tilde{V}} = 1$. On the other hand the WI associated with the local current $V_\mu(x)$ is conserved only up to lattice artifacts and for this reason it requires a finite renormalization factor $Z_V(g_0)$.

Similarly we can repeat the calculation by applying an axial transformation, $\alpha_V = 0$ in eq. (2.18). In this case the Wilson term $-ar\nabla^\star_\mu\nabla_\mu$ does not simplify and leaves an additional contribution in the axial WI. Indeed, it is not possible to find an axial current which is conserved in the chiral limit, like A_μ in eq. (2.20). Therefore the PCAC relation, both for the point-split axial current $\tilde{A}_\mu$ (which can be defined by replacing $(\gamma_\mu \pm 1) \to \gamma_\mu\gamma_5$) and the local axial current $A_\mu(x)$, defined in eq. (2.21), is violated by $O(a)$ terms [39]. Finite renormalization factors $Z_{\tilde{A}}(g_0)$ and $Z_A(g_0)$ are required in the limit $a \to 0$.

2.2.3 Symanzik's Effective Theory

In addition to the additive renormalization of the bare masses, also operators require additive counter-terms to compensate the breaking of chiral symmetry by Wilson fermions. Their effect is to cancel the leading lattice artifacts of $O(a)$ and gives an effective "acceleration" towards the continuum limit, which is reached at a faster rate.

In a series of papers [40, 41], Symanzik developed a framework where such acceleration, called $O(a)$-*improvement*, can be achieved by interpreting a lattice theory as an effective theory in the continuum. The decoupling theorem [42] states that at energies below a certain threshold, the fields corresponding to heavy particles can be removed from the Lagrangian and their effects absorbed in the coupling constants. At energies far from the cutoff the effects of these particles can be mimicked by adding higher dimensional operators to the effective Lagrangian and fields.

Therefore, assuming that the physics of the lattice action, the "fundamental" theory in this context, can be reproduced up to energies of $O(a^{-2})$ by the continuum actions S_0 and S_1, its low-energy counterparts $S_{\text{eff}} = S_0 + aS_1 + O(a^2)$, the expectation value of an observable $O_{\text{eff}} = O_0 + aO_1 + O(a^2)$ becomes

$$\langle O_{\text{eff}}\rangle = \langle O_0\rangle_0 - a\langle O_0 S_1\rangle_0 + a\langle O_1\rangle_0\,, \quad \langle O\rangle_0 = \mathcal{Z}^{-1}\int [\mathcal{D}\phi] O e^{-S_0}\,. \tag{2.23}$$

So far, we have been very generic without defining the observables. In fact, the description above holds, for instance, for correlation functions at positive non-zero distances,

in which case $\langle \cdots \rangle$ has to be intended as the connected part. At very short distance some observables have contact terms which are not accounted in the effective theory. The operators in O_1 and S_1 can be found by matching the symmetries and quantum numbers of the corresponding O_0 and S_0.

2.3 Full QCD

Starting from the Wilson formulation of QCD, given in eq. (2.14), let us now discuss the complete renormalization pattern to compute renormalized quantities up to a^2 violations. Two additional counter-terms for the gluonic and fermionic action, in accordance with Symanzik's approach, can be added to eq. (2.14)

$$S = S_g + a^2\delta S_g + \sum_{f=1}^{N_{\rm f}} \Big[a^4 \sum_x \overline{\psi}_f(x) D_{\rm W}(m_{0,f}) \psi_f(x) \Big] + a\delta S_F \,, \tag{2.24}$$

The explicit form of the counter-terms can be obtained by listing the independent gauge-invariant operators (with engineering dimension larger than four) sharing the same symmetries of the corresponding action. Within the gauge sector, only three dimension-6 operators are accessible and no dimension-5. For this reason the improvement of the pure gauge action starts at order a^2. Making use of the equations of motion (on-shell improvement), forcing the normalization of the $\mathrm{tr}\, F^2$ as in eq. (2.3) and imposing the improvement of eq. (2.3), gives the Lüscher-Weisz (tree-level) improved action [43]

$$S_g[U] = \frac{1}{g_0^2}\big(c_0 \sum_p \mathrm{tr}\{1 - U(p)\} + c_1 \sum_r \mathrm{tr}\{1 - U(r)\}\big) \,, \quad c_0 = \frac{5}{3} \,, c_1 = -\frac{1}{12} \,, \tag{2.25}$$

where r denotes the flat rectangles. Note that the numbers in eq. (2.25) are the tree-level values of c_0 and c_1 and in principle they could be computed either to higher orders in PT (e.g. to one-loop [44]), or non-perturbatively by forcing the cancellation of cutoff effects in some spectral quantities. The main interest remains in any case QCD, where a full $O(a^2)$ improvement is extremely difficult, as it involves a large basis of operators of dimension 6.

Wilson fermions can be improved in a similar manner. In this case five dimension-5 operators can be found. On-shell improvement removes two of them, whereas two can be re-absorbed in the counter-terms of the bare masses and bare coupling constant, leaving only the Pauli term, best known from the authors Sheikholeslami and Wohlert [45]. Hence the Dirac operator can be re-expressed as

$$D_{\rm W}(m_{0,f}) = \frac{1}{2}\sum_{\mu=0}^{3}\{\gamma_\mu(\nabla^\star_\mu + \nabla_\mu) - a\nabla^\star_\mu\nabla_\mu\} + ac_{\rm sw}\sum_{\mu,\nu=0}^{3}\frac{i}{4}\sigma_{\mu\nu}\widehat{F}_{\mu\nu} + m_{0,f} \,, \tag{2.26}$$

with $\widehat{F}_{\mu\nu}$ discretized using the *clover* definition [46]. Given the $a^2\delta S_G$ term in eq. (2.24), the reader might wonder why we drop a term of the form $a^2\delta S_{F,2}$. As mentioned earlier, such a term consists in a large number of operators of dimension 6, whose treatment is particularly difficult. Therefore, with the choice in eq. (2.24) we do not treat a^2 corrections systematically. Nevertheless we believe that some observables (in particular gluonic ones) might still benefit from the $a^2\delta S_G$ term.

The last step towards the computation of physical observables is renormalization, including Symanzik's improvement. The continuum limit is at $g_0 = 0$ and there exists a unique function relating the lattice spacing and the bare coupling. However, from the previous discussion on $O(a)$-improvement we mentioned that two operators amount to an additional renormalization of the coupling and the masses. Indeed, in a mass-independent renormalization scheme, $\tilde{g}_0$ is the parameter which univocally fixes a [46],

$$g_{\rm R}^2 = Z_g(\tilde{g}_0^2, a\mu)\tilde{g}_0^2\,, \quad \tilde{g}_0^2 = g_0^2(1 + ab_g{\rm tr}M/N_{\rm f})\,. \tag{2.27}$$

Similarly, also the bare subtracted quark masses, introduced before, require multiplicative renormalization

$${\rm tr}M_{\rm R} = Z_m r_m\big[(1 + a\bar{d}_m{\rm tr}M){\rm tr}M + ad_m{\rm tr}M^2\big]\,, \quad \text{with } {\rm tr}M = \sum_f m_{{\rm q},f}\,, \tag{2.28}$$

$${\rm tr}\,(\lambda M_{\rm R}) = Z_m\big[(1 + a\bar{b}_m{\rm tr}M){\rm tr}\,(\lambda M) + ab_m{\rm tr}\,(\lambda M^2))\,. \tag{2.29}$$

According to Ref. [47] we have introduced the parameter r_m, which accounts for the difference between the Z factors of singlet and non-singlet scalar quark bilinears.

According to Symanzik's effective theory also composite operators undergo a similar treatment. Consider the case of the axial current. Four dimension-5 operators share its same quantum numbers, but only three survive in on-shell correlation functions

$$O_1^a = \partial_\mu P^a\,, \quad O_2^a = {\rm tr}\,(\lambda^a M_{\rm val})A_\mu^a\,, \quad O_3^a = {\rm tr}MA_\mu^a\,. \tag{2.30}$$

We have considered here the most generic case with valence quarks $M_{\rm val}$ in the propagators different from the sea quarks M. Since O_2 and O_3 amount to a redefinition of the bare local current, renormalization is usually split in two steps. Firstly an *improved* bare operator is defined in the chiral limit

$$A_{\mu,{\rm I}}^a(x) = A_\mu^a(x) + ac_A\frac{1}{2}(\partial_\mu + \partial_\mu^\star)P^a(x)\,. \tag{2.31}$$

Secondly it is renormalized according to

$$A_{\mu,{\rm R}}^a(x) = Z_A(\tilde{g}_0^2)(1 + a\bar{b}_A{\rm tr}M + ab_A{\rm tr}\,(\lambda^a M_{\rm val}))A_{\mu,{\rm I}}^a(x)\,. \tag{2.32}$$

For the pseudo-scalar current P no operators like O_1^a exist. Hence it is already improved and only multiplicative renormalization is required to cancel $O(a)$ effects

$$P_{\mu,{\rm R}}^a(x) = Z_P(\tilde{g}_0^2, a\mu)(1 + a\bar{b}_P{\rm tr}M + ab_P{\rm tr}\,(\lambda^a M_{\rm val}))P_\mu^a(x)\,. \tag{2.33}$$

The various improvement coefficients are functions of the bare coupling alone. The values we quote for c_0 and c_1 come from a tree-level computation in perturbation theory, while $c_{\rm sw}$ is often computed non-perturbatively by forcing the PCAC relation. The Schrödinger functional, that we mentioned in Chapter 1, turns out to be a particularly convenient setup for this calculations [46]. In fact, the coefficient b_g has been obtained to 1-loop in Ref. [48] and starts at $O(g_0^2)$. A tree-level calculation shows that $b_m = d_m = -\frac{1}{2} + O(g_0^2)$ and b_A,$b_P = 1 + O(g_0^2)$. They account for valence quark effects in the observables, such as, in correlation functions involving axial or pseudo-scalar currents, while the coefficients $\bar{b}_X$ account for sea effects. Hence, they start at $O(g_0^4)$ since they contribute through quark loops to the gluon self-energy.

Before continuing, it is worth mentioning that the approach that we have outlined to cancel $O(a)$ lattice artifacts is not unique. For Wilson fermions there exists a second approach where $O(a)$-improvement is achieved automatically. The *twisted-mass* discretization of QCD (tmQCD) for a doublet of quarks with the same bare mass m_0

$$S = a^4 \sum_x \overline{\psi}(x)(D_{\rm W} + m_0 + i\mu\tau^3\gamma_5)\psi(x)\,, \tag{2.34}$$

was originally introduced to overcome the problem of configurations with fermionic zero modes [49, 50]. The action written above (once translated in the formal continuum theory) can be related to the standard QCD action with a global rotation in the chiral-flavor group of the spinor fields, $\psi \to \exp(i\frac{\alpha}{2}\tau_3\gamma_5)\psi$. Hence, correlation functions in standard QCD are mapped into correlation functions of tmQCD and for chiral multiplets the relation between the two is simply linear.

Let us now (briefly) describe the effective approach à la Symanzik to investigate the structure of the $O(a)$ counter-terms. Similarly to what we have seen before, the lattice action and observables are expanded in the effective field theory in terms of a leading contribution S_0, and counter-terms S_1 and O_1 sharing their same quantum numbers and symmetries. Note that S_0 is understood to be the formal continuum action corresponding to eq. (2.34), therefore the mass parameter is given by the bare subctracted quark mass. S_1 contains as before the Pauli-term, together with a mass-like term proportional to $\mu^2\overline{\psi}\psi$ (and additional dimension-5 operators which can be eliminated with the equation of motion). If the bare subctrated quark mass vanishes, meaning that $m_0 = m_{\rm cr}$, the action S_0 is invariant under the $\gamma_5\tau_1$-transformation $\psi \to i\gamma_5\tau_1\psi$. This situation is often referred to as *maximal twist*, since the twist angle $\alpha = \pi/2$ ($\tan\alpha \propto \mu/(m_0 - m_{\rm cr})$). Unlike S_0, S_1 is odd under this transformation, while for O_1 the following condition holds: $O^{\rm even} \to O_1^{\rm odd}$ and viceversa. Therefore, for all even correlation functions (under the $\gamma_5\tau_1$-transformation) the leading contributions in the Symanzik approach start at order a^2, while the odd ones vanish up to $O(a)$ discretization errors. Hence, automatic $O(a)$ improvement is obtained in tmQCD at maximal twist and in practice the tuning of $c_{\rm sw}$ is replaced by $\kappa_{\rm cr}$.

Within the CLS effort, the decision to use standard Wilson fermions (with the $c_{\rm sw}$ term in the action) was taken mostly to preserve the usual flavor and parity symmetries, which are broken in the twisted-mass regularization and recovered only in the continuum limit.

2.4 Transfer matrix and correlation functions

To extract physical information from the lattice version of QCD, unitarity must be satisfied and demonstrating the existence of a hermitian Hamiltonian operator is sufficient.

For simplicity, let us start with the interacting scalar theory ϕ^4 discretized in a periodic box L^3. Only in this Section we set the lattice spacing to 1. For later convenience let us also impose the boundary conditions in time $\phi(0,\vec{x}) = \phi_{\rm i}(\vec{x})$ and $\phi(T,\vec{x}) = \phi_{\rm f}(\vec{x})$. The Hilbert space is given by the direct product of the eigenstates of the field operator $\hat{\phi}(\vec{x})$

$$\hat{\phi}(\vec{x})|\phi(\vec{x})\rangle = \phi(\vec{x})|\phi(\vec{x})\rangle\,, \quad |\phi\rangle = \otimes\prod_{\vec{x}}|\phi(\vec{x})\rangle\,. \tag{2.35}$$

The Fock space of the theory is given by the direct sum of the various Hilbert spaces $|\phi_n\rangle$ living on the time slices n of the lattice (by restoring the lattice spacing, n would be x_0/a). The original action $S = \sum_x \mathcal{L}(x)$, depending on the discretized Lagrangian $\mathcal{L}(x)$, can be rewritten as a sum over time slices $S = \sum_n \mathcal{L}(n+1,n)$, with $\mathcal{L}(n+1,n)$ given by

$$\mathcal{L}(n+1,n) = \sum_{\vec{x}} \frac{1}{2}\big[\phi(n+1,\vec{x}) - \phi(n,\vec{x})\big]^2 + V\big(\phi(n)\big)\,, \tag{2.36}$$

where we have introduced the potential V, which contains the mass term and the quartic interaction and does not couple adjacent time slices. Following the Schrödinger picture (eq. (2.35)), we can define the action on a state $|\phi_n\rangle$ of the operator corresponding to $\mathcal{L}(n+1,n)$ as

$$\mathcal{L}(n+1,n) = \langle\phi_{n+1}|\Big\{\frac{V[\hat{\phi}]}{2} + \sum_{\vec{x}}\frac{\hat{\pi}^2(\vec{x})}{2} + \frac{V[\hat{\phi}]}{2}\Big\}|\phi_n\rangle\,, \tag{2.37}$$

with $\hat{\pi}(\vec{x})$ the operator satisfying the canonical commutation relations with $\hat{\phi}(\vec{x})$. The Boltzman weight e^{-S} can be expressed as a product over times slices of the factor $e^{-\mathcal{L}(n+1,n)}$ to which we associate the operator $\hat{T}$. The latter evolves the state $|\phi_n\rangle$ into $|\phi_{n+1}\rangle$ and is called *Transfer Matrix*,

$$e^{-\mathcal{L}(n+1,n)} = \langle\phi_{n+1}|\hat{T}|\phi_n\rangle\,, \quad \hat{H} \equiv -\ln\hat{T}\,. \tag{2.38}$$

Since it is hermitian and positive definite, there exists a Hamiltonian operator fulfilling eq. (2.38). The partition function of the scalar theory can consequently be re-written in terms of the Transfer Matrix as

$$\mathcal{Z} = \int\prod_x d\phi(\vec{x})e^{-S[\phi]} = \langle\phi_{\rm f}|\hat{T}^T|\phi_{\rm i}\rangle = \langle\phi_{\rm f}|e^{-T\hat{H}}|\phi_{\rm i}\rangle\,, \tag{2.39}$$

satisfying the boundary conditions that we imposed before. Note that for periodic boundary conditions in time, $|\phi_{\rm f}\rangle = |\phi_{\rm i}\rangle$, eq. (2.39) becomes the usual $\mathrm{Tr}\,(e^{-T\hat{H}})$.

Poincaré invariance of the continuum theory implies the existence of a unitary operator responsible for translations. A lattice version of this operator exists as well, corresponding to finite jumps between neighboring sites. Its simultaneous diagonalization with the Hamiltonian $\hat{H}|\vec{p},n\rangle = E_n(\vec{p})|\vec{p},n\rangle$ provides a complete basis of the Fock space (n indicates any quantum number and $\vec{p}$ the momentum of the state). Assuming the following normalization $\langle\vec{p},n|\vec{q},m\rangle = \delta_{mn}\delta(\vec{p}-\vec{q})2E_n(\vec{p})L^3$ the partition function, for sufficiently large T, becomes

$$\mathcal{Z} = \frac{1}{L^3}\sum_{\vec{p},n}\frac{1}{2E_n(\vec{p})}\langle\phi_{\rm f}|\vec{p},n\rangle e^{-TE_n(\vec{p})}\langle\vec{p},n|\phi_{\rm i}\rangle \overset{T\to\infty}{\to} \langle\phi_{\rm f}|0\rangle e^{-TE_0}\langle 0|\phi_{\rm i}\rangle\,, \tag{2.40}$$

where we have used the completeness of the Hilbert space (with some abuse of notation to keep the previous sum over $\vec{p}$ and n compact)

$$\mathbb{1} = \frac{1}{2E_n(\vec{p})L^3}\sum_{\vec{p},n}|\vec{p},n\rangle\langle\vec{p},n|\,, \quad \text{with} \quad \frac{|\vec{0},0\rangle\langle\vec{0},0|}{2E_0(\vec{0})L^3} \equiv |0\rangle\langle 0|\,. \tag{2.41}$$

The ground state of the Hamiltonian $|0\rangle$ defines the vacuum with energy $E_0 = E_0(\vec{0})$ and it is normalized to one. Note that in eq. (2.40) we have used an important assumption on the boundary states: they share the same quantum numbers of the vacuum and therefore in the limit $T\to\infty$ only E_0 survives. This statement does not mean that $|\phi_{\rm f,i}\rangle = |0\rangle$, but rather that it is a linear combination of all the states with vacuum quantum numbers.

Let us now discuss a two-point function of a generic operator $\hat{O}$. Using the Transfer Matrix we can derive its quantum mechanical representation

$$\langle O(x)O(y)\rangle = \mathcal{Z}^{-1}\langle\phi_{\rm f}|e^{-(T-x_0)\hat{H}}\hat{O}(\vec{x})e^{-(x_0-y_0)\hat{H}}\hat{O}(\vec{y})e^{-y_0\hat{H}}|\phi_{\rm i}\rangle\,. \tag{2.42}$$

If we insert many times a complete basis of states $|\vec{p},n\rangle$, we obtain the following expression

$$\begin{aligned}\langle O(x)O(y)\rangle =& \mathcal{Z}^{-1}\frac{1}{L^9}\sum_{n,m,l}\sum_{\vec{p},\vec{q},\vec{s}}\frac{1}{2^3E_n(\vec{p})E_m(\vec{q})E_l(\vec{s})}\langle\phi_{\rm f}|\vec{q},m\rangle e^{-(T-x_0)E_m(\vec{q})}\\ &\times\langle\vec{q},m|\hat{O}(\vec{x})|\vec{p},n\rangle e^{-(x_0-y_0)E_n(\vec{p})}\langle\vec{p},n|\hat{O}(\vec{y})|\vec{s},l\rangle e^{-y_0E_l(\vec{s})}\langle\vec{s},l|\phi_{\rm i}\rangle\,.\end{aligned} \tag{2.43}$$

The two exponential terms with temporal arguments $T-x_0$ and y_0 produce contributions coming from the boundary states, if they are not taken sufficiently large. On the other hand if $(T-x_0)\,, y_0 \to \infty$ the surviving contributions are those with $E_m(\vec{q})$ and $E_l(\vec{s})$ equivalent to E_0 and they cancel with e^{-E_0T} coming from the inverse partition function. This means that all the energies of the states propagating between the two operators $\hat{O}$ are correctly normalized with the ground state energy $\tilde{E}_n(\vec{p}) \equiv E_n(\vec{p}) - E_0$. Note that also

that the matrix elements $\langle\phi_{\mathrm{f}}|0\rangle$ and $\langle 0|\phi_{\mathrm{i}}\rangle$ drop out in the ratio thus leaving the familiar vacuum expectation value of the two-point correlator

$$\langle O(x)O(y)\rangle = \frac{1}{L^3}\sum_{\vec{p},n}\frac{1}{2E_n(\vec{p})}\langle 0|\hat{O}(\vec{x})|\vec{p},n\rangle e^{-(x_0-y_0)\tilde{E}_n(\vec{p})}\langle\vec{p},n|\hat{O}(\vec{y})|0\rangle\,. \tag{2.44}$$

Now using the translation operator (which commutes with $\hat{H}$) on the two $\hat{O}$ and assuming that the vacuum state is invariant under spatial translations, the two-point function becomes the well-known Källen-Lehmann representation

$$\begin{aligned}\langle O(x)O(y)\rangle =&\frac{1}{L^3}\sum_{\vec{p},n}\frac{e^{i\vec{p}\cdot(\vec{x}-\vec{y})}}{2E_n(\vec{p})}|\langle\vec{p},n|\hat{O}|0\rangle|^2 e^{-(x_0-y_0)(E_n(\vec{p})-E_0)}\\ =&\frac{1}{L^3}\sum_{\omega,\vec{p}}\rho(\omega,\vec{p})e^{-\omega(x_0-y_0)}e^{i\vec{p}\cdot(\vec{x}-\vec{y})}\,.\end{aligned} \tag{2.45}$$

In the thermodynamic limit, the sum becomes an integral and the spectral density ρ a function of a continuous spectrum. From eq. (2.45) it is straightforward to demonstrate that an additional sum either over $\vec{x}$ or $\vec{y}$ corresponds to the zero-momentum projection, which leads to the extraction of particle masses.

A Transfer Matrix can be calculated as well for free Wilson fermions. The representation of states clearly changes in favor of Grassman variables, but a positive hermitian Transfer Matrix can be found in a similar manner. More precisely, is the choice $r = 1$ which guarantees its positivity.

Wilson's formulation of the interacting theory is gauge-invariant. In that case care must be taken in the construction of a Hilbert space, since all the wave functions related by a gauge transformation are physically equivalent. However, during the derivation, one finds that an operator projecting onto physical states automatically comes out from the plaquette action introduced before. This operator can be added to the Transfer Matrix without spoiling its positivity. Eventually, proving the positivity of the gauge and the fermionic Transfer Matrix separately is enough to guarantee the unitarity of lattice QCD [51].

The spectrum of the QCD Hamiltonian can not be solved due to its non-linearity. Nevertheless, through the experimental knowledge of the hadronic spectrum, it is possible to predict the "tower of eigenstates" and test the validity of the theory. Let us consider the lightest mesons: the pions. The quantum numbers of the charged ones are $J^P = 0^-$ and suitable interpolating operators are $P^{ud} = \overline{\psi}^u\gamma_5\psi^d$ and $A_0^{ud} = \overline{\psi}^u\gamma_0\gamma_5\psi^d$ (they create a pion state from the vacuum, as they share the same quantum numbers). Therefore by computing the following correlation functions, we can extract their mass m_π and decay constants G_π and F_π from the large time behavior (we indicate with $|\pi\rangle$ a state with a

charged pion with momentum zero)

$$\lim_{x_0\to\infty}\sum_{\vec{x}}\langle P^{ud}(x)P^{du}(0)\rangle \approx G_\pi^2 e^{-m_\pi x_0}\,, \quad G_\pi = |\langle 0|\hat{P}|\pi\rangle|\,. \tag{2.46}$$

$$\lim_{x_0\to\infty}\sum_{\vec{x}}\langle A_0^{ud}(x)P^{du}(0)\rangle \approx G_\pi F_\pi e^{-m_\pi x_0}\,, \quad F_\pi = \langle 0|\hat{A}_0|\pi\rangle\,. \tag{2.47}$$

The calculations that we showed in this Section, on the Transfer Matrix in a theory with boundaries, will be very useful in the next Chapters, where lattice QCD with open boundary conditions will be discussed. Let us anticipate already here that the notation for the boundary states will change from $|\phi_{\mathrm{f,i}}\rangle$ to $|\Omega\rangle$.

2.5 Universality

The universality of the continuum limit leaves room to many possibilities in the discretization of the Dirac Lagrangian. Even though, this work is based on the Wilson formulation, other options exist.

We have already introduced tmQCD and listed some of its properties. Let us mention here that the twisted-mass discretization of QCD admits a positive and hermitian Transfer Matrix [52] and it has the correct continuum limit, where parity and flavor symmetries, broken by the twisted-mass parameter, are restored.

A different approach to the doubling problem, was considered by Kogut and Susskind in 1975 [53]. It reduces the doublers from 2^D to $2^{D/2}$ by using some of the unphysical fermions to build the 4 components of a Dirac field in the continuum. In this formulation, also known as *staggered*, the spinor/flavor structure becomes more complicated and the Transfer Matrix is positive, only if defined between the time slices at x_0 and $x_0 + 2a$. A proof, despite numerical findings, of the renormalizibility (to all orders in PT) and universality has not been yet derived.

Finally, even if Neuberger's operator (see next Section) is the only known solution to the GW problem, fermions in a 5D theory coupled to a *domain-wall* produce chiral states in the 4D bulk [54, 55, 56]. The overlap operator has been shown to be equivalent to a formulation with an infinite domain wall [57, 58].

2.6 Ginsparg-Wilson fermions

In Ref. [59] Ginsparg and Wilson, starting from a continuous chirally-invariant fermion operator D, studied how chiral symmetry is minimally broken by the lattice discretization, treated in the paper as a block spin transformation. They argued that (the usual form of) chiral symmetry in the lattice formulation is broken by an irrelevant operator and that

D obeys the relation

$$\{\gamma_5, D\} = aD\gamma_5 D\,. \tag{2.48}$$

Clearly Wilson's operator in eq. (2.10) does not obey eq. (2.48) and it took almost ten years to discover a discretization of the Dirac operator, which fulfills the Ginspag-Wilson relation

$$D = 1 + \gamma_5 \frac{Q_{\rm W}}{\sqrt{Q_{\rm W}^2}}\,, \quad Q_{\rm W} = \gamma_5 D_{\rm W}\,, \tag{2.49}$$

known as the Overlap operator [60, 61, 62]. So far, it remains, apart from modification of $D_{\rm W}$, the only known explicit realization of eq. (2.48).

Afterwards, in '98, Lüscher demonstrated that eq. (2.48) automatically defines a "lattice chiral symmetry" which is preserved by D at finite a [63],

$$\psi \to (1 + i\varepsilon\tau\hat{\gamma}_5)\psi\,, \quad \hat{\gamma}_5 = \gamma_5\Big(1 - \frac{a}{2}D\Big)\,, \quad \bar{\psi} \to \bar{\psi}\Big[1 + i\varepsilon\tau\Big(1 - \frac{a}{2}D\Big)\gamma_5\Big]\,, \tag{2.50}$$

and becomes the usual chiral transformation in the naive continuum limit. Let us stress once more the validity of the Nielsen-Ninomiya theorem. As a no-go theorem it prevents us from constructing the local theory for fermions we would like. However, if property 3 is violated by a lattice artifact according to eq. (2.48) the theorem does not hold any more and the overlap operator proves that a local, invertible and chiral discretization of the fermionic action is possible. In fact, even if the denominator in eq. (2.49) couples all points together, such coupling falls off exponentially with the distance [64].

The exact version of chiral symmetry, realizable at finite a with the overlap operator, protects the renormalization of the mass from additive terms. By using $\tau \in \mathfrak{su}(N_{\rm f})_L \otimes \mathfrak{su}(N_{\rm f})_R$ in the transformation laws in eq. (2.50) (assuming $N_{\rm f}$ GW fermions), the correct PCVC and PCAC relations are reproduced also here, now without $O(a)$ terms.

2.6.1 Anomalies and topology

Only the $U(1)$ transformations remain to be tested. If $\tau \in \mathfrak{u}(1)_V$, from Lüscher's chiral rotations, a conserved WI, associated to the quark number, is obtained. In formal continuum QCD this is also the case, whereas since the '60s it is well-known that the $U(1)_A$ symmetry, preserved at tree-level, is broken at 1-loop [65, 66]

$$\partial_\mu J^5_\mu = \frac{g_0^2}{16\pi^2}\,\epsilon_{\mu\nu\rho\delta}\,{\rm tr}\,\{F^{\mu\nu}F^{\rho\delta}\}\,. \tag{2.51}$$

This feature, known as the $U(1)_A$ problem, has important physical consequences and it is a requirement for a discretized theory of QCD. For GW fermions, $\tau \in \mathfrak{u}(1)_A$ induces

a transformation in the measure[9] $\delta[d\psi d\overline{\psi}] \to [d\psi d\overline{\psi}] a\mathrm{Tr}\,(\gamma_5 D)$. Using the fact that the eigenvalues of D satisfying eq. (2.48) lie exactly on a circle and that the zero modes are chiral, it is possible to demonstrate that

$$a\mathrm{Tr}\,(\gamma_5 D) = 2(n_- - n_+)\,, \tag{2.52}$$

with $n_\pm$ the number of Right(Left)-Handed zero modes. Therefore, the $U(1)_A$ symmetry is anomalous for GW fermions as well.

For a massless Dirac operator in the formal continuum theory, the winding number of the gauge manifold, called the *topological charge* Q

$$Q = -\frac{1}{32\pi^2}\int d^4x\ \epsilon_{\mu\nu\rho\delta}\ \mathrm{tr}\,\{F^{\mu\nu}F^{\rho\delta}\} \tag{2.53}$$

is related to the number of zero modes $Q = (n_- - n_+)$ through the famous Atiyah-Singer index theorem [67]. Turning back to GW fermions, if we define a local topological charge density through the anomalous term induced by the $U(1)_A$ transformation $q(x) = \frac{a}{2}\mathrm{tr}\,(\gamma_5 D(x,x))$, thanks to eq. (2.52) the associated topological charge is integer and homotopically invariant. Therefore, the index theorem is also valid for GW fermions, even if the density $q(x)$ correctly reproduces the integrand in eq. (2.53) only for sufficiently smooth configurations[10].

We have briefly sketched how the $U(1)_A$ problem is satisfied by GW fermions: at this point the reader can convince himself that the same happens also for Wilson fermions in the continuum limit, where chiral symmetry is restored.

At first sight it is not immediately clear that topology is realized at finite lattice spacing, for gauge field configurations where continuity in space is replaced by finite steps. However, in Ref. [69] Lüscher noted that under the smoothness condition

$$\mathrm{Re}\,\mathrm{tr}\,[1 - U(p)] < \varepsilon\,, \quad \varepsilon = 0.067\,, \tag{2.54}$$

the space of fields splits into topological sectors, homotopically inequivalent (see Appendix A), as in the continuum theory. Note that the bound in eq. (2.54) must be satisfied by all the plaquettes in the lattice and configurations violating this bound provide regions in fields space, which continuously connect the different sectors with each others. For those fulfilling eq. (2.54), the realization of the $F_{\mu\nu}$ tensor given in Ref. [69] correctly reproduces their corresponding integer topological charge (often called geometrical definition).

[9] We denote the trace over color and spinor indices with tr, while we use Tr to indicate also the sum over space-time.

[10] In Ref. [68] it has been proven that the index theorem, where one side of the equation is given by Q in eq. (2.53), holds, at finite lattice spacing, for the Fixed Point Dirac operator satisfying the GW relation.

The gauge-field configurations which are used in lattice computations are always too "rough" to satisfy eq. (2.54) and therefore the notion of topology is lost. Moreover, provided a certain discretization of the field strength tensor, the topological susceptibility corresponding to the charge density in eq. (2.53) is known to suffer from short-distance singularities. Therefore a good definition of the topological charge is such that the corresponding susceptibility is finite in the continuum limit. This is the case for the density $q(x)$ defined through the anomalous flavor-singlet Ward Identities for a Dirac operator satisying the GW relation [70, 71, 72].

Recently, in Refs. [7, 8], a theoretical framework has been devised, where the UV modes of the gauge fields can be removed with controlled systematic errors: the so-called *Wilson (or Gradient) flow* defined by the equation

$$\partial_t V_t(x,\mu) = -g_0^2\{\partial_{x,\mu} S_{\rm W}(V_t)\}V_t(x,\mu)\,, \quad V_t(x,\mu)\big|_{t=0} = U_\mu(x)\,, \tag{2.55}$$

with t a positive square length called flow-time. Let us only-briefly mention its relevant properties:

- the action monotonically decreases with t thus leading to smoothed gauge fields V_t;
- correlation functions of purely gluonic observables, such as the energy density $E(t)$, are automatically finite at $t > 0$ [73, 74];
- the dimensionless quantity $t^2E(t)$ can be used to define a renormalized coupling and therefore a scale for lattice simulations; concerning the latter the following definitions have been proposed [8, 21, 75]

$$\begin{gathered}\langle t^2E(t)\rangle\big|_{t=t_0} = 0.3\,, \quad \langle t^2E(t)\rangle\big|_{t=t_1} = \frac{2}{3}\,, \\ t\partial_t\langle t^2E(t)\rangle\big|_{\sqrt{t}=w_0} = 0.3\,.\end{gathered} \tag{2.56}$$

Now, given the properties of the Wilson flow, let us turn once more to topology. Firstly, we note that the topological charge defined from smoothed links at positive flow time generates a finite susceptibility in the limit $a \to 0$. Numerical evidences in Ref. [8] support the conjecture that it has the correct continuum limit in the pure gauge theory. Secondly, the Wilson flow induces a bijective map between the original U fields and V_t. Therefore sectors in the U-field space are mapped into sectors of the space of the smoothed fields, which might be used to study the topology of the corresponding gauge configurations. However the smoothness condition in eq. (2.54), which we re-write here for the fields at positive flow time,

$$s_{\rm p}(t) < 0.067\,, \quad s_{\rm p}(t) = {\rm Retr}\,[1 - V_t(p)]\,, \tag{2.57}$$

is never satisfied by all plaquettes. The object studied in Ref. [8] is the probability for smoothed plaquettes to exceed the bound 0.067, namely

$$P_t(s_{\rm cut}) \propto \langle \sum_p \theta(s_p(t) - s_{\rm cut})\rangle\,, \quad s_{\rm cut} = 0.067\,, \tag{2.58}$$

and what is found there, through numerical studies, is that it decreases with a^{10} towards the continuum limit, or a^6 in a fixed volume. Hence, one concludes that topological sectors appear dynamically in the limit $a \to 0$. Additional explanations can be found in Refs. [8, 9].

We prefer to interrupt here the discussion and describe the Monte Carlo techniques presently used to sample the field space. In the second part of Chapter 3 we will comment on the relevance of topology for algorithms. The study of topology on the lattice has a long history and in this thesis we have discussed only some aspects. In this introductive Chapter we have only mentioned a few techniques presently used to compute the topological charge on the lattice. For a recent review on the various methods available and other topology-related problems, such as the study of instantons and calorons, we point the reader to Ref. [76] and references therein.

3 Modern QCD Simulations

The basics of the lattice discretization of QCD and its renormalization has been explained. In this Chapter we will describe how, in practice, expectation values are computed by means of Numerical Simulations.

In the path integral formalism, expectation values of observables of a certain QFT are obtained essentially by computing integrals

$$\langle O \rangle = \mathcal{Z}^{-1} \int [\mathcal{D}U]\, e^{-S[U]}\, O[U]\,. \tag{3.1}$$

Monte Carlo methods are based on the general idea that

$$\frac{1}{b-a}\int_a^b dx f(x) \approx \frac{1}{N}\sum_i f(x_i) \equiv \langle f \rangle\,, \tag{3.2}$$

with randomly-chosen $x_i \in [a,b]$. The error on the estimator $\langle f \rangle$ scales with $1/\sqrt{N}$, but if the function is peaked somewhere the convergence is terribly slow. Indeed it would be much better if we could sample the points x_i according to their relevance (better to stay in the region of the peak and do *importance sampling*) modulated by a certain probability distribution P

$$\int dx P(x) \frac{f(x)}{P(x)} \approx \frac{1}{N}\sum_i \frac{f(x_i)}{P(x_i)}\,, \tag{3.3}$$

and ideally $P = f$ ($f \geq 0$ is assumed) would bring the variance to zero. Making a proposal of an x distributed according to P requires the knowledge of its normalization. In terms of eq. (3.1) it translates in the knowledge of the partition function and eventually, the only way out is to consider relative probabilities where the normalization cancels. Given an initial field configuration x_0, distributed according to P_0, the subsequent application of a *Transition probability* $T(x_{i+1} \leftarrow x_i)$ generates a so-called *Markov Chain* $x_0 \to x_1 \to x_2 \cdots \to x_N$. Stability, ergodicity and normalization to one are the properties which T must satisfy to guarantee that in the long run the sampling of fields will be done according to P, regardless of the initial P_0.

The Metropolis-Hastings algorithm [77, 78] has been the first proposal for a practical implementation of T and it works in two steps:

1. a new configuration x_1 is drawn with probability $W(x_1 \leftarrow x_0)$, satisfying the symmetry $W(x_1 \leftarrow x_0) = W(x_0 \leftarrow x_1)$;

2. the acceptance probability $P_{\text{acc}}(x_1, x_0)$ is computed and x_1 is accepted if $P_{\text{acc}}(x_1, x_0) > r$ (r is a random number $0 \leq r < 1$).

This procedure defines a transition matrix $T(x_1 \leftarrow x_0) = W(x_1 \leftarrow x_0)P_{\text{acc}}(x_1, x_0) + \delta_{y,x_1} \sum_y W(y \leftarrow x_0)(1 - P_{\text{acc}}(y, x_0))$ which fulfills all the requirements above.

Hence we can conclude that *autocorrelation* among successive configurations is the price to pay for the removal of any reference to the normalization of P in Markov chain processes.

3.1 Algorithms for Lattice QCD

In the Metropolis algorithm making a good proposal for the acceptance-rejection step is very important and the classical Hamiltonian formalism is exactly what we need. The reason lies in the fact that the Hamilton-Jacobi equations of motion divide the space of canonical coordinates and momenta in surfaces of constant Hamiltonian (Liouville's theorem). Hence $W(U' \leftarrow U)$ can be formulated by (i) extending the field space by adding conjugate momenta to the link variables

$$\mathcal{Z} = \int [\mathcal{D}U][\mathcal{D}\pi] e^{-H[\pi,U]}\,, \quad H[\pi, U] = \frac{1}{2} \sum_{x,\mu,a} \pi^a_\mu(x)\pi^a_\mu(x) + S[U]\,, \tag{3.4}$$

and (ii) solving the equations of motion in a fictious Monte Carlo time τ

$$\dot{\pi}_\mu(x) = -\sum_a \frac{\partial S[e^\omega U]}{\partial \omega^a(x,\mu)}\bigg|_{\omega=0} T^a = -\sum_a F^a_\mu(x)T^a\,, \quad \dot{U}_\mu(x) = \pi_\mu(x)U_\mu(x)\,. \tag{3.5}$$

Here, we denote the generators of the group with T^a, a being a color index. Thanks to the conservation of the Hamiltonian, the Boltzmann factor e^{-H} is constant. However in lattice simulations the equations above are solved by numerical integration, which is correct up to $O(\epsilon^k)$ (ϵ being the step-size of the integrator and $k \geq 1$) and W is never exact; still, U' can always be considered as a proposal for the acceptance-rejection step. Since we are interested in ratios of probability density functions, it can be formulated in terms of the following acceptance probability

$$P_{\text{acc}} = \min\left[1, \exp(H[\pi, U] - H[\pi', U'])\right]. \tag{3.6}$$

Note that if the integration were exact, flipping the sign of the conjugate momenta and solving the Molecular Dynamics (MD) again would bring us from U', back to the original field configuration U. Hence it is important for the integrators to satisfy *reversibility* exactly, because together with the symmetric distribution $e^{-\pi^2/2}$ this ensures the symmetry of $W(U' \leftarrow U)$. With numerical integrators rounding errors and approximate inversions of the Dirac operator may become an issue (even if they are small, they accumulate along

the trajectories). In our simulations we performed reversibility checks on some trajectories by solving the MD equations "backwards" in the Monte Carlo time, $U \stackrel{\pi}{\to} U' \stackrel{-\pi}{\to} U''$, and computing the difference between U and U'' (given a certain definition of a distance in the group manifold). The step-sizes have been adjusted to keep this difference sufficiently small to guarantee the ergodicity of the algorithm.

The algorithm that we introduced above is called Hybrid Monte Carlo (HMC) [79] and can be implemented as follows:

1. generation of π with gaussian distribution[1];
2. computation of the forces F^a_μ;
3. evolution $(\pi, U) \to (\pi', U')$ through the solution of the discretized Hamilton-Jacobi equations of motion for a length τ, which is expressed in Molecular Dynamics Units (MDU); these equations have to be symplectic, since eqs. (3.5) preserve the volume in phase space;
4. computation of $P_{\rm acc}$ and acceptance if $P_{\rm acc} \geq r$, $0 \leq r < 1$.

3.1.1 Molecular Dynamics

As we mentioned numerical integrators solve the MD equations up to errors of $O(\epsilon^k)$. But is still true that they are symplectic? Yes, if $\dot{U}$ and $\dot{\pi}$ are separately exact. Any combination of two micro-canonical updates defines an area-preserving integrator.

The simplest integrator is called *leap-frog* and has $k = 1$. Omelyan, Mrygold and Folk in Ref. [80] reviewed many possibilities for higher order integrators, such as second and fourth order ones. They are based on successive applications of $\dot{U}$ and $\dot{\pi}$ with appropriate weights to cancel the various contributions of Taylor expansions in ϵ, such that at the end of a trajectory only terms proportional to ϵ^k are present. From this it is clear that higher order integrators cost more, but the real problem is their stability: up to which step-size the expansion works and what happens afterwards are still open questions. In particular it is known that large forces cause instabilities with too large step-sizes.

A second interesting observation is that the various forces can be integrated also on different time scales [81], as their magnitude can be very different. Several integrators can be nested together and small forces, which correspond typically to the more expensive part of the computation, are integrated on the outer level, thus achieving a global acceleration.

3.1.2 Fermions at work

Computers can perform all the basic operations, such as sums, multiplications and divisions. In a physics language, we would say that a computer can treat bosonic variables.

[1] Note that here the normalization is known.

The same statement does not hold for Grassman variables. Assuming a Hilbert space of n identical fermionic variables, the creation and annihilation operators could be represented by $2^n \times 2^n$ matrices acting on states like $|0, 1, \ldots, 0, 1, 0\rangle$. The limitations in memory and cpu resources clearly do not allow to treat such a system on a computer.

Fortunately, the fermions can first be integrated out and the resulting determinant can be rewritten with bosonic fields again, called *pseudo-fermions* [82]. In the following we will often make use of γ_5-hermiticity of Wilson fermions by replacing $D^\dagger D$ with Q^2 ($Q = \gamma_5 D$) and we will drop the subscript W in Q_W and D_W since no other choices will be considered for the discretized Dirac operator. For simplicity we consider a theory with 2 degenerate flavors

$$\begin{aligned} \mathcal{Z} &= \int [\mathcal{D}U][\mathcal{D}\psi][\mathcal{D}\overline{\psi}]\; e^{-S_g[U] - 2\sum_x \overline{\psi} D[U] \psi} = \int [\mathcal{D}U]\, \det{}^2(D)\, e^{-S_g[U]} \\ &= \int [\mathcal{D}U][\mathcal{D}\phi][\mathcal{D}\phi^\dagger]\; e^{-S_g[U] - \sum_x \phi^\dagger (D^\dagger D)^{-1} \phi} = \int [\mathcal{D}U][\mathcal{D}\phi][\mathcal{D}\phi^\dagger]\; e^{-S_\mathrm{eff}[U]}\,. \end{aligned} \tag{3.7}$$

The ideal treatment of the determinant would be $S_\mathrm{eff} \propto -\log\det(D^\dagger D) = -\mathrm{tr}\,\log Q^2$, but its evaluation is too expensive since D is a large matrix, whereas the pseudo-fermions allow a feasible stochastic computation.

If the determinant is practically impossible to evaluate, also the solution of the Dirac equation is not cheap. In the computation of the force it is required twice,

$$F \simeq -\phi^\dagger Q^{-2} (\delta Q) Q^{-1} \phi\,, \tag{3.8}$$

and various (iterative) methods exist to solve this problem. In this case, as in the following, a better understanding of the physics led to great advances[2].

Clearly there is a certain freedom in writing the fermionic contributions. This can be exploited in practice to reduce the cost of simulations. One such example is the Hasenbusch preconditioning [84, 85]

$$\det Q^2 = \det \frac{Q^2}{Q^2 + \mu_1^2} \det \frac{Q^2 + \mu_1^2}{Q^2 + \mu_2^2} \cdots \det(Q^2 + \mu_N^2) \tag{3.9}$$

which is very similar to the Domain Decomposition [86], as both try to separate the infrared modes from the rest of the spectrum via an infrared regulator: a mass μ or a physical (domain) length L. The latter consists in fixing the links at the border of the domains and in performing the updates only inside, which results in larger autocorrelations.

Why and how the Hasenbusch preconditioning works in practice has been studied in Ref. [87]. We report here the conclusion of the calculations performed in that work, which

[2] We leave the topic about the so-called *solvers* to the reader (for an extensive introduction see the lectures in Ref. [83] and references therein).

are based on the recently-developed Shadow Hamiltonian approach [88, 89]. In the end what really matters in the acceptance step is the difference $\delta H = H[\pi', U'] - H[\pi, U]$. More precisely, the relevant quantity which controls $P_{\rm acc}$ is the variance of δH, whose minimization is a good criterion to improve the integrators. The numerical evidences reported in Ref. [87] show that the splitting of the determinant, as in eq. (3.9), gives a tremendous reduction of this variance and consequently, to target the same acceptance rate, higher step-sizes can be used, thus reducing the cost of the simulation.

3.2 Autocorrelations

Markov chains are generated through a transition matrix T. Hence, we expect to see a correlation length in the Monte Carlo time τ, called *autocorrelation time*, which reduces the amount of statistical independence in the chain, thus affecting the error of the observables.

Assume to have run the algorithm for N iterations. The set of field configurations $\phi^1 \to \phi^2 \to \dots \phi^N$ is a representative ensemble of field space. Given a set of primary observables a^α, the average of their measurements, evaluated configuration by configuration and denoted by a_i^α, is a stochastic estimator of the path integral expectation values $A^\alpha = \langle a^\alpha \rangle$

$$\bar{a}^\alpha = \frac{1}{N}\sum_{i=1}^{N} a_i^\alpha \,, \quad \delta a_i^\alpha = a_i^\alpha - A^\alpha \,. \tag{3.10}$$

Repeating the simulation many times with the same N and computing the average over the various repetitions, called *replica*, eventually will bring us to the true mean $\langle\langle a^\alpha \rangle\rangle = A^\alpha$. However in real world only a finite number of (finite) replica is available and the following variance statistically defines the error of our estimators

$$\langle\langle (\bar{a}^\alpha - A^\alpha)^2 \rangle\rangle = \frac{1}{N^2}\sum_{i,j}^{N} \langle\langle \delta a_i^\alpha \delta a_j^\alpha \rangle\rangle = \frac{1}{N^2}\sum_{i=1}^{N}\sum_{t=1-i}^{N-i} \langle\langle \delta a_i^\alpha \delta a_{i+t}^\alpha \rangle\rangle \,. \tag{3.11}$$

Expanding the sum over i and counting the number of $\langle\langle \delta a_i^\alpha \delta a_{i+t}^\alpha \rangle\rangle$ for a fixed t, which are all equivalent thanks to translation invariance in Monte Carlo time, we obtain

$$\langle\langle (\bar{a}^\alpha - A^\alpha)^2 \rangle\rangle = \frac{1}{N^2}\sum_{t=-(N-1)}^{N-1} (N - |t|)\Gamma_\alpha(t) \,, \quad \Gamma_\alpha(t) = \langle\langle \delta a_0^\alpha \delta a_t^\alpha \rangle\rangle \,, \tag{3.12}$$

where Γ_α is the *autocorrelation function* [90]. In the limit of large N the error of our estimator of A^α is

$$\sigma_\alpha^2 = \frac{1}{N}\sum_{t=-\infty}^{\infty} \Gamma_\alpha(t)(1 + O(1/N)) \approx \frac{\Gamma_\alpha(0)}{N} 2\tau_{\rm int}(A^\alpha) \,, \tag{3.13}$$

where we have introduced the normalized autocorrelation function and the *integrated autocorrelation time*

$$\rho(t) = \frac{\Gamma_\alpha(t)}{\Gamma_\alpha(0)}\,, \quad \tau_{\rm int}(A^\alpha) = \frac{1}{2} + \sum_{t=1}^{\infty} \rho(t)\,. \tag{3.14}$$

Note that $\Gamma_\alpha(0)$ corresponds to the standard variance.

At the practical level only a biased estimator of Γ is computable, since A^α are replaced with the measured $\bar{a}^\alpha$, and its definition in eq. (3.12) can be further generalized to the case of more observables [91]

$$\Gamma_{\alpha\beta}(t) = \frac{1}{N-t} \sum_{i=1}^{N-t} (a_i^\alpha - \bar{a}^\alpha)(a_{i+t}^\beta - \bar{a}^\beta) + O(1/N)\,. \tag{3.15}$$

Consequently also ρ and $\tau_{\rm int}$ are biased. Moreover, for the latter a finite summation window W is needed to truncate the sum in eq. (3.14) as otherwise its variance would be infinite[3].

With an analogous calculation it is possible to show that for a derived observable $F(A^\alpha)$ the error can be obtained according to eq. (3.13), with $\tau_{\rm int}(F)$ computed from the following autocorrelation function

$$\Gamma_F(t) = \left.\frac{\partial F(x)}{\partial x^\alpha}\right|_{x^\alpha=\bar{a}^\alpha} \Gamma_{\alpha\beta}(t) \left.\frac{\partial F(x)}{\partial x^\beta}\right|_{x^\beta=\bar{a}^\beta}\,, \tag{3.16}$$

calculated through the Taylor expansion of the estimator $\bar{F} = F(A^\alpha)$.

To better understand the behavior of autocorrelations in simulations it turns out to be very useful to interpret τ as an additional dimension to the 4D theory. In this framework it has been shown, in the free theory, that the autocorrelations for the HMC remain constant once the Monte Carlo time and the trajectory length are rescaled with the lattice spacing [92]. This statement does not hold anymore in the presence of interactions, due to the non-renormalizability of this algorithm [93]. In Ref. [93] it is argued that the HMC may fall in the same universality class of the Langevin algorithm[4], pointing to a scaling of autocorrelation times with a^{-2}.

In the 5D theory, functions like Γ can be interpreted as two-point correlators and the transition matrix $T(\phi' \leftarrow \phi)$ as a kind of Transfer Matrix in the lattice theory. Very

[3] A large amount of noise would be added to small portions of signal, indeed, according to Ref. [90] $(\delta\tau_{\rm int})^2 \approx (4W+2)\tau_{\rm int}^2/N$ would be larger than 100% for $W = N$.

[4] In the 5D picture the Langevin equation is renormalizable [94], if the underlying theory is, and therefore an asymptotic scaling with a is predictable. In particular the algorithms based on the Langevin equation, such as stochastic molecular dynamics (SMD), should exhibit the same scaling. The latter automatically extends to the HMC algorithm, which belongs to a subgroup of the SMD ones [95].

similarly to eq. (2.44) the Γ function can be expanded in a sum of exponential terms, by applying $T(\phi' \leftarrow \phi)$ between[5] δa_i^α and δa_{i+t}^α

$$\begin{aligned} \Gamma_\alpha(t) &= \sum_n e^{-t/\tau_n} s_n c_n^2(A^\alpha)\,, \quad s_n = \pm 1\,, \\ \text{with} \quad \tau_n &= \frac{1}{\log \lambda_n}\,, \quad T(\phi' \leftarrow \phi)|\lambda_n\rangle = \lambda_n|\lambda_n\rangle\,. \end{aligned} \tag{3.17}$$

While the modes τ_n are uniquely determined by the algorithm, the coupling to the modes depends on the observables. In general all the errors will be affected by the slowest mode, called *exponential autocorrelation time* $\tau_{\rm exp}$, and a reliable ensemble must have a statistics of $O(50)\times\tau_{\rm exp}$. The knowledge of $\tau_{\rm exp}$ however comes a posteriori, by running a simulation and computing the autocorrelations of some observables. Assuming that we have such a knowledge, the error analysis can consequently be adjusted [6]

$$\tau_{\rm int} = \left[\frac{1}{2} + \sum_{t=1}^{W} \rho(t)\right] + \tau_{\rm exp}\rho(W) \tag{3.18}$$

and in the following Chapters, where results are presented, eq. (3.18) will be always used.

3.2.1 Critical slowing down and topological modes

On top of the (unavoidable) scaling with the number of points in a fixed volume, namely a^{-4}, the cost of the simulation is further increased by the loss of performance of the algorithm in the limit $a \to 0$. This phenomenon is called *critical slowing down* and it goes along with the scaling of autocorrelations with the lattice spacing. It is typical in systems approaching a critical point and the question is only how severe it is.

The high-statistics study of Ref. [6] in the pure gauge theory demonstrates that topological modes strongly couple to $\tau_{\rm exp}$ and their scaling with the lattice spacing a^{-z} is more dramatic than expected, with $z \approx 5$ in the range $a \in [0.14\,, 0.05]$ fm. Beyond this range of probed lattice spacings, it is not excluded that the scaling may be even worse than a power law. Indeed, in Ref. [96] it is found to be exponential for CP^N models, which share many properties with QCD. It is plausible that the cause of the freezing of topology resides in the physics of the underlying classical gauge theory.

3.2.2 Topological sectors

In the classical Yang-Mills theory the space of gauge fields (in infinite space-time or on a 4D Torus) is divided in topological sectors. They are disconnected and separated by barriers of infinite action.

[5] The Frobenius-Perron theorem ensures that $\lambda_0 = 1$ and $|\lambda_n| < 1$ with $n \geq 1$. Detailed balance has been used to symmetrize $T(\phi' \leftarrow \phi)$ and produce its spectral decomposition.

At the end of Chapter 2 we have discussed how topology is realized at finite lattice spacing once an appropriate definition of smoothness, such as the Wilson flow, is provided. In Ref. [8] it has been demonstrated (numerically) that the probability of occurrence of fields that are between the sectors, defined in eq. (2.58), scales with a^6 in a fixed volume. This scaling is represented in Figure 3.1: the left panel is the result from the pure gauge simulations in Ref. [8], whereas the right one represents the same scaling in the presence of two dynamical fermions [9]. What we learn from these plots is that (repeating Section 2.6.1) sectors appear dynamically towards the continuum limit, where they are disconnected, and the regions "between the sectors" disappear with a high power of a.

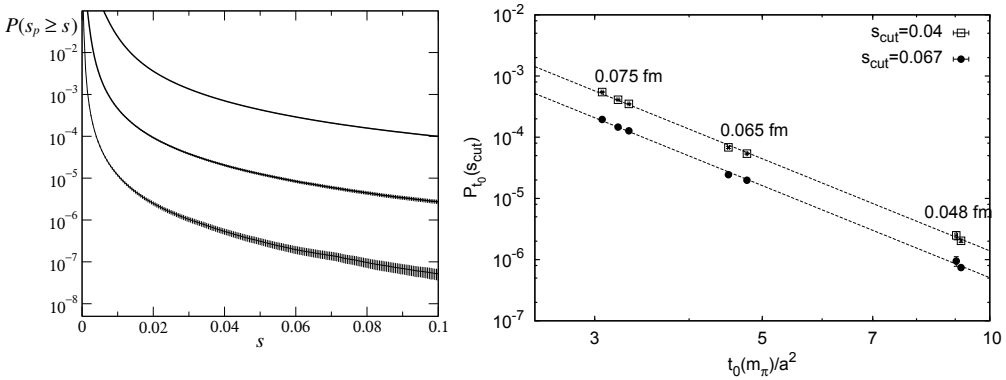

Figure 3.1: Both plots show the probability P_t, defined in eq. (2.58), that a smooth plaquette is bigger than a certain value s (left panel) or s_{cut} (right panel). This probability is measured on configurations of smooth fields V_t, with flow time $t = t_0$, and it is found to scale as a^{10} both with and without fermion fields in the sea. *Left:* numerical results in the pure gauge theory. The three curves represent from top to bottom lattices with $a \approx 0.099\,, 0.071\,, 0.05\,\text{fm}$ and the figure is taken from Ref. [8]. *Right:* a^2 scaling of the probability that a smooth plaquette s_p is larger than s_{cut}. The data points [9] correspond to ensembles with two dynamical fermions, at different lattice spacings and pion masses, as can be noticed from the displacement of the points along the x-axis.

If we now combine the notion of topology of gauge fields and the HMC algorithm, which we use to evaluate the path integral of QCD, we immediately notice that there is a problem: for the HMC algorithm, which is essentially a continuous transformation of the fields on the surfaces with constant Hamiltonian, towards $a \to 0$ changing sector becomes harder and harder and if a is too small, practically impossible. The consequence of this phenomenon is the freezing of topology and a scaling of autocorrelations much worse than the expected a^{-2} behavior. The fact that at coarse lattice spacings the charge decorrelates faster seems to be dominantly a cutoff effect.

Fermions, at fixed lattice spacing, are expected to help due to the suppression of topology given by the fermion determinant, since with a narrower distribution of the charge less tunneling events are needed. In Ref. [9] the suppression of topology has been demon-

strated for $O(a)$-improved Wilson fermions with per-cent accuracy w.r.t. the topological susceptibility in the Yang-Mills theory. However in terms of scaling behavior, the fermions at most reduce the coefficient in front of a^{-z}, not z. In the right panel of Figure 3.2 we compare the autocorrelation times[6] of Q^2 in the presence of two sea degenerate quarks [9] (for two values of the quark masses) against the pure gauge study in Ref. [6]. The gauge action is the Wilson plaquette action in both cases and the $\tau_{\rm int}$ shown have been corrected for the differences among the algorithms used[7]. The two lines have the same slope but different intercepts, which may be explained by the presence of the fermion determinant in the simulations.

In addition to that, Ref. [9] demonstrates that $a \approx 0.05\,\text{fm}$ is the crossing point where the topological charge is as slow as the smoothed energy density, whose scaling index $z \approx 2$ matches expectations. Eventually, for a better control over systematic effects in the continuum limit, simulations below 0.05 fm must be carried out and a solution to the problem of topology freezing must be found.

3.3 Open boundary conditions

In Appendix A we only briefly review the explanation of the emergence of non-trivial gauge transformations belonging to different homotopy classes. Their origin is in the topology of space-time, which is usually a 4D Torus. The solution proposed in Ref. [10] is to change it to a cylinder of length T by imposing boundary conditions at $x_0 = 0$ and T. The remaining three directions are compactified as usual on a 3D Torus.

To preserve gauge symmetry at the boundaries it suffices to fix the tangential components of the field strength tensor

$$F_{0\nu}(0,\vec{x}) = F_{0\nu}(T,\vec{x}) = 0\,. \tag{3.19}$$

The disappearance of homotopy classes guarantees that the space of fields is now connected and it breaks the quantization of the topological charge into integers.

Fermions can be added with suitable boundary conditions: similarly to the Schrödinger functional only half degrees of freedom must be fixed at $x_0 = 0, T$ and in practice the only allowed choice[8] [24, 97] is

$$\begin{gathered} P_+\psi|_{x_0=0} = P_-\psi|_{x_0=T} = 0\,, \quad P_\pm = \frac{1}{2}(1 \pm \gamma_0) \\ \overline{\psi}P_-|_{x_0=0} = \overline{\psi}P_+|_{x_0=T} = 0\,. \end{gathered} \tag{3.20}$$

[6] The topological charge is measured from smoothed links using the Wilson flow introduced in Chapter 2. The autocorrelation times reported in the next Figures correspond to Q^2 measured at flow time $t = t_0$, where $\tau_{\rm int}$ does not depend anymore on t[10, 9].

[7] To account for inactive links in the DD-HMC algorithm, the autocorrelations are corrected with the ratio of active links and multiplied with the acceptance rates. We do not expect the remaining details of the algorithms to contribute to this level of accuracy.

[8] To preserve parity and time reflection.

The renormalizability of the theory is still intact since no gauge-invariant dimension-3 operators can mix with the operators on the boundary surfaces [26]. The lattice discretization is practically the same[9] as with the periodic boundary conditions with two exceptions: the spatial plaquettes on the time slices 0 and T have weight $\frac{1}{2}$ and the spinors on those time slices are simply set to zero.

Hence, a Hilbert space of physical states can be constructed with the usual positive definite Transfer Matrix (see Chapter 2). The real difference with the periodic lattice is the presence of a boundary state Ω in the spectral representation of the partition function, which shares the same quantum numbers of the vacuum. We will extensively discuss its effects in the next Chapters where the extraction of spectral quantities from two-point correlation functions is described.

Similarly to the Schrödinger functional setup, also in the case of open boundaries irrelevant operators can be added to the action to accelerate the convergence to the continuum limit. The bulk action is improved as usual with the clover-term described in Chapter 2 and the boundaries through counter-terms of dimension four integrated over the points in the time slices at $x_0 = 0, T$. The only possible choices are $\partial_0\overline{\psi}\psi$ and the gluon energy density $\mathrm{tr}\{1-U\}$, which are multiplied by coefficients of the form $(c_{G,F}-1)$. At present they are known only to tree level $c_{G,F} = 1 + O(g_0^2)$ leaving room for $O(ag_0^2)$ effects (in particular where boundary effects are noticeable).

3.3.1 Scaling of autocorrelations

The absence of topological barriers should wash out the exceptional critical slowing down of the HMC, thus leaving space to the expected scaling of autocorrelations with a^{-2}.

In the left panel of Figure 3.2 we show the autocorrelation times measured with the HMC algorithm with open [10] and periodic [6] boundary conditions. The effect of the open boundaries on the scaling behavior is evident from the differences in the slopes. In the range of lattice spacing probed, which is approximately from 0.14 to 0.05 fm, the open boundaries cure the exceptional scaling of autocorrelations and restore it to a^{-2}.

[9] The γ_5-hermiticity of the Wilson operator is preserved.

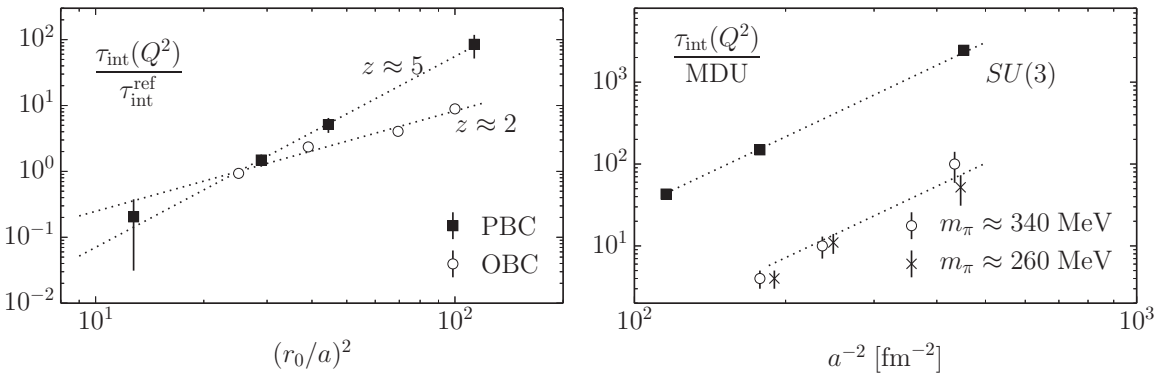

Figure 3.2: *Left*: scaling of the autocorrelations of Q^2 with Periodic [6] and Open BC [10]. In both cases the topological charge is summed over the entire volume. To better visualize the two different scalings of $\tau_{\rm int}$ we have considered the ratio w.r.t. $\tau_{\rm int}$ interpolated at $r_0/a = 5$. *Right*: comparison of $\tau_{\rm int}(Q^2)$ with [9] and without [6] dynamical fermions ($N_{\rm f} = 2$), with Periodic BC. The z factors are identical and close to 5, as depicted by the two lines which have the same slope. The effect of the suppression of topology by the fermions is evident.

4 CLS Ensembles

In the first three Chapters we have introduced the lattice regularization of QCD, together with its renormalization properties, and the algorithms that are currently used to simulate it. Hence in this Chapter we proceed to the description of the ensembles, whose analysis is the final goal of the thesis and will be presented in Chapter 6.

Nowadays large-volume simulations with dynamical quarks can be carried out almost exclusively by the joint effort of various groups, often organized in a collaboration. In our case we took part to the Coordinated Lattice Simulations[1] (CLS) effort in the production of the ensembles, generated on High Performance Computers (HPC). In the following we will describe only the crucial algorithmic and physics parameters, which will be relevant for the discussion of the analysis, whereas the interested reader can find all the details on the simulations in Ref. [12].

In Chapter 3 the importance of topology freezing in modern simulations at small lattice spacings has been stressed. To overcome it, the pioneering simulations carried out by the CLS effort adopt open boundary conditions in time together with Twisted-Mass (TM) reweighting, for the first time on a large-scale project. The boundary effects will be discussed in the next Chapter, while now we introduce the TM reweighting.

4.1 Twisted-mass reweighting

The transformation $m_0 \to m_0 + i\mu\gamma_5$ is applied to the Dirac operator corresponding to the pair of degenerate light quarks. The twisted mass μ acts as an infrared regulator to stabilize simulations at small quark masses. If $\mu > 0$ those gauge-field configurations with almost-singular Dirac operator, being "infrared safe" due to the TM term, are also accessible to the algorithm, as their Boltzman weight factor is no more zero. Therefore, the twisted mass adopted in our simulations, the so-called type II introduced in Ref. [98],

$$S_f(\mu) = -\log\det\frac{(\hat{Q}^2+\mu^2)^2}{\hat{Q}^2+2\mu^2} - \log\det Q_{oo}^2\,, \tag{4.1}$$

is a lever arm also to assure the ergodicity of the HMC. The factorization of the fermion determinant appearing in eq. (4.1) is related to the use, in our setup, of the even-odd

[1] https://wiki-zeuthen.desy.de/CLS

preconditioning

$$\det Q^2 = \det Q_{oo}^2 \det \hat{Q}^2 \,, \quad \hat{Q} = Q_{ee} - Q_{eo} Q_{oo}^{-1} Q_{oe} \,, \tag{4.2}$$

with the TM term applied only to $\hat{Q}$. Clearly to recover results in the underlying theory, at $\mu = 0$, the configurations must be-reweighted [99]

$$\langle O \rangle = \frac{\langle WO \rangle_W}{\langle W \rangle_W} \,, \quad \langle O \rangle_W = \frac{\int [\mathcal{D}U] e^{-S(\mu)} O}{\int [\mathcal{D}U] e^{-S(\mu)}} \,. \tag{4.3}$$

We indicate with $S(\mu)$ the full action (including the gluonic part and Symanzik counterterms) which depends on $S_f(\mu)$ (from which S inherits the μ depedence). Hence from eq. (4.1) the functional form of the TM *reweighting factor* is

$$W = \det \frac{\hat{Q}^2(\hat{Q}^2 + 2\mu^2)}{(\hat{Q}^2 + \mu^2)^2} \,, \tag{4.4}$$

The reason behind the choice of eq. (4.1) and eq. (4.4) in favor of the more simplistic case

$$\bar{W} = \det \frac{\hat{Q}^2}{\hat{Q}^2 + \mu^2} \,, \tag{4.5}$$

lies in the behavior of their fluctuations in the ultra-violet region. Assuming that the spectrum of $\hat{Q}$ is dominated by a single eigenvalue $\hat{Q}|\lambda\rangle = \lambda|\lambda\rangle$, in the limit $\mu/\lambda \ll 1$ eq. (4.4) and eq. (4.5) scale differently

$$\bar{W} = 1 - \frac{\mu^2}{\lambda^2} + O(\lambda^{-4}) \,, \quad W = 1 - \frac{\mu^4}{\lambda^4} + O(\lambda^{-6}) \,. \tag{4.6}$$

Since the number of high modes scales with the volume, their effective contribution to the fluctuations of the reweighting factor is more suppressed for eq. (4.4) than eq. (4.5). For this reason W has been chosen in our large-volume simulations.

4.1.1 Fluctuations of the low modes

Exploring more phase space, thanks to a positive μ, is certainly desirable, but can have disadvantages too. In fact a large value of the twisted mass increases, in the Monte Carlo histories, the presence of the so-called *exceptional* configurations, with almost-zero eigenvalues of the Dirac operator. The reweighting factor in eq. (4.4) is computed stochastically using $N_{\rm src}$ gaussian random fields (which we will often call also noise sources)

$$\tilde{W}(\mu, N_{\rm src}) = \frac{1}{N_{\rm src}} \sum_{i=1}^{N_{\rm src}} \exp \left[- \eta_i^\dagger \left(\frac{(\hat{Q}^2 + \mu)^2}{\hat{Q}^2(\hat{Q}^2 + 2\mu^2)} - 1 \right) \eta_i \right] , \tag{4.7}$$

and for these exceptional configurations problems might occur. Through the stochastic estimators, the path integral is enlarged, pretty much as with the pseudo-fermions and only after the average over the noise fields the determinant is reproduced (we consider below the case $N_{\rm src} = 1$)

$$W = \langle \tilde{W}(\mu, 1) \rangle_\eta = \frac{\int [\mathcal{D}\eta] \tilde{W}(\mu, 1) e^{-\eta^\dagger \eta}}{\int [\mathcal{D}\eta] e^{-\eta^\dagger \eta}} \,. \tag{4.8}$$

Since the integrals over the noise fields and the integral over the gauge field can always be exchanged, the same estimator of the reweighting factor must be used for all configurations, which means fixing $N_{\rm src}$ for each ensemble.

For a generic positive definite operator A, the variance of the stochastic estimator of $\det A$, define by

$$\det A = \langle \tilde{A} \rangle_\eta \,, \quad \tilde{A} = e^{-\eta^\dagger (A^{-1} - 1)\eta} \,, \tag{4.9}$$

can easily be obtained with a few lines of algebra

$$\mathrm{var}(\tilde{A}) = \langle \tilde{A}^2 \rangle_\eta - \langle \tilde{A} \rangle_\eta^2 = \det \frac{A}{2 - A} - (\det A)^2 \,. \tag{4.10}$$

In our application A is replaced by the argument of the determinant in eq. (4.4).

As originally suggested in Ref. [100], a factorization à la Hasenbush of eq. (4.4) improves the estimate of the reweighting factor. Inserting intermediate twisted masses μ_i reduces the fluctuations of the various contributions which can be estimated with less sources, thus keeping the effort almost constant. Hence, improvement can be achieved by a proper tuning of the masses. If the following factorization is employed

$$W_H = \prod_{i=1}^{N} \det \frac{(\hat{Q}^2 + \mu_i^2)^2 (\hat{Q}^2 + 2\mu_{i+1}^2)}{(\hat{Q}^2 + 2\mu_i^2)(\hat{Q}^2 + \mu_{i+1}^2)^2} \equiv \prod_{i=1}^{N} f(\hat{Q}, \mu_i, \mu_{i+1}) \,, \quad \mu_i < \mu_{i+1} \,, \tag{4.11}$$

according to eq. (4.10), the variance of its stochastic estimator is

$$\mathrm{var}(W_H) = \frac{W_H}{\prod_i (2 - f(\hat{Q}, \mu_i, \mu_{i+1}))} - W_H^2 \,. \tag{4.12}$$

If $\mu_0 = 0$ and $\mu_N = \mu$ the definition of W in eq. (4.4) is recovered. The minimization of this variance w.r.t. μ_i leads to the condition $f(\hat{Q}, \mu_i, \mu_{i+1}) = f(\hat{Q}, \mu_{i-1}, \mu_i)$, which provides a recipe to obtain optimal values of the twisted intermediate masses.

We tested this idea on some exceptional configurations of the ensemble H105. In particular assuming $\hat{Q}$ to be dominated by a single eigenvalue λ, in the limit $\lambda \to 0$ we impose the condition

$$\frac{\mu_i^2}{\mu_{i+1}^2} = \frac{1}{c} \,, \quad \mu_0 = 0 \,, \quad \mu_N = \mu \,, \tag{4.13}$$

where, for convenience, we introduce the factor c. In the right panel of Figure 4.1 we plot the results of the various determinants f in eq. (4.11), where the intermediate masses μ_i have been chosen with $c = 2$ and $N = 10$. Each determinant has been computed stochastically with 15 realizations of the noise fields, leading to a final precision of W_H around 20/30%. Without the factorization and 24 stochastic sources, the reweighting factor W was completely unknown, as can be seen from the left panel of Figure 4.1, where we plot the error of $\tilde{W}$ as a function of its mean value.

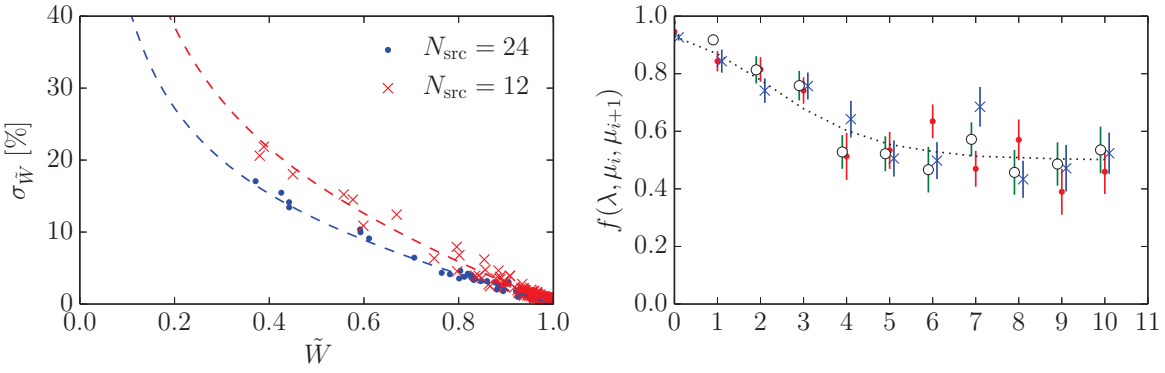

Figure 4.1: *Left*: measurements of the TM reweighting factor on the ensemble H105. The curves represent the prediction for the variance in eq. (4.10), which describes reasonably well both sets of data. For this ensemble the chosen value of μ is such that 1% of the configurations have $\tilde{W} < 0.9$. *Right*: results of the stochastic estimates of the determinants in eq. (4.11) whose set of μ_i has been obtained according to $\mu_{i+1} = \sqrt{2}\mu_i$. The line connects the predicted points $f(\hat{Q}, \mu_i, \mu_{i+1})$, where $\hat{Q}$ has been replaced with a single eigenvalue λ, approximately estimated from a separate computation.

When $\tilde{W}$ approaches 1 the variance goes to zero and a good estimate can be obtained with fewer sources. However, we see that when $\tilde{W} \lesssim 0.5$ the relative error of the reweighting factor is above 10% and for some configurations with $\tilde{W} \sim 0$ it is 100%. From the plot it is clear that $N_{\rm src}$ should be increased by at least a factor 2 or 3 to keep the error below the 10% threshold. With $N_{\rm src}$ also the cost grows and the right balance must be found, taking into account that these (problematic) configurations are only a small part of the total statistics, about 1% for the test case showed in Figure 4.1. For those configurations, we have estimated the reweighting factor through the factorization of the determinant, which proved to be better in this situation. Thanks to this knowledge, we could safely conclude that they are not relevant in the final estimates of the reweighted observables, given the accuracy that we are able to reach at present. For this reason, in the reweighting procedure we always compute the TM reweighting factor W according to eq. (4.7).

4.2 RHMC

To simulate the strange quark field we use the Rational Hybrid Monte Carlo (RHMC) algorithm [101, 102]. We adopt Zolotarev's approximation to compute the square root, which, similarly to the TM term, is applied only to $\hat{Q}$

$$\det Q = \det Q_{oo} \det \sqrt{\hat{Q}^2} = \det Q_{oo} \frac{P_1(\hat{Q}^2, n)}{P_2(\hat{Q}^2, n)} W_1 \,. \tag{4.14}$$

Note that the square root requires $\hat{Q}^2$ to be positive definite. P_1 and P_2 are two polynomials of degree n, whose coefficients are computed to optimally approximate the square root in the range $[r_a\,, r_b]$. W_1 is a reweighting factor which is later computed to account for the inaccuracies introduced by the approximation through the ratio of the polynomials.

In our simulations such inaccuracies are negligible [12], since we have chosen large values of n and spectral ranges $[r_a\,, r_b]$ wide enough to contain the full spectrum of $\hat{Q}$ (note that here the lower bound of the spectral gap is controlled by the strange quark mass). This is reflected in the fluctuations of the RHMC reweighting factor (compared to the TM reweighting factor, the variance is $O(100)$ times smaller) which in practice amount to a tiny increase in the error of the reweighted observables.

4.3 Ensembles

Let us now discuss the choice of the physical parameters: β and the two values of κ. Simulations at small up/down quark masses became feasible, in the last decade, thanks to the algorithmic and computer developments. However, physical (but always degenerate) light quark masses can be simulated at relatively coarse lattice spacings and they are still very expensive, in terms of cpu resources. Therefore, the generation of ensembles is usually spread over a wide range of masses in order to extrapolate physical quantities to the desired point. In Table 4.2 we report the list of the ensembles used in this thesis, with the relevant physical parameters and the statistics in MDU.

For a fixed value of the lattice spacing and in the three-flavor theory, finding a trajectory in the up/down vs. strange quark mass plane leading to the physical point is not trivial, since many possibilities are in principle available. In the left panel of Figure 4.2, a few of the most reasonable ones are plotted. As already said, these trajectories must be taken at fixed lattice spacing, which is in one-to-one correspondence with $\tilde{g}_0$ (recall the discussion on $O(a)$-improvement with Wilson fermions in Chapter 2). Therefore the chiral trajectory defined by keeping the sum of the bare quark masses constant [103], has the obvious advantage

$$\mathrm{tr}M = const \quad \rightarrow \quad \tilde{g}_0 = const \times g_0 \,. \tag{4.15}$$

The symmetric point, where all quarks are degenerate, defines the first point of the trajectory. However, using the renormalized $\mathrm{tr}M$ to fix the trajectory is not ideal, since

β	3.4	3.46	3.55	3.7
$\tau_{\rm exp}$	40(12)	58(18)	80(24)	108(44)

Table 4.1: Values of the exponential autocorrelation times extracted from the ensembles with $m_\pi = m_{\rm K} \approx 420\,{\rm MeV}$. No significant dependence on the quark masses has been found, given the accuracy of our estimates of $\tau_{\rm exp}$.

scale-dependent renormalization factors and $O(a)$-improvement coefficients are needed. Moreover the physical value that $\mathrm{tr}M_{\rm R}$ should target is not known a priori, but it would be rather the goal of a computation, as it means directly evaluating the quark masses. To circumvent these issues, we turn to the following two observables

$$\phi_2 = 8t_0 m_\pi^2\,, \quad \phi_4 = 8t_0(m_{\rm K}^2 + \frac{1}{2}m_\pi^2)\,, \tag{4.16}$$

whose leading order expansion in Chiral Perturbation Theory (see next Chapter) are linear in $1/\kappa_u$ and $\mathrm{tr}M$. With 2+1 flavors, their values at physical quark masses in the continuum limit

$$\phi_2^{\rm phys} = 0.0801(27)\,, \quad \phi_4^{\rm phys} = 1.117(38)\,, \tag{4.17}$$

are a combination of t_0 taken from Ref. [75] and the pion and kaon masses, where QED and isospin breaking effects have been removed [104]

$$m_\pi^{\rm phys} = 134.8(3)\,{\rm MeV}\,, \quad m_{\rm K}^{\rm phys} = 494.2(4)\,{\rm MeV}\,, \quad \sqrt{8t_0} = 0.4144(70)\,{\rm fm}\,. \tag{4.18}$$

For each value of β, at the symmetric point κ_u has been tuned to match $\phi_4 = 1.15$ with per-cent accuracy, as shown in Figure 4.3. The effects of possible mistunings of ϕ_4 on other observables (e.g. mesonic decay constants) will be discussed in the next Chapter. t_0 is used as an intermediate scale, since its computational effort is negligible compared to the production of configurations. The disadvantage introduced by this choice is the size of cutoff effects between different discretizations of the energy density. Here and in the following, we will always use the clover discretization of $G_{\mu\nu}$, which exhibits a smaller dependence on a^2, due to the particular combination with the Lüscher-Weisz action of the bulk and the Wilson action in eq. (2.55) [105]. These effects could be reduced by replacing t_0 with t_1, which is expected to have smaller discretization errors.

To see whether we have achieved a proper sampling of the field space, the statistics has to be compared with the exponential autocorrelation time. Our ensembles have been generated with a number of Molecular Dynamics Units (MDU) of $O(50) \times \tau_{\rm exp}$ and larger, thus giving a reliable estimate of the autocorrelations plotted in Figure 4.2 (right panel). From the energy density at positive flow time we have extracted $\tau_{\rm exp}$ for the four lattice spacings, whose values are listed in Table 4.3.

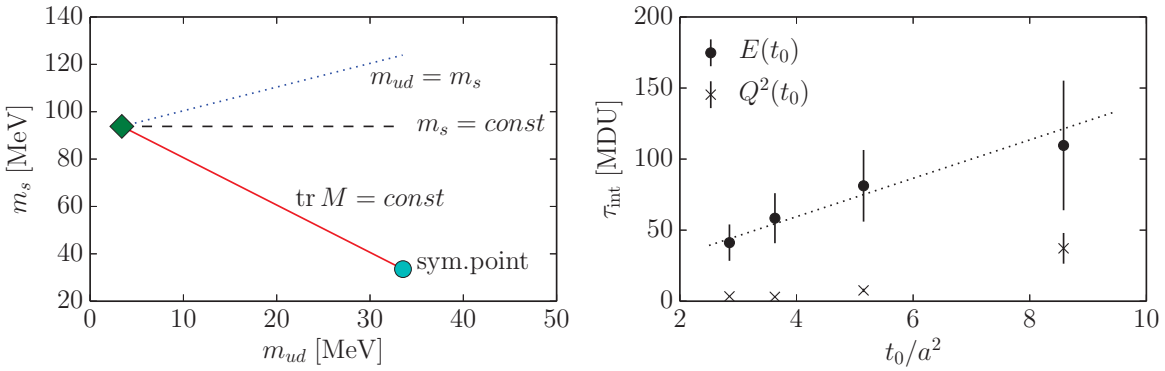

Figure 4.2: *Left*: different chiral trajectories in the bi-dimensional parameter space spanned by the two quark masses. The green diamond is the physical point where $m_s \approx 93.8\,\text{MeV}$ and $m_{ud} \approx 3.4\,\text{MeV}$ [104]. *Right*: scaling of the autocorrelations for the energy density (clover-definition) and the topological charge squared, measured at flow time $t = t_0$ from the ensembles H101, H400, H200, N301.

In accordance with the findings of Ref. [9] the smoothed energy density $E(t)$ shows the largest autocorrelation times, with the expected scaling a^{-2}. The $\tau_{\rm int}$ of the topological charge squared is smaller throughout but seems to increase quickly for $t_0/a^2 > 6$. A possible explanation for the topological charge not being yet the slowest observable, might be given by the suppression of topology by the fermion determinant, discussed in Chapter 3.

The volumes of our ensembles have been chosen to fulfill the condition $m_\pi L \geq 4$ (except two cases with $m_\pi L \simeq 3.8$). Finite-volume effects have been analytically studied in the interacting scalar theory in Ref. [106], whose conclusion is that for a theory with a mass gap, they are expected to fall off exponentially. In QCD the exponent is given by the familiar combination $m_\pi L$ and our conservative choice leads to finite-volume corrections proportional to $e^{-4} = 0.018$. The coefficient in front of the exponential factor depends on the observable and in some cases is very small. Nevertheless the level of accuracy reached by modern lattice computations requires to take these effects into account, for a reliable estimate of a quantity in the continuum limit. In this thesis we will address this problem in the next Chapter where we will study, for some ensembles, the finite-volume dependence of pseudo-scalar spectral quantities.

Finally, let us mention that a third advantage of the choice in eq. (4.15) is that the tuning can be done in relatively small volumes, since at the symmetric point pions are heavy enough to guarantee that lattices with $L/a = 32$ (and $L/a = 48$) satisfy $m_\pi L \simeq 4$ in our range of β. Once ϕ_4 is computed at the symmetric point the values of κ_u and κ_s can be changed according to eq. (4.15), along the red line in Figure 4.2.

As a first attempt to verify how much the renormalized tr$M$ is constant, we compute the observables in eq. (4.16) for each ensembles and plot them in the right panel of Figure 4.3. Lattice artifacts are not observed, except for the point corresponding to the ensemble J303, where also mistunings can play a role (see next Chapter).

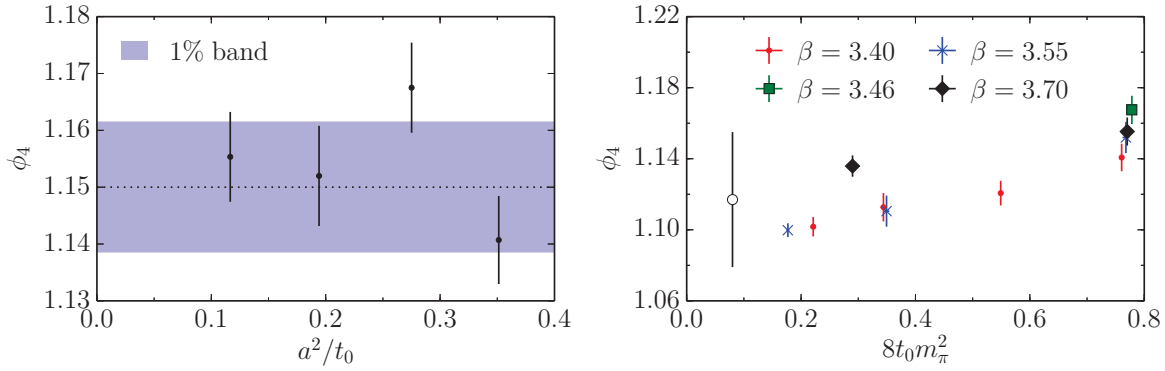

Figure 4.3: *Left*: tuning variable ϕ_4 at the symmetric point for our four lattice spacings. Given the statistical precision the tuning to $\phi_4 = 1.15$ has been achieved to 1% accuracy, represented by the blue band. *Right*: ensembles at fixed tr$M$ in the plane $\phi_4(\phi_2)$. The open symbol corresponds to the physical point, eq. (4.17). A dependence on the lattice spacing is not visible between the points at $\beta = 3.4$ and $\beta = 3.55$, while for the leftmost point at $\beta = 3.7$, namely J303, the situation is different. Note that, in these plots we want to show essentially how the observables used in the tuning of the ensembles look like. In the next Section, we will correct the points for finite-volume and mistuning effects and only after these corrections discuss their cutoff effects.

const.	id	β	L/a	T/a	κ_u	κ_s	MDU	m_π[MeV]	m_K[MeV]	$m_\pi L$
tr$M$	H101	3.40	32	96	0.13675962	0.13675962	8000	420	420	5.8
	U103	3.40	24	128	0.13675962	0.13675962	15000	420	420	4.3
	H102	3.40	32	96	0.136865	0.136549339	8100	350	440	4.9
	H105	3.40	32	96	0.136970	0.13634079	11600	280	460	3.9
	C101	3.40	48	96	0.137030	0.136222041	5400	220	470	4.7
m_s	H106	3.40	32	96	0.137015570...	0.136148704...	6000	270	510	3.8
	H107	3.40	32	96	0.136945665...	0.136203165...	6200	350	530	5.1
	C102	3.40	48	96	0.137050845...	0.136129062...	1200	220	500	4.7
$\kappa_u = \kappa_s$	H400	3.46	32	96	0.13688848	0.13688848	4200	420	420	5.2
	H401	3.46	32	96	0.136725	0.136725	4500	550	550	7.3
	H402	3.46	32	96	0.136855	0.136855	4600	450	450	5.7
tr$M$	H200	3.55	32	96	0.137000	0.137000	8000	420	420	4.4
	N200	3.55	48	128	0.137140	0.13672086	6800	280	460	4.4
	D200	3.55	64	128	0.137200	0.136601748	3600	200	480	4.2
tr$M$	N300	3.70	48	128	0.137000	0.137000	6100	420	420	5.1
	J303	3.70	64	192	0.137123	0.1367546608	2300	260	470	4.1

Table 4.2: List of the ensembles. The column "const." groups ensembles belonging to the same (chiral) trajectory, fixed by constant tr$M$ or m_s. Note the ensembles at $\beta = 3.46$ where the condition is the degeneracy of the quark masses. The column id lists the names of the various ensembles. The chosen naming convention relates the first capital letter to the geometry, the first digit to β and the final two digits to the particular combination of κ_u and κ_s. The statistics of the ensembles is reported in MDU. We give approximate values of m_π and m_K obtained in units of t_0 with $\sqrt{8t_0} = 0.4144$ fm. Finally, in the last column we list the product $m_\pi L$.

5 Computation of spectral quantities

In this Chapter we describe the methods used to compute pseudo-scalar meson masses and decay constants for the set of ensembles described in Chapter 4. Together with these fermionic quantities we also compute the "flow" observable t_0. Let us make here a remark on the notation used in the following: we denote with flavor indices 1,2 and 3, the up, down and strange quarks. In our setup the light quarks are degenerate, nevertheless we use the indices 1 and 2 to underline that we are interested only in non-singlet two-point functions. Note also that we often interchange the "flavor" with the "mesonic" notation: $12 \leftrightarrow \pi$ and $13 \leftrightarrow K$. Throughout this and the next Chapter we will often indicate quantities measured at the symmetric point with the superscript 'sym'.

5.1 Measurements of the observables

As we have mentioned in Chapter 1, the analysis is focused on two-point correlation functions between the pseudo-scalar and the zero-component of the axial fermion currents (introduced in Chapter 2, eq. (2.21)), which we average over the spatial volume, to project to zero-momentum

$$\begin{aligned} f_{\mathrm{A}}^{rs}(x_0, y_0) &= -\frac{a^6}{L^3} \sum_{\vec{x},\vec{y}} \langle A_0^{rs}(x_0, \vec{x}) P^{sr}(y_0, \vec{y}) \rangle \,, \\ f_{\mathrm{P}}^{rs}(x_0, y_0) &= -\frac{a^6}{L^3} \sum_{\vec{x},\vec{y}} \langle P^{rs}(x_0, \vec{x}) P^{sr}(y_0, \vec{y}) \rangle \,. \end{aligned} \tag{5.1}$$

Once Wick's contractions are performed, eqs. (5.1) amount to the evaluation of two propagators S, carrying flavors r and s (the trace is over color and spinor indices)

$$f_X(x_0, y_0) = -\frac{a^6}{L^3} \sum_{\vec{x},\vec{y}} \left\langle \mathrm{tr}\left[\Gamma_X S^r(x, y) \gamma_5 S^s(y, x)\right] \right\rangle , \quad X = A_0, P \,; \Gamma_X = \gamma_0\gamma_5, \gamma_5 \,. \tag{5.2}$$

Hence, the computation of f_{A} and f_{P} would require, in principle, $O(L^3)$ solutions of the Dirac equation, which would be too expensive. However, thanks to stochastic techniques, the cost of the measurements of eqs. (5.1) can be drastically reduced (for an introduction see for example Ref. [83] and references therein).

We start by adding a set of $N_{\rm src}$ fields η_i to the path integral, which do not affect the physics of the theory and fulfill the conditions (we drop color and spinor indices)

$$\langle \eta_i^\dagger(x)\eta_j(y)\rangle_\eta = \delta(x-y)\delta_{ij}\,, \quad \langle \eta_i(x)\rangle_\eta = 0\,, \tag{5.3}$$

where the definition of $\langle\cdots\rangle_\eta$ has been given in eq. (4.8), but in this case we use $U(1)$-distributed random sources. Let us start by solving the Dirac equations (again we do not write color and spinor indices)

$$D_{\rm W}(m_{0,f})\xi_i^f(y) = \eta_i(y) \quad \to \quad \xi_i^f(x) = \sum_y S^f(x,y)\eta_i(y)\,, \tag{5.4}$$

$$D_{\rm W}(m_{0,f})\gamma_5\zeta_i^f(y) = \gamma_5\Gamma_X^\dagger\eta_i(y) \quad \to \quad \zeta_i^f(x) = \sum_z S^{f\,\dagger}(x,z)\Gamma_X^\dagger\eta_i(z)\,. \tag{5.5}$$

Now, if we sum over the various noise fields the product

$$\mathcal{F}_X(x) = \frac{1}{N_{\rm src}}\sum_{i=1}^{N_{\rm src}}\Big(\big[\zeta_i^r(x)\big]^\dagger\gamma_5\xi_i^s(x)\Big)\,, \tag{5.6}$$

when the sources are integrated out we obtain the trace we are interested in (which can be later averaged over the gauge field configurations)

$$\langle\mathcal{F}_X(x)\rangle_\eta = \sum_y \mathrm{tr}\left[\Gamma_X S^r(x,y)\gamma_5 S^s(y,x)\right]. \tag{5.7}$$

In our case, we use stochastic sources distributed on one specific time-slice, a technique sometimes called time-dilution. At the same cost of $N_{\rm src}$ point-like sources, the variance of our observables is significantly reduced [107]. For these noise fields, eq. (5.7) returns $\langle\mathcal{F}(x,y_0)\rangle_\eta$, since the sum on the r.h.s. is performed only on the spatial $\vec{y}$. Also for this type of stochastic estimates, $N_{\rm src}$ must be kept constant for all gauge-field configurations, as $\int[\mathcal{D}U]$ and $\langle\cdots\rangle_\eta$ can be freely interchanged.

The stochastic estimates reported above have an error proportional to $1/\sqrt{N_{\rm src}}$ and the observables, as we have seen in Chapter 3, fluctuate with the gauge-field configurations. Therefore, $N_{\rm src}$ must be chosen reasonably large (balancing with the computational cost) to be able to neglect the first source of error in the analysis. In Figure 5.1 we show the dependence of the errors of two pseudo-scalar spectral quantities on the number of sources. From the plots we infer that for $N_{\rm src} \simeq 10$ the precision on the derived observables is dominated by the gauge noise. Anyhow, since the computation of $f_{\rm A}$ and $f_{\rm P}$ is particularly cheap (thanks to the solver used in the inversion of $D_{\rm W}$), we decided to use 16 stochastic sources for our ensembles at $\beta = 3.4$ and 3.55, and between 20 and 24 sources for the measurements at $\beta = 3.7$.

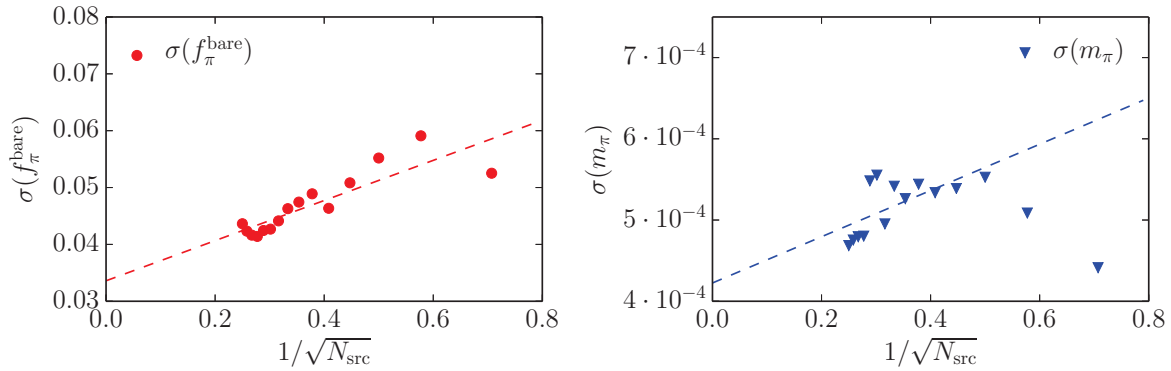

Figure 5.1: Error of the bare pion decay constant and mass as a function of the number of stochastic sources N_{src}. The test ensemble is D200 and the maximum value of N_{src} is 16. The lines represent linear fits to the points, excluding those with $N_{\text{src}} < 4$. In both cases the limit $N_{\text{src}} \to \infty$ gives an estimate of the (pure) gauge noise, coming from the fluctuations of the pseudo-scalar correlation functions with the gauge-field configurations.

5.1.1 Spectral quantities with open BC

To understand and extract the spectral quantities from the correlation functions in eq. (5.1), we expand them using the Transfer Matrix $\hat{T} = e^{-\hat{H}}$, introduced in Chapter 2. Since the discussion below does not depend on the specific choice of flavor indices, we concentrate only on the pion sector, but everything is valid also for kaons.

Let us start from eq. (2.43) and from some considerations: the boundary states are the same on both sides for open BC (see eq. (3.19)) and we denote them with $|\Omega\rangle$. They are invariant under spatial translations, meaning that[1] $\langle\Omega|\vec{p}, n\rangle = 0$ for $\vec{p} \neq \vec{0}$. Recall also that we are interested in correlators projected to zero momentum, eq. (5.1). For these reasons we will omit the momenta $\vec{p}$ from the notation.

On top of this we modify two other properties, to keep the notation as simple as possible: we define $|\alpha, n\rangle$ the eigenstates of the Hamiltonian, with n labeling the energy levels and α the other quantum numbers of the states, and we use the normalization $\langle\beta, m|\alpha, n\rangle = \delta_{nm}\delta_{\alpha\beta}$. Since we are interested in pseudo-scalar two-point functions, the relevant combination of quantum numbers for their spectral representations is, apart from[2] $J^P = 0^-$, $C = +$ and isospin $(I, I_3) = (1, 1)$ (we consider always non-singlet flavor rotations, thus leading to the charged pions and kaons) and we use $\alpha = \pi$ as a shorthand.

[1] The notation is taken from Section 2.4.

[2] On the lattice the continuum rotation group is broken to a discrete subgroup. The irreducible representations of the latter classify lattice states, which can overlap with states with different J of the continuum theory. Usually lattice states are labelled with the smallest of such J, which is then recovered in the continuum limit, e.g. the irreducible representation A_1 with $J = 0$.

The following derivation (and notation) is taken from Ref. [108], where practically the same calculations have been carried out. We decided to repeat them here since many of these formulae will be used in the next Sections.

According to the new notation introduced above eq. (2.43), for $f_{\rm A}$ and $f_{\rm P}$, and in the limit of large T, reduces to

$$f_X(x_0,y_0) = \sum_{\alpha,\beta}\sum_{n,m} \frac{\langle\Omega|\beta,m\rangle}{\langle\Omega|0,0\rangle} e^{-\tilde{E}^{\beta}_m(T-x_0)} \langle\beta,m|\hat{X}|\alpha,n\rangle e^{-\tilde{E}^{\alpha}_n(x_0-y_0)} \langle\alpha,n|\phi_\pi(y_0)\rangle\,, \qquad (5.8)$$

with $X = A_0\,, P$ and $|\phi_\pi(y_0)\rangle$

$$|\phi_\pi(y_0)\rangle \equiv L^3 \sum_{\gamma,l} \hat{P}|\gamma,l\rangle e^{-y_0\tilde{E}^{\gamma}_l} \frac{\langle\gamma,l|\Omega\rangle}{\langle 0,0|\Omega\rangle}\,, \quad \langle\alpha,n|\phi_\pi(y_0)\rangle = \delta_{\alpha\pi}\langle\pi,n|\phi_\pi(y_0)\rangle\,. \qquad (5.9)$$

In order to investigate the effects of the boundaries, let us take the limit $|x_0-y_0|\to\infty$ such that the states propagating between $\hat{X}$ and $\phi_\pi(y_0)$ are washed out and only $|\pi,0\rangle$ survives. In this limit eq. (5.8) becomes ($m_\pi \equiv \tilde{E}^{\pi}_0$)

$$f_X(x_0,y_0) = \sum_m \left[\frac{\langle\Omega|0,m\rangle}{\langle\Omega|0,0\rangle} e^{-\tilde{E}^0_m(T-x_0)} \langle 0,m|\hat{X}|\pi,0\rangle\right] e^{-m_\pi(x_0-y_0)} \langle\pi,0|\phi_\pi(y_0)\rangle\,, \qquad (5.10)$$

since the boundary state has an overlap only with the states with $\alpha=0$. If the separation between x_0 and the boundary at $x_0=T$ is large enough, $(T-x_0)\tilde{E}^0_2 \gg 1$, the first relevant contribution from the boundary is given by the state with energy $\tilde{E}^0_1$

$$f_X(x_0,y_0) = \left[1 + \eta^T_X e^{-\tilde{E}^0_1(T-x_0)} + \ldots\right] \langle 0,0|\hat{X}|\pi,0\rangle e^{-m_\pi(x_0-y_0)} \langle\pi,0|\phi_\pi(y_0)\rangle\,, \qquad (5.11)$$

with the ellipsis corresponding to terms of order $e^{-\tilde{E}^0_2(T-x_0)}$ and the matrix element η^T_X related to the boundary at $x_0=T$ (and similarly for the case $x_0=0$, η^0_X)

$$\eta^T_X = \frac{\langle\Omega|0,1\rangle}{\langle\Omega|0,0\rangle} \frac{\langle 0,1|\hat{X}|\pi,0\rangle}{\langle 0,0|\hat{X}|\pi,0\rangle}\,. \qquad (5.12)$$

In the pure Yang-Mills theory we would certainly identify the state $|0,1\rangle$ with the scalar glueball 0^{++}. In QCD, however, also a two-pion state with zero momentum and zero isospin can be a possible candidate. At present, there are however still some gaps on the knowledge of the mass of the scalar glueball, both from the theoretical and the experimental side, and it is believed to be heavier than $2m^{\rm phys}_\pi$. Certainly, this statement might not hold for ensembles with pion masses larger than 500 MeV or so, which is never the case in our setup. Nevertheless, in the following analysis we make sure to keep this systematic uncertainty under control, as explained in the next Subsections.

Let us now look at the consequences of assuming that the excited state $\tilde{E}_1^0$, appearing in eq. (5.11), is a two-pion state. The quantization of momenta, given by the finiteness of the spatial directions, pushes the energies of states with momenta up in the spectrum, thus leaving, for instance, a separation of order $2\pi/L$ between two pions (both) with zero momentum and with opposite momenta. Hence, if we identify the state $|0,1\rangle$ with two pions, we expect $\tilde{E}_1^0 = 2m_\pi$ rather than $\tilde{E}_1^0 = 2\sqrt{m_\pi^2 + |\vec{p}|^2}$, with[3] $|\vec{p}| = 2\pi/L$.

Expecting $\tilde{E}_1^0$ to be $2m_\pi$, we have to consider also finite-volume effects, which modify the relation between the two energies to $\tilde{E}_1^0 = 2m_\pi + \delta(L)$. These effects are well known and studied by the lattice community, since they are used to extract scattering amplitudes [109, 110]. Chiral Perturbation Theory (ChPT), which we will discuss later, provides a framework where these amplitudes can be predicted, in terms of some low-energy constants. However, to leading order in ChPT, the zero-isospin $\pi\pi$ scattering amplitude [111, 112] entering in the definition of $\delta(L)$ is independent from those[4] and given only in terms of the pion decay constant and mass,

$$m_\pi a_0^{I=0} = \frac{7m_\pi^2}{32\pi f_\pi^2} 2\left[1 + O\left(\frac{m_\pi^2}{(4\pi f_\pi)^2}\right)\right], \quad \delta(L) = -\frac{4\pi m_\pi a_0^{I=0}}{m_\pi^2 L^3}\left[1 + O\big((f_\pi L)^{-1}\big)\right]. \quad (5.13)$$

At physical pion masses $m_\pi a_0^{I=0} \approx 0.22$ and $\delta(L)$ is consequently expected to be small. For our ensembles, eq. (5.13) predicts shifts in the two-pion state ranging, approximately, from 60 to 10 MeV. If we further neglect these finite-volume effects, using f_P in eq. (5.11) we obtain the last simplification [11]

$$f_\mathrm{P}(x_0, y_0) \propto \sinh\left[(x_0 - \tilde{T}/2)m_\pi\right], \quad (5.14)$$

where $\tilde{T}$ is now a free parameter, which absorbs part of the contribution of η_X^T.

The spectral quantities we are after, are not only the pseudo-scalar masses appearing in the exponential decay, but also the pion-to-vacuum matrix elements. In order to remove the dependence on $|\phi_\pi(y_0)\rangle$ in eq. (5.10) let us consider the quantity

$$L^3 f_\mathrm{P}(T - y_0, y_0) = e^{-m_\pi(T-2y_0)} \langle \phi_\pi(y_0)|\pi, 0\rangle\langle\pi, 0|\phi_\pi(y_0)\rangle\,, \quad (5.15)$$

and its ratio with f_A and f_P [108]

$$\frac{f_X(x_0, y_0)}{L^{3/2}\sqrt{f_\mathrm{P}(T - y_0, y_0)}} = \left[1 + \eta_X^T e^{-\tilde{E}_1^0(T-x_0)} + O(e^{-\tilde{E}_2^0(T-x_0)})\right]\langle 0, 0|\hat{X}|\pi, 0\rangle e^{-m_\pi(x_0 - T/2)}\,. \quad (5.16)$$

[3] The label n is understood to take into account also possible degeneracies of states. For example, a two-particle state with back-to-back propagation has a degeneracy associated to the three possible spatial directions.

[4] The factor 2 appearing in the scattering amplitude in eq. (5.13) comes from the normalization of $f_\pi = \sqrt{2}F_\pi \approx 130\,\mathrm{MeV}$.

At this point, the extraction of the matrix element $\langle 0,0|\hat{X}|\pi,0\rangle$ can be performed in three ways: through fits to the ratio in eq. (5.16) (possibly in a range where the excited states can be neglected) or by averaging plateaus of the following two observables

$$\langle 0,0|\hat{X}|\pi,0\rangle = \frac{f_X(x_0,y_0)}{L^{3/2}\sqrt{f_{\mathrm{P}}(T-y_0,y_0)}} e^{m_\pi(x_0-T/2)} + O(e^{-\tilde{E}_1^0(T-x_0)}) + O(e^{-(\tilde{E}_1^\pi - m_\pi)x_0}) , \quad (5.17)$$

$$\langle 0,0|\hat{X}|\pi,0\rangle = \left[\frac{|f_X(x_0,y_0)f_X(x_0,T-y_0)|}{L^3 f_{\mathrm{P}}(T-y_0,y_0)}\right]^{1/2} + O(e^{-\tilde{E}_1^0(T-x_0)}) + O(e^{-(\tilde{E}_1^\pi - m_\pi)x_0}) , \quad (5.18)$$

the first introduced in Ref. [108], in the context of the Schrödinger functional, and the second proposed in Ref. [113]. Clearly, all methods have to deal both with boundary effects and excited states at short source-sink separations. Indeed, in all cases, a range in x_0 where these additional contributions can be neglected needs to be defined, taking into account the statistical accuracy of the data.

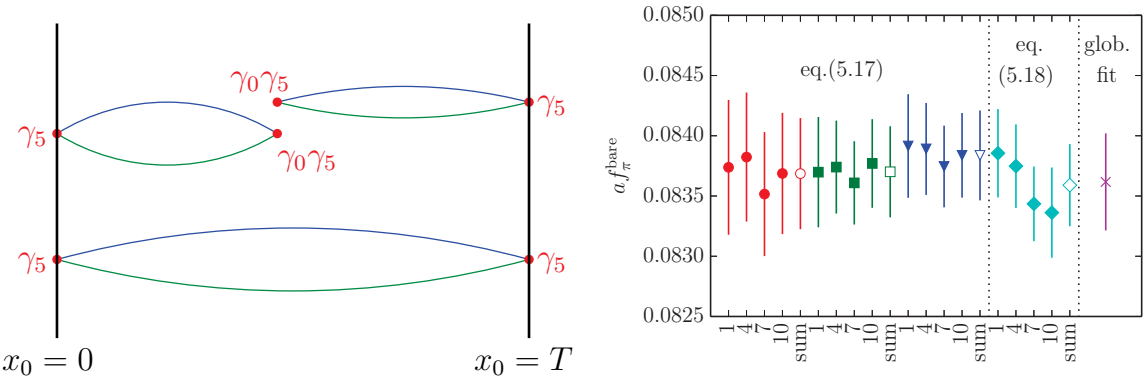

Figure 5.2: *Left*: sketch of the pseudo-scalar two-point functions involved in eq. (5.18), with $X = A_0$. The boundary-to-boundary correlator, namely $f_{\mathrm{P}}(T-y_0,y_0)$, is used to normalize the product of the other two correlation functions. *Right*: computation of the bare pion decay constant on the ensemble H101. The x-axis labels the position of the sources y_0 of the measured correlation functions (filled symbols), while 'sum' (open symbols) refers to the average of the vacuum expectation value of f_π computed from the displaced correlators. We tested eq. (5.17) with several definitions of the pseudo-scalar mass in the exponent: the effective mass as a function of x_0 (circles) and its plateau average (squares), see eq. (5.24), and the mass obtained from the fit (triangles) to the two-point functions. We computed the pion-to-vacuum matrix element also according to eq. (5.18), where the exponential term automatically drops out, and we performed a global fit to f_{P} and f_{A} using eq. (5.16). We do not observe a significant difference in the final errors obtained from the various methods.

In Ref. [113] we have tested all the three methods on the ensemble H101. They gave compatible results with the same errors, thus concluding that there is no preferable strategy (this statement is anyhow relative to the actual precision of the data, which fluctuates between half and one percent). The results shown in Figure 5.2 come from plateau averages and fits performed in a region sufficiently far from the boundaries.

The presence of the open boundaries breaks translation invariance, preventing us from freely displacing the sources along the time direction. In Ref. [113], the possibility to profit from the average over several source positions has been studied on H101 as well. We concluded that it does not improve the final accuracy. This is due to the observation of strong correlations, in the center of the lattice, among the "displaced" two-point functions. The error bars corresponding to the label 'sum' in the right panel of Figure 5.2 confirm this.

The only left invariance is under time reversal transformations. Hence, to improve the signal, we always measure the mirrored correlation functions of eq. (5.1) ($(x_0, y_0) \to (T - x_0, T - y_0)$), and we consider the average

$$f_X(x_0, y_0) = \frac{1}{2}\big[f_X(x_0, y_0) + f_X(T - y_0, T - x_0)\big] \,. \tag{5.19}$$

To obtain plateaus as large as possible for the quantities under study, we always measure the two-point functions with sources placed on the first time slice.

5.1.2 Fit quality

The whole analysis, as we will see in the following, is practically based on fits to the data points. Hence, let us introduce now a few statistical tools and their corresponding notation (for more details see Ref. [114]). Assuming that a set of measurements y_i, with errors σ_i, is described by a function f, depending on the corresponding set of x_i and some parameters a_α, from the minimization of the "naive" chi-square

$$\chi^2 = E^T W E \,, \quad E_i = f(x_i, \{a_\alpha\}) - y_i \,, \quad W = \mathrm{diag}(\sigma_1^2, \sigma_2^2, \ldots, \sigma_N^2)^{-1} \,, \tag{5.20}$$

we obtain the values of the parameters $\{a_\alpha\}$. The quantity defined in eq. (5.20) is called naive since the covariances among the points y_i are neglected. In fact, the real χ^2, for this type of problems, is defined by $W = C^{-1}$, the inverse of the covariance matrix C, whose entries are particularly difficult to compute with a sufficient precision, due to the limited statistics available.

Instead it is possible to compute the expectation value of the χ^2, assuming that the data points y_i are normally distributed. If they fluctuate around $f(x_i, \{A_\alpha\})$, with probability density function depending on the covariance matrix and with $\{A_\alpha\}$ being the "true" values of the parameters, the expectation value of the χ^2 defined in eq. (5.20), which we

call "expected" χ^2 or χ^2_{exp} [115], can be analytically computed (by Taylor expanding f inside the vector E around the solutions $\{A_\alpha\}$)

$$\chi^2_{\text{exp}} = \text{tr}\,(1 - P_\phi) W^{1/2} C W^{1/2}\,. \tag{5.21}$$

Note that W can be any weight matrix but must coincide to eq. (5.20) if we want to compare the two definitions of the χ^2. The projector P_ϕ spans the space defined by $\{W^{1/2}\partial_\alpha f(x_i, \{a_\alpha\})\}$ and the dimension of the identity matrix is given by the total number of points.

For correlated fits, where $W = C^{-1}$, χ^2_{exp} reduces to the (usual) number of degrees of freedom (dof). Roughly speaking, in the case of naive χ^2 minimization, the χ^2_{exp} returns an "effective number of degrees of freedom" and the corresponding reduced χ^2, given by $\chi^2/\chi^2_{\text{exp}}$, is used to judge the quality of the fits. Together with this ratio, also the Q-value is used to monitor the quality of a fit. It corresponds to the probability that a certain value of the χ^2 is larger than the "measured" one (obtained from the minimization process) by chance.

5.1.3 Excited states contaminations

As we have seen in eq. (5.11), close to the boundary we expect to see excited states. Moreover, when the distance between source and sink is not large enough, excited states corresponding to the energy levels $\tilde{E}^\pi_1, \tilde{E}^\pi_2, \ldots$ are expected as well. Therefore our general strategy to define a plateau, proposed in Ref. [12] for open boundary conditions, is to find the set of points where neglecting an additional state produces a systematic error N_σ times smaller than the statistical one, with $N_\sigma = 3$ or 4.

Let us assume to have an observable A, which shows a plateau far from the boundaries, and to perform a fit of the form

$$A(x_0) = c_0 + c_1 e^{-E_1 x_0}\,, \tag{5.22}$$

in a suitable interval[5] in x_0.

The condition

$$\sigma_A(x_{0,\text{min}}) \geq N_\sigma c_1 e^{-E_1 x_{0,\text{min}}}\,, \tag{5.23}$$

automatically defines a plateau in x_0 where the contributions coming from the excited state with energy E_1 is negligible. This procedure applies to quantities such as the smooth energy density, the matrix elements defined in eq. (5.17) and eq. (5.18) or the effective mass

$$m_{\text{eff}}(x_0 + a/2, y_0) = \log \frac{f_{\text{P}}(x_0, y_0)}{f_{\text{P}}(x_0 + a, y_0)}\,, \tag{5.24}$$

[5] This interval is chosen by fixing one extreme in the bulk of the lattice, whereas the other is varied in a region close to the boundary. The first time slice, towards the middle of the lattice, where the reduced-χ^2, $\chi^2/\chi^2_{\text{exp}}$, is approximately 1, defines the other extreme of the fit range.

as they approach the boundaries. Note that for $m_{\rm eff}$ or eq. (5.17), two independent fits of eq. (5.22) are required for the case when the sink is close to the source or to the boundary, thus leading to asymmetric plateaus. For observables, which are symmetric under time reversal, such as $t^2E(t)$ or the product of two-point functions in eq. (5.18), the following functional form can be applied, instead of eq. (5.22),

$$A(x_0) = c_0 + c_1 e^{-E_1(T/2)} \cosh\left[(x_0 - T/2)E_1\right], \tag{5.25}$$

and the criterion in eq. (5.23) is modified accordingly.

In the extraction of the pion and kaon masses, we have chosen a slightly different approach [12], as we computed them directly by fitting $f_{\rm P}$. As a first step, we determine the value of x_0/a, close to the boundary at $x_0 = 0$ and also to the source $y_0 = a$, where excited states can be neglected. We fit the pseudo-scalar correlation functions at fixed y_0 with

$$f_{\rm P}(x_0, y_0) = c_0 e^{-m x_0} + c_1 e^{-E_1 x_0}, \tag{5.26}$$

in a range where one extreme is at $x_0 \simeq T/3$ (to be able to neglect the contributions from the boundary at $x_0 = T$), and the other determined again by $\chi^2/\chi^2_{\rm exp} \approx 1$. In this case the criterion in eq. (5.23), defining $x_{0,\rm min}$, becomes

$$\frac{1}{N_\sigma}\sigma_{m_{\rm eff}}(x_{0,\rm min}) \geq \log\left(\frac{1 + c_1/c_0 e^{-(E_1-m)x_{0,\rm min}}}{1 + c_1/c_0 e^{-(E_1-m)(x_{0,\rm min}+a)}}\right). \tag{5.27}$$

Since the sources y_0 are placed close the boundary at $x_0 = 0$, we expect to observe two different behaviors when the two boundaries are approached. Using the strategy described above also when the sink is approaching $x_0 = T$ would give particularly small plateaus. As we have explained in the previous Sections, in this situation a two-pion state is the expected candidate for the first excited state. Hence, we fit the pseudo-scalar correlators with a sinh-form as in eq. (5.14) on a wider plateau

$$f_{\rm P}(x_0, y_0) = c_0 e^{-m x_0} + c_1 e^{-m(2T - x_0)}, \tag{5.28}$$

instead of using eq. (5.26) in the range where the second state can be neglected. From a larger plateau we obtain a (slightly) more precise estimator[6] of the pseudo-scalar masses and we are able to use from 60% to 80% of our lattices, thus discarding a relatively small portion close to the boundaries. Nevertheless, to cross-check our estimates, we compute the effective mass defined in eq. (5.24) in a range where the condition in eq. (5.23) is satisfied both for $x_{0,\rm min}$ and $x_{0,\rm max}$.

We account for systematic effects given by an additional excited state close to the boundary at $x_0 = T$, by verifying that the contribution of the third exponential in

$$f_{\rm P}(x_0, y_0) = c_0 e^{-m x_0} + c_1 e^{-m(2T - x_0)} + c_2 e^{-E_1(T - x_0)}, \tag{5.29}$$

[6]Due to the presence of correlations along the time direction, the errors do not decrease much when larger plateaus are considered.

is smaller compared to the uncertainty of the effective mass and exactly as before, we obtain a criterion which defines $x_{0,\mathrm{max}}$, while $x_{0,\mathrm{min}}$ is held fixed.

Moreover, to avoid uncertainties due to the finite-volume effects in the energy of the two-pion state (see previous Sections), we parametrize this shift according to

$$f_{\mathrm{P}}(x_0, y_0) = \tilde{c}_0 e^{-\tilde{m} x_0} + \tilde{c}_1 e^{-(\tilde{m}+\delta)(2T-x_0)} \,. \tag{5.30}$$

In the end, we always define our definitive fit ranges by checking that on the one hand the systematic effects of the third exponential fit above are small, with the usual criterion, and on the other hand that the masses extracted from eq. (5.30) or from eq. (5.28) are compatible. Once $x_{0,\mathrm{min}}$ and $x_{0,\mathrm{max}}$ are known we use eq. (5.28) to compute the meson masses from the pseudo-scalar correlators f_{P}.

5.1.4 Renormalization and $O(a)$-improvement

The hadronic masses extracted from the correlation functions given in eq. (5.1), do not require renormalization as they are eigenvalues of the Hamiltonian. They suffer, like all other observables, from cutoff effects, which start at order a in theories breaking chiral symmetry such as the Wilson formulation of QCD (as we have seen in Chapter 2). According to Symanzik's improvement program they can be canceled by suitable counter-terms added to the action and to the operators. The $O(a)$-improved action used to generate our ensembles has already been described in Chapters 2 and 4, and we now present the improvement of the correlation functions defined in eq. (5.1). Out of the composite operators A_μ and P only the axial one is affected by $O(a)$ additive corrections, which modifies f_{A} according to eq. (2.31)

$$f_{\mathrm{A}}^{rt,\mathrm{I}}(x_0, y_0) = f_{\mathrm{A}}^{rt}(x_0, y_0) + a c_A \tilde{\partial}_0 f_{\mathrm{P}}^{rt}(x_0, y_0) \,, \quad \tilde{\partial}_0 = \frac{1}{2}(\partial_0 + \partial_0^\star) \,. \tag{5.31}$$

From $f_{\mathrm{A}}^{\mathrm{I}}$ and the usual f_{P}, $O(a)$ improved matrix elements can be extracted with one of the methods discussed before. To obtain physical quantities, such as decay constants, they must undergo multiplicative renormalization, as already explained in eq. (2.32) and eq. (2.33). For the flavor combination 12, which is associated with the pion, we obtain

$$Z_A(\tilde{g}_0)\big[1 + a\bar{b}_A \mathrm{tr} M + a b_A m_{\mathrm{q},12}\big] \langle 0, 0 | \hat{A}_0 | \pi, 0 \rangle = f_\pi m_\pi (2 m_\pi L^3)^{-1/2} \,, \tag{5.32}$$

and similarly for the kaon, by replacing $12 \leftrightarrow 13$ and $\pi \leftrightarrow K$. The term in parenthesis on r.h.s. of eq. (5.32) is the usual normalization of one-particle states, due to the fact that we have chosen $\langle \alpha, n | \beta, m \rangle = \delta_{\alpha\beta}\delta_{nm}$ (cross-check against Section 2.4 where we adopt the common normalization). The finite renormalization factor Z_A, defined in Chapter 2, has been computed non-perturbatively in a separate work, yet unpublished. For more details

see Appendix B. Note also that, given our definitions of $f_{\rm A}$ and $f_{\rm P}$, bare quark masses always appear in the combination

$$m_{{\rm q},rt} = \frac{1}{2}(m_{{\rm q},r} + m_{{\rm q},t})\,, \quad m_{\rm q,u} = m_{\rm q,d} = m_{\rm q,12}\,, \quad m_{\rm q,s} = 2m_{\rm q,13} - m_{\rm q,12}\,. \tag{5.33}$$

Beyond the mesonic quantities listed so far, quark masses are the other objects we investigate in this thesis. Before turning to those let use briefly list here the known results of the improvement coefficients, which will be used in the rest of the analysis. For the Lüscher-Weisz improved gauge action and Wilson fermions, the knowledge of these numbers is purely perturbative, and limited to 1-loop results [116]

$$\begin{aligned} b_A &= 1 + 0.0881(1) C_F g_0^2 + O(g_0^4)\,, \\ b_P &= 1 + 0.0890(1) C_F g_0^2 + O(g_0^4)\,, \quad C_F = 4/3\,. \end{aligned} \tag{5.34}$$

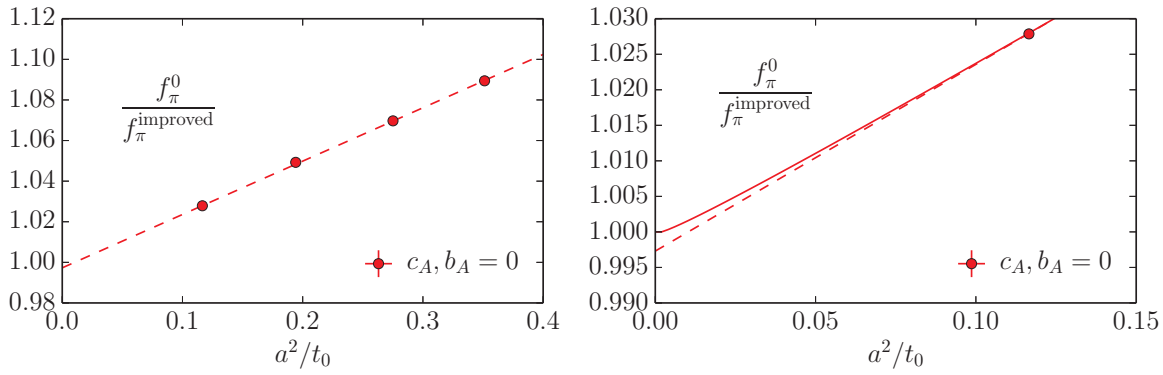

Figure 5.3: Ratio of the un-improved ($c_A = b_A = 0$) over the improved (c_A, but $b_A = 0$) pion decay constant. The pion and kaon masses are fixed in units of t_0, through $\phi_4 \approx 1.15$, and mistunings in this variable do not have a significant impact on the ratio. The dashed line is a linear fit in a^2 to the four points, whose continuum value differs from 1 by 0.27(3)%. Correlations between numerator and denominator make the ratios turn out to be extremely precise. Renormalization factors cancel as well. In the right panel we zoom in a region closer to the continuum limit and we show the results of the fits constrained to 1 but with a and a^2 terms.

In Figure 5.3 we show the effects of the improvement coefficient c_A on the pion decay constant at the symmetric point. As we see from the left panel, c_A produces an effect on the 10% level at our coarsest lattice spacing. For b_A much smaller effects are expected, around 1%, since it is small at 1-loop and multiplied with am-terms. The data shows a rather good a^2 scaling and we interpret the fact that it does not extrapolate to 1,

as residual $O(a)$ effects (below the percent, see Figure 5.3). We try to model them by fitting the function $1 + b_0 a/\sqrt{t_0} + b_1 a^2/t_0$, whose results are plotted in the right panel of Figure 5.3. We observe one order of magnitude between the two coefficients, $-10b_0 \approx b_1$, and we conclude that c_A contributes mostly to $O(a^2)$ discretization effects of the decay constants and has only a small a piece.

A similar a^2-dominance is observed in the combination $\sqrt{8t_0} f_\pi$, Figure 5.4, where linear fits in a^2 to the improved and un-improved data agree within less than one standard deviation in the continuum limit. In these quantities errors are much larger compared to the ratios shown in Figure 5.3, and there is a contamination, concerning a^2 effects, coming from the determination of Z_A. In particular, what we learn from this plot, is that the size of the a^2 contributions given by c_A and Z_A are equivalent.

Note also that along our chiral trajectory the strange quark mass becomes larger and the b_A-corrections to f_K are expected to be relevant at the physical point. Using the 1-loop values in eq. (5.34) they are expected to be around 1%, the size of the statistical accuracy of our results.

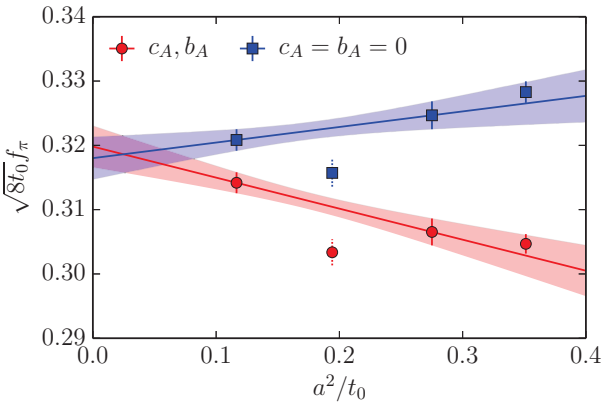

Figure 5.4: Continuum extrapolation in a^2 of $\sqrt{8t_0} f_\pi$ at the symmetric point. The two linear fits exclude the rightmost point and the point with dashed error bars, since it is affected by finite-volume effects, which we discuss later.

5.1.5 Quark masses

In Chapter 2 we have discussed in what terms quark masses undergo additive renormalization, for discretizations of the fermion Lagrangian breaking chiral symmetry. Our ensembles have been generated with 2+1 $O(a)$-improved Wilson fermions, therefore the knowledge of the critical mass is in principle needed. This would require a dedicated study. However the problem can be bypassed by computing the so-called PCAC masses.

Starting from the Ward Identity in eq. (2.20), a suitable definition for the (bare) quark masses is

$$m_{rs}(x_0) = \frac{\tilde{\partial}_0 f_{\rm A}^{rs}(x_0) + a c_A \partial_0 \partial_0^* f_{\rm P}^{rs}(x_0)}{2 f_{\rm P}(x_0)}\,, \tag{5.35}$$

usually called PCAC masses, with c_A being the coefficient of the $O(a)$ counter-term of the axial current in eq. (2.31). In this thesis we use the non-perturbative determination of c_A of Ref. [117]. Renormalized PCAC masses can be obtained (recall the discussion on Symanzik's improvement program) by combining eq. (2.32) and eq. (2.33) with eq. (5.35)

$$m_{rs,\rm R} = \frac{Z_A}{Z_P}\frac{1 + a\bar{b}_A {\rm tr}M + a b_A m_{{\rm q},rs}}{1 + a\bar{b}_P {\rm tr}M + a b_P m_{{\rm q},rs}} m_{rs}\,. \tag{5.36}$$

Eq. (5.36) and eq. (2.29) are equivalent, up to cutoff effects. From this equivalence, a relation between the bare subtracted quark masses and the bare improved PCAC masses can be inferred (note that we drop the dependence of the Z factors and b coefficients on the renormalization scale and on $\tilde{g}_0$)

$$m_{rs,\rm R} = m_{{\rm q},rs}^{\rm R} \quad \rightarrow \quad m_{{\rm q},rs} = \frac{Z_A}{Z_m Z_P} m_{rs} - (r_m - 1)\frac{{\rm tr}M}{N_{\rm f}} + O(am^2)\,. \tag{5.37}$$

Bare subtracted quark masses enter in the improvement of many quantities, e.g. eq. (5.32). However, since we do not know the value of $\kappa_{\rm cr}$ for our four values of β, we always make use of eq. (5.37) to express renormalized quantities in terms of bare PCAC masses. To this change of variables we associate the following change of notation[7] ($X = A, P$)

$$a b_X m_{{\rm q},rs} \rightarrow a\tilde{b}_X m_{rs}\,, \quad \tilde{b}_X \equiv \tilde{Z} b_X\,, \quad \tilde{Z}(\tilde{g}_0) = \frac{Z_A(\tilde{g}_0)}{Z_m(a\mu,\tilde{g}_0) Z_P(a\mu,\tilde{g}_0)}\,. \tag{5.38}$$

In the following analysis the available perturbative knowledge of the improvement coefficients $\tilde{b}_X$ is used. The one-loop result of $\tilde{Z}$ is taken from Ref. [118] and does not contribute, at this order, to the difference $\tilde{b}_A - \tilde{b}_P$

$$\tilde{Z}(\tilde{g}_0) = 1 - 0.0703\tilde{g}_0^2\,, \quad \tilde{b}_A - \tilde{b}_P = -0.0012(2) g_0^2 + O(g_0^4)\,. \tag{5.39}$$

Note that replacing $\tilde{g}_0$ with g_0 in the perturbative definitions of the $\tilde{b}_X$ coefficients amounts to an a^2 effect. Let us remind the reader that an alternative method to extract the pseudo-scalar decay constants can be defined using the PCAC relation (see for instance Ref. [119]). If we consider eq. (5.18) with $X = P$, a suitable plateau average returns the matrix element $\langle 0,0|\hat{P}|\pi,0\rangle$. Using the expansion of the correlation functions appearing in the PCAC relation eq. (2.20), it is possible to relate pseudo-scalar and axial matrix elements (up to cutoff effects)

$$\langle 0,0|\hat{A}_0|\pi,0\rangle = \langle 0,0|\hat{P}|\pi,0\rangle \frac{2m_{12}}{m_\pi}\,. \tag{5.40}$$

[7] In the literature the combination of Z factors appearing in eq. (5.37) is usually denoted by $Z = (Z_m Z_P)/Z_A$.

5.1.6 Boundary effects

The presence of the boundaries is clearly visible in the profile of the observables. In particular in all cases under study, strong lattice artifacts are observed close to $x_0 = 0$ and T. One of the reasons for this behavior comes from the $O(a)$ counter-terms at the boundaries: for their coefficients, namely c_G and c_F, we have used the tree level values, thus leaving room for $O(ag_0^2)$ effects. In Figure 5.5 we show the profile of a purely gluonic observable, $t_0^2 E(t_0)$, and of the ratio of the bare light quark mass $m_{12}(x_0)$ over its plateau average m_{12}^{aver}, which is independent from renormalization factors and improvement coefficients. In the former, changing the values of κ does not produce a visible effect in the various curves, while for the latter sea quark effects are observed.

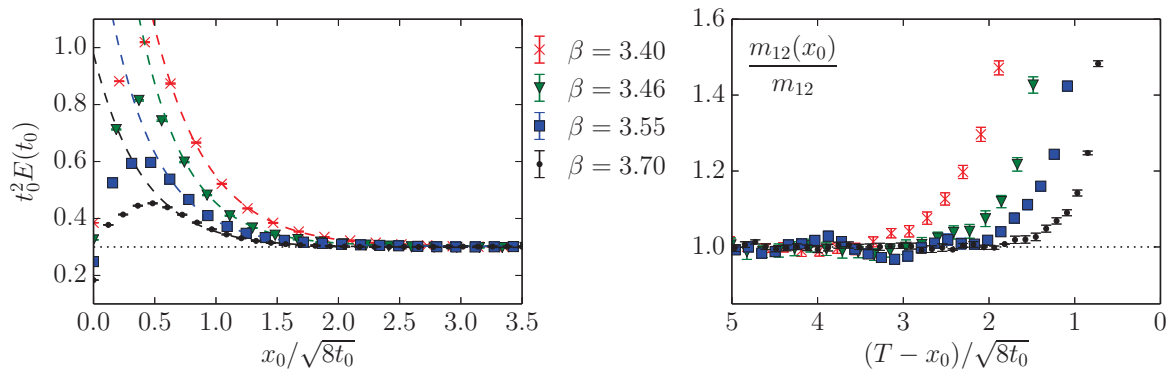

Figure 5.5: The plots show the profile of two observables along the time direction, expressed in units of $\sqrt{t_0}$, for the four ensembles at the symmetric point, where $m_\pi \approx 420\,\text{MeV}$. *Left*: $t_0^2 E(t_0)$; the lines represent independent fits of eq. (5.22), from which $x_{0,\text{min}}/\sqrt{8t_0}$ is found to be approximately constant, around 4. This is a sign of dominant $O(a)$ artifacts introduced by the boundaries. *Right*: ratio of the bare light quark mass over its plateau average; to demonstrate the presence of boundary effects we show how the PCAC masses approach the boundary at $x_0 = T$. We show the limit $x_0 \to T$ instead of small x_0 because in the latter excited states coming from short source-sink separations overlap with the boundary contributions. Recall that we place the sources of the two-point functions on the first time slice of the lattice.

The PCAC masses are derived from an identity among operators. This means that all deviations from a flat behavior immediately reveal the presence of lattice artifacts. This is not the case for the energy density, where a (yet unknown) physical profile close to the boundary does exist and cutoff effects can be judged only through the relative comparison of different β. In the end, what is relevant for our analysis, is how fast they approach the plateau according to the criterion defined in eq. (5.23). For the energy density we find

that excited states become negligible at $x_0/\sqrt{8t_0} \approx 4.2$ for all values of β, while for the PCAC masses this bound varies from $x_0/\sqrt{8t_0} \approx 2.5$ to 4.2, depending on the sea quark masses and on the lattice spacing.

For the decay constants, the situation is similar concerning relative discretization effects, but more interesting in terms of sea quark effects. In particular, if the matrix elements of f_π and f_K are computed according to eq. (5.18), with $X = P$ and with sources placed at $y_0 = a$ (see eq. (5.40) for the multiplicative factor relating $\langle 0,0|\hat{P}|\pi,0\rangle$ to f_π and f_K). The cancellation of the exponential factor in $f_\mathrm{P}(x_0,y_0)\cdot f_\mathrm{P}(x_0,T-y_0)$ is the practical advantage in eq. (5.18) w.r.t. to eq. (5.17). Moreover, the resulting product is symmetric under time reversal, which allows to treat excited states in one step, according to eq. (5.25).

When x_0 approaches one of the boundaries, say $x_0 = 0$, two different contributions interfere: $\exp(-\tilde{E}_1^0 x_0)$ coming from the $f_\mathrm{P}(x_0, T-y_0)$ approaching the boundary (recall eq. (5.11), where we take $\tilde{E}_1^0 = 2m_\pi$)

$$\frac{f_\mathrm{P}(x_0,T-y_0)}{L^{3/2}\sqrt{f_\mathrm{P}(y_0,T-y_0)}} \overset{x_0\to 0}{\approx} \langle \pi,0|\hat{P}|0,0\rangle e^{m_\pi(x_0-T/2)}[1+\eta_P^0 e^{-2m_\pi x_0}]\,, \tag{5.41}$$

and $\exp(-\tilde{E}_1^\pi(x_0-y_0))$ from the short source-sink separation of $f_\mathrm{P}(x_0,y_0)$, (which we assume to be a 3-pion state with energy $\tilde{E}_1^\pi = 3m_\pi$)

$$\frac{f_\mathrm{P}(x_0,y_0)}{L^{3/2}\sqrt{f_\mathrm{P}(y_0,T-y_0)}} \overset{x_0\to 0}{\approx} \langle 0,0|\hat{P}|\pi,0\rangle e^{-m_\pi(x_0-T/2)}\Big[1+\frac{\langle 0,0|\hat{P}|\pi,1\rangle}{\langle 0,0|\hat{P}|\pi,0\rangle}e^{-2m_\pi(x_0-y_0)}\Big]\,. \tag{5.42}$$

Note that the dependence on y_0 appears only through the source-sink separation of the three-pion state, since the boundary contributions contained in $\phi_\pi(y_0)$ are canceled by the denominator.

When we multiply the l.h.s. of eq. (5.41) with the one in eq. (5.42) we obtain the square of the quantity defined in eq. (5.18). From the expansions above we can read off the term corresponding to the first excited state

$$\left[\frac{\langle \pi,0|\hat{P}|0,1\rangle}{\langle \pi,0|\hat{P}|0,0\rangle}\frac{\langle 0,1|\Omega\rangle}{\langle 0,0|\Omega\rangle}+\frac{\langle 0,0|\hat{P}|\pi,1\rangle}{\langle 0,0|\hat{P}|\pi,0\rangle}e^{2m_\pi y_0}\right]e^{-2m_\pi x_0}\,. \tag{5.43}$$

In Figure 5.6 we plot the behavior of matrix elements extracted from the combination in eq. (5.18), with $X = P$ on the top panel and $X = A_0$ in the bottom one. The two observables show two different profiles as they approach the boundaries. For the axial correlation function no particular difficulties are encountered in the estimates of the excited states, which can be done according to eq. (5.25), while for the pseudo-scalar correlator a strong dependence on the pion mass is visible. For the latter the estimate of systematic uncertainties is more difficult, as fits with two excited states, rather than one, are more stable as the bump becomes more pronounced. For these reasons, in our

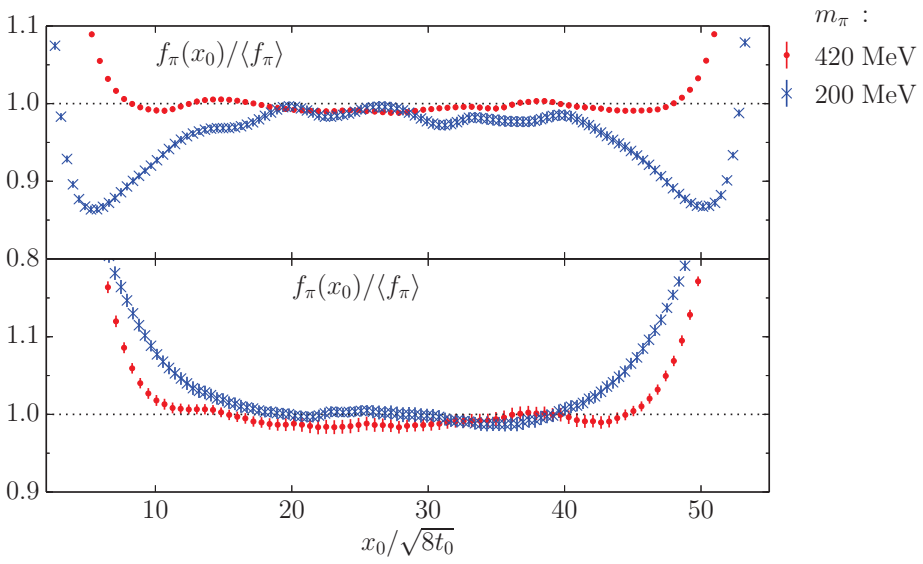

Figure 5.6: Behavior of the pion decay constants as they approach the boundaries. A direct comparison between the different curves is possible due to the normalization with the plateau average, which avoids also renormalization factors and improvement coefficients. Curves at pion masses between 420 and 200 MeV lie between the two shown and we do not plot them for a better legibility of the figures. *Top*: profile along the time direction of the pion-to-vacuum matrix element computed from eq. (5.18) using f_P. The factor in eq. (5.40), involving m_π and m_{12}, is used to convert $\langle 0,0|\hat{P}|\pi,0\rangle$ into the axial matrix element. A significant dependence on the quark mass is observed close to the boundary. Data from $\beta = 3.4$ and $\beta = 3.55$ is used. *Bottom*: f_π is directly evaluated from eq. (5.18) with f_A. In this case fits with one excited state are reliable at all pion masses.

analysis we do not use these estimates of f_π and f_K, but only those showed in the bottom panel of Figure 5.6.

As we have seen for other quantities, cutoff effects close to the boundaries are relatively pronounced and they are present also in this case. However, by comparing two curves at $\beta = 3.4$ and 3.55 and at the same value of the pion mass, namely the ensembles H105 and N200, we conclude that they can not be the dominant contributions to the bumps. Instead, they are probably a consequence of the physical dependence of the prefactor multiplying the two-pion state in eq. (5.43) on m_π. In Ref. [120] some of the matrix elements appearing in eq. (5.43) have been computed in ChPT. Unfortunately, since we do not know the contribution of the boundary state $|\Omega\rangle$, it is difficult to explain the observed behavior, even qualitatively.

5.1.7 Twisted-mass reweighting

In Chapter 4 we have discussed the presence of a twisted-mass term in our simulated action. Beyond the difficulties which might occur in the computation of the associated reweighting factor, a second issue is the impact of their fluctuations on the reweighted observables. The choice of the TM mass μ is always at the origin of the problem, as it controls the occurrence of gauge-field configurations with close-to-zero eigenvalues of the Dirac operator.

Let us consider a generic observable O and a generic reweighting factor w. In Ref. [113] we have computed the variance of the reweighted observable (notation taken from eq. (4.3))

$$\langle O^2 \rangle - \langle O \rangle^2 = \langle w^{-1} \rangle \langle (O - \langle O \rangle)^2 w \rangle \,. \tag{5.44}$$

In the same work, we presented a numerical study of the variance in eq. (5.44), where we examined its dependence upon the reweighting factor $w = W \cdot W_1$, with W the TM reweighting factor defined in eq. (4.4) and W_1 the RHMC reweighting factor. Varying the twisted mass μ, from 1 to 5 MeV, has not produced a significant effect on the variance of $O = t^2 E(t)$, for the ensemble H105 ($m_\pi \approx 280\,\mathrm{MeV}$, $\beta = 3.4$). In fact, we do not expect, at the present level of accuracy, to observe a strong dependence of gluonic observables, such as t_0, on the eigenmodes of the fermion determinant and consequently on the TM reweighting factor. For this type of observables, reweighting basically amounts to a tiny increase in the final error.

Unlike t_0, the two-point functions that we use in the analysis are extremely correlated with the reweighting factors. More precisely, they are anti-correlated since, for an exceptional configuration, (assuming single-eigenvalue dominance of the Dirac operator)

$$f_\mathrm{P} \propto \mathrm{tr}\,\{Q^{-2}\} \overset{\lambda \to 0}{\approx} \frac{1}{\lambda^2}\,, \quad W \overset{\lambda \to 0}{\propto} \lambda^2\,, \tag{5.45}$$

and therefore, for particularly small eigenvalues λ, cancellations take place in their product.

In Figure 5.7 the time series of W, f_P and $W f_\mathrm{P}$, for two ensembles differing only by the choice of μ, are presented. The size of the fluctuations of the reweighting factor and the observable are clearly controlled by the twisted mass. The difference between the two cases disappears after reweighting, thus demonstrating the correctness of the method.

Let us remark that the occurrence of these "singular" events, in the Monte Carlo histories of these observables, might depend also on the lattice spacing and the physical volume. In fact, towards the continuum limit, the fluctuations of the reweighting factors are much smaller, also for relatively large values of μ. For instance, in the four ensembles at the symmetric point the product $a\mu$ is fixed to 10^{-3}, which means that μ is growing with β. Nevertheless, smaller fluctuations are observed on the finer lattices.

5.1.8 Results

Starting from these findings, we decided to measure f_{A} and f_{P} with $y_0 = a$ for all ensembles and to use the method described in eq. (5.18) (with $X = A_0$), to extract the matrix elements $\langle 0,0|\hat{A}_0|\pi,0\rangle$ and $\langle 0,0|\hat{A}_0|\mathrm{K},0\rangle$ (K and π are equivalent in terms of quantum numbers and differ only by the energy levels $E_0^{\mathrm{K}} = m_{\mathrm{K}}$, $E_0^{\pi} = m_{\pi}$). The latter are related to the pion and kaon decay constants according to eq. (5.32). In Table 5.1 we report the results of the computation of the meson masses and decay constants, together with the PCAC masses.

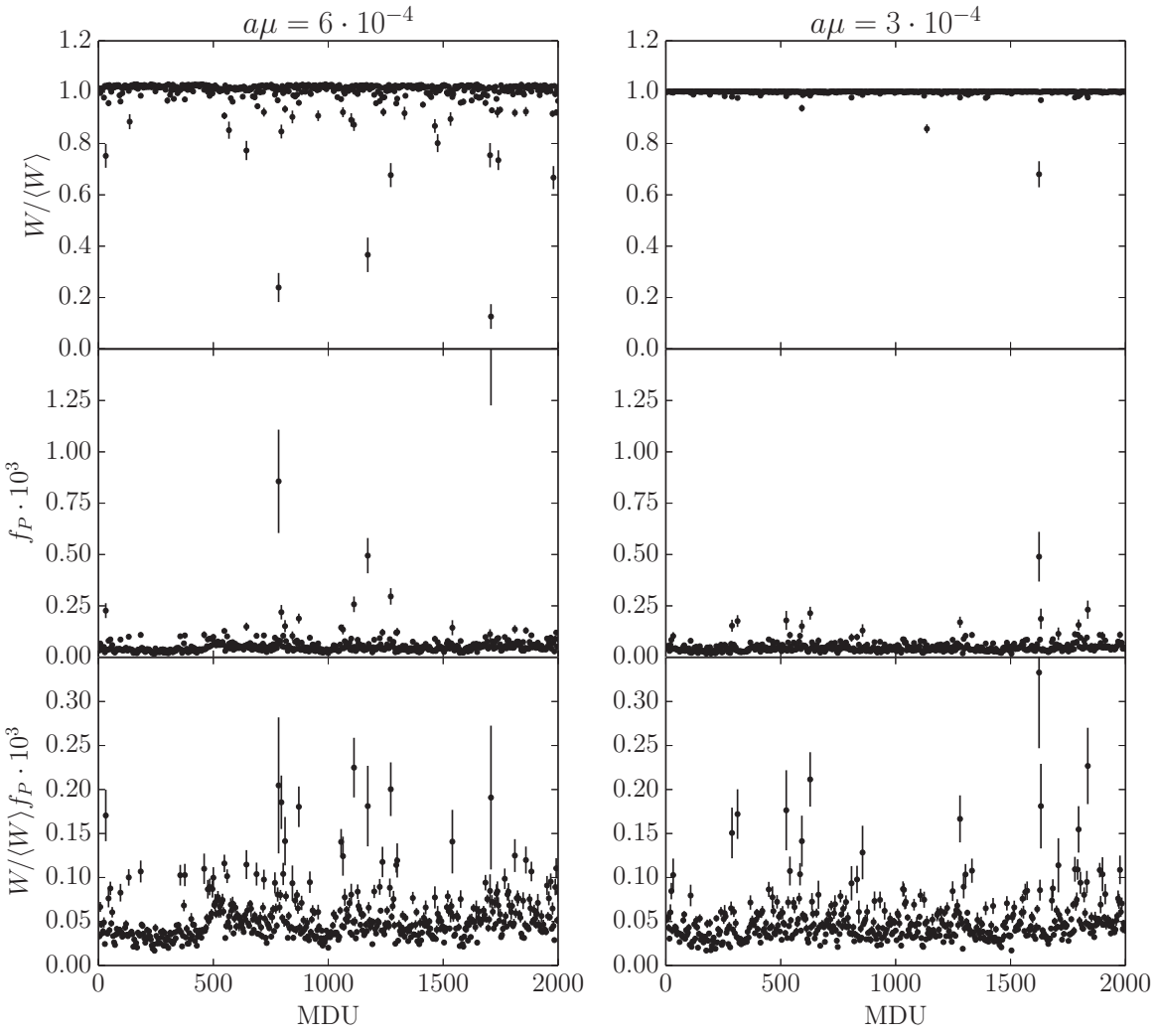

Figure 5.7: Monte Carlo histories of $W/\langle W \rangle$, $f_{\mathrm{P}}(T/2 - a)$ and their product. Left and right panel correspond to two simulations at $\beta = 3.4$ and $m_\pi \simeq 220\,\mathrm{MeV}$, where μ differs by a factor 2. After reweighting the fluctuations of the pseudo-scalar correlators are equivalent in the two cases. Note that in our analysis we always treat the two cases separately, since they are not replica, but we always present averaged results, under the common name C101. More details can be found in Ref. [12].

id	β	t_0/a^2	am_π	am_K	am_{12}	am_{13}	af_π	af_K
H101	3.40	2.8468(61)	0.18273(70)	0.18273(70)	0.009188(30)	0.009188(30)	0.06377(32)	0.06377(32)
U103		2.8836(74)	0.18137(80)	0.18137(80)	0.008920(34)	0.008920(34)	0.06179(75)	0.06179(75)
H102		2.8799(73)	0.15437(70)	0.19164(57)	0.006537(37)	0.010200(33)	0.06035(31)	0.06371(20)
H105		2.9031(73)	0.12170(96)	0.20126(63)	0.003946(41)	0.011273(32)	0.05760(51)	0.06423(29)
C101		2.9085(51)	0.09751(93)	0.20639(40)	0.002491(35)	0.011892(21)	0.05571(41)	0.06370(24)
H106		2.8187(73)	0.1191(18)	0.22471(74)	0.003763(65)	0.013918(44)	0.05782(79)	0.06605(49)
H107		2.7189(88)	0.1591(11)	0.23771(78)	0.006666(43)	0.015331(39)	0.06350(37)	0.06965(31)
C102		2.868(11)	0.0978(21)	0.2183(13)	0.002558(62)	0.013253(65)	0.05764(67)	0.06550(52)
H400	3.46	3.635(13)	0.16360(64)	0.16360(64)	0.008237(30)	0.008237(30)	0.05679(31)	0.05679(31)
H401		3.2456(95)	0.22887(44)	0.22887(44)	0.015810(26)	0.015810(26)	0.06762(26)	0.06762(26)
H402		3.577(21)	0.17752(80)	0.17752(80)	0.009783(45)	0.009783(45)	0.05928(39)	0.05928(39)
H200	3.55	5.150(23)	0.13653(52)	0.13653(52)	0.006862(23)	0.006862(23)	0.04722(35)	0.04722(35)
N200		5.1584(78)	0.09202(61)	0.15059(57)	0.003155(11)	0.008647(10)	0.04415(27)	0.04883(24)
D200		5.1681(68)	0.06542(44)	0.15640(25)	0.001548(14)	0.009387(12)	0.04237(25)	0.04922(20)
N300	3.70	8.580(27)	0.10593(32)	0.10593(32)	0.0055073(58)	0.0055073(58)	0.03790(22)	0.03790(22)
J303		8.631(24)	0.06480(38)	0.11979(23)	0.002026(29)	0.007178(11)	0.03413(44)	0.03835(53)

Table 5.1: Measured values of the pseudo-scalar masses and decay constants, together with the PCAC masses. In the values where the coefficients c_A, $\tilde{b}_A$ and $\tilde{b}_P$ are necessary, they have been used as described in the text. Some of the numbers appearing in this table have already been published in Ref. [12].

5.2 Chiral Perturbation Theory

Chiral symmetry is a fundamental global symmetry in QCD. From the discussions in Chapter 3 on the technical difficulties in carrying out simulations at physical quark masses, we have learned that most of the lattice computations are performed at unphysically heavier up/down quark masses[8]. Hence, a theory to guide the extrapolations to physical masses is needed and must be sought in the framework of the Effective Field Theories.

Let us consider QCD with N_f massless quarks in the continuum. The Lagrangian is symmetric under chiral-flavor rotations of the form $U(N_\mathrm{f})_L \times U(N_\mathrm{f})_R$. As we have seen in Section 2.6.1 the axial $U(1)$ current is anomalous, even at zero quark masses, while the vector $U(1)$ current is preserved and associated to quark-number conservation. If we now restrict our theory to up, down and strange quarks, the lightest in nature, we are left with $SU(3)_L \times SU(3)_R$ transformations.

If the full chiral-flavor symmetry were not broken, we would expect to observe hadron multiplets of parity partners, for example three scalar mesons with the same masses of the pions. Evidently, from the lack of those in the hadron spectrum, we conclude that $SU(3)_L \times SU(3)_R$ must be broken also in the chiral limit, to the smaller subgroup $SU(3)_V$ (note that in the two-flavor theory it corresponds to the isospin symmetry). Indeed, in Ref. [121] it has been proven that the QCD vacuum is invariant under vector rotations, the "diagonal" subgroup of the full symmetry group, in the degenerate-mass limit.

The so-called chiral condensate is the natural order parameter of the chiral symmetry breaking and at zero quark mass, where only $SU(3)_V$ is preserved, it is degenerate in flavor space $\langle \bar{u}u \rangle = \langle \bar{d}d \rangle = \langle \bar{s}s \rangle \neq 0$. The existence of a non-zero chiral condensate would prove the breaking of chiral symmetry, as well.

According to Goldstone's theorem we expect to see $N_\mathrm{f}^2 - 1$ massless bosonic degrees of freedom associated with the broken generators of $SU(N_\mathrm{f})_L \times SU(N_\mathrm{f})_R$. In nature the massless limit is not realized as quarks have positive masses. However, if we restrict ourselves to up, down and strange quarks, their masses are still small compared to the typical QCD scales and for this reason, in the literature, these bosonic fields are often called pseudo-Goldstone bosons, for chiral symmetry would be approximately realized at the level of the Lagrangian. Their corresponding particles must be sought in the pseudo-scalar sector of the mesonic spectrum $J^P = 0^-$: experimentally we "observe" such an octet of particles, since π, K and η are relatively light mesons, compared to the next one in the spectrum, the ρ, which is a vector particle.

The Lagrangian describing the behavior of these (pseudo-)Goldstone particles can be built using the exponential representation of their fields ϕ, $\Sigma = \exp(2i\phi/f)$, to enforce linear representations of the transformation laws, e.g. $\Sigma \to U_L \Sigma U_R^\dagger$, with $U_{L,R} \in SU(3)$.

[8] Moreover, lattice calculations are performed in Euclidean space-time and the analytic continuation to Minkowski space-time for many quantities is not possible. In fact, scattering amplitudes can not be obtained directly from lattice computations. Instead, extracting the parameters of ChPT by lattice calculations, ChPT can be used to predict scattering amplitudes.

Note the presence of the dimensionful quantity[9] f to account for dimensions in the exponent of Σ. The transition from quarks and gluons to pion-like fields is completely dictated by the symmetries of the fundamental theory (Lorentz, parity and chiral invariance, including its spontaneous breaking). Its effects are absorbed in the couplings of the effective theory, which is valid only below a certain threshold and is described by [122]

$$\mathcal{L}_\chi = \frac{f^2}{8}\mathrm{tr}\left(\partial_\mu\Sigma\partial_\mu\Sigma^\dagger\right) + L_1\mathrm{tr}\left(\partial_\mu\Sigma\partial_\mu\Sigma^\dagger\right)^2 + \dots . \tag{5.46}$$

Once quark masses are switched on, chiral symmetry is broken explicitly by the mass term in the QCD Lagrangian and Goldstone bosons become massive as well, even though they remain relatively light. This formally explains the gap, in masses, between the light pseudo-scalar octect and the ρ meson. If the masses are sufficiently small (sufficiently means compared to the typical QCD scales, which are $O(\Lambda_{QCD})$), they can be treated as perturbations of the effective Lagrangian in eq. (5.46). Since the $SU(3)_L \times SU(3)_R$ symmetry must be preserved, quark masses are introduced through a spurion contribution M

$$\mathcal{L}_2 = \frac{f^2}{8}\mathrm{tr}\left(\partial_\mu\Sigma\partial_\mu\Sigma^\dagger\right) - \frac{f^2 B}{4}\mathrm{tr}\left(M\Sigma^\dagger + M^\dagger\Sigma\right), \quad M \to U_L M U_R^\dagger . \tag{5.47}$$

We can keep track of the chiral symmetry breaking in the effective Lagrangian through M and actually break it by setting $M = \mathrm{diag}(m_u, m_d, m_s)$. From the leading order chiral Lagrangian eq. (5.47) the pion mass is easily found $m_\pi^2 = 2B(m_u + m_d)$ and the effective parameter B is related to the chiral condensate through f, $\langle\bar{q}^i q^j\rangle = -f^2 B\delta^{ij}$.

We have briefly seen how Chiral Perturbation Theory (ChPT) can be developed (for an extensive introduction see for example Refs. [123, 124]). In their famous papers, Gasser and Leutwyler extended eq. (5.47) to one-loop for the $SU(2)$ [125] and $SU(3)$ [126] flavor rotations. To obtain results at one-loop level, computing loop diagrams involving the ϕ fields is not sufficient. The theory needs to be renormalized and counter-terms (such as the term proportional to L_1 in eq. (5.46)) are added to the Lagrangian: the difference here, w.r.t. a renormalizable theory, is that new operators are necessary, carrying also new coupling constants, called Low Energy Constants (LEC). They are fixed by matching ChPT and QCD observables at energy scales much smaller than typical QCD scales, or alternatively, through lattice computations. Still, there is a certain amount of predictivity, since only a finite number of counter-terms is needed at each order of the expansion.

5.2.1 SU(3) ChPt

In this thesis we want to investigate the behavior of the pseudo-scalar decay constants as the pion mass decreases along our chiral trajectory, defined by (bare) $\mathrm{tr}M = const.$ In

[9] In this thesis we adopt the notation $f = \sqrt{2}F \approx 130\,\mathrm{MeV}$.

order to extrapolate these observables to the physical point and to the chiral limit for the up-down masses, the predictions of Chiral Perturbation theory may be used.

Let us start by considering the $SU(3)$ expressions for the quantities we are interested in. We do not give here the details on the derivations of the one-loop formulae below and simply report them. To next-to-leading order expansions of the pseudo-scalar meson masses, in the isospin limit $m_{\rm up} = m_{\rm down} = m_{\rm ud}$, are

$$m_\pi^2/(4Bm_{\rm ud}) = 1 + L_\pi - \frac{1}{3}L_{\rm K} + \frac{32Bm_{\rm ud}}{f^2}(2L_8 - L_5) + \frac{32B{\rm tr}M}{f^2}(2L_6 - L_4)) \,, \tag{5.48}$$

$$\begin{aligned} m_{\rm K}^2/(2B(m_{\rm ud} + m_{\rm s})) =& 1 + \frac{2}{3}L_\eta + \frac{16B(m_{\rm ud} + m_{\rm s})}{f^2}(2L_8 - L_5) \\ &+ \frac{32B{\rm tr}M}{f^2}(2L_6 - L_4) \,, \end{aligned} \tag{5.49}$$

whereas for the eta meson mass, we will need only the leading order

$$m_\eta^2 = \frac{4}{3}B(2m_{\rm s} + m_{\rm ud}) = \frac{4}{3}B(2{\rm tr}M - 3m_{\rm ud}) \,. \tag{5.50}$$

We have parametrized the logarithmic contributions with the function L_x defined as

$$L_x = \frac{m_x^2}{(4\pi f)^2} \ln\left(\frac{m_x^2}{\Lambda^2}\right) , \quad x = \pi, {\rm K}, \eta, \tag{5.51}$$

Λ being the energy scale at which the loop integrals are renormalized. The sum of the pion and kaon masses

$$\frac{1}{2}m_\pi^2 + m_{\rm K}^2 = 2B{\rm tr}M(1 + O(m_{\rm ud})) \tag{5.52}$$

is proportional to tr$M$, at tree level, thus justifying our choice of using ϕ_4 as a tuning variable.

5.2.2 Decay constants

The expansions of the pion and kaon decay constants to one-loop in $SU(3)$ chiral perturbation theory are

$$f_\pi/f = 1 - 2L_\pi - L_{\rm K} + \frac{16Bm_{\rm ud}}{f^2}L_5 + \frac{16B(m_{\rm s} + 2m_{\rm ud})}{f^2}L_4 \,, \tag{5.53}$$

$$f_{\rm K}/f = 1 - \frac{3}{4}L_\pi - \frac{3}{2}L_{\rm K} - \frac{3}{4}L_\eta + \frac{8B(m_{\rm s} + m_{\rm ud})}{f^2}L_5 + \frac{16B(m_{\rm s} + 2m_{\rm ud})}{f^2}L_4 \,. \tag{5.54}$$

The symmetry of the theory is such that the low energy constants appearing in eq. (5.53) and eq. (5.54) are the same. This leads to a straightforward combination of the two

observables where the leading dependence on the quark masses is proportional to tr$M$, a convenient observation for our setup. We denote the combination by $f_{\pi\mathrm{K}}$

$$f_{\pi\mathrm{K}} \equiv \frac{2}{3}\Big(f_{\mathrm{K}} + \frac{1}{2}f_{\pi}\Big) = f\Big[1 - \frac{7}{6}L_{\pi} - \frac{4}{3}L_{\mathrm{K}} - \frac{1}{2}L_{\eta} + \frac{16B\mathrm{tr}M}{3f^2}(L_5 + 3L_4)\Big]\,. \tag{5.55}$$

Along our trajectory tr$M = const$, the one-loop behavior of $f_{\pi\mathrm{K}}$ is entirely fixed by the linear combination of the logarithmic terms in eq. (5.55), up to a constant term, depending on one combination of LECs. Using the experimental values of the pion and kaon decay constant, after the subtraction of the isospin-breaking effects [104], we calculate the QCD value of $f_{\pi\mathrm{K}}$

$$f_{\pi} = 130.2(1.4)\,\mathrm{MeV}\,, \quad f_{\mathrm{K}} = 156.3(0.9)\,\mathrm{MeV}\,, \quad f_{\pi\mathrm{K}} = 147.60(76)\,\mathrm{MeV}\,. \tag{5.56}$$

In our calculations we fix the scale $\Lambda = 4\pi f_{\pi\mathrm{K}}$ and we introduce a simple notation, to describe the chiral dependencies

$$y_{\pi} = \frac{m_{\pi}^2}{(4\pi f_{\pi\mathrm{K}})^2}\,, \quad y_{\mathrm{K}} = \frac{m_{\mathrm{K}}^2}{(4\pi f_{\pi\mathrm{K}})^2}\,, \tag{5.57}$$

and

$$y_{\eta} = \frac{4}{3}y_{\mathrm{K}} - \frac{1}{3}y_{\pi} + O(y_{\pi}^2)\,. \tag{5.58}$$

Note that in the denominator of y_{π} and y_{K} we use the values of $f_{\pi\mathrm{K}}$ measured on each ensemble. Therefore replacing the pseudo-scalar masses with these two variables, is equivalent to changing the parameter of the chiral expansion from $(m_{\pi}/(4\pi f))^2 \to (m_{\pi}/(4\pi f_{\pi\mathrm{K}}))^2$. In the literature the two methods are usually called x and ξ expansions, referring to f and $f_{\pi\mathrm{K}}$ respectively. We note however, that this change of variable produces effects at higher orders than we consider here, namely $(m_{\pi}/f)^4$.

For later convenience let us still introduce two additional quantities

$$y_{\mathrm{sym}} \equiv y_{\pi}|_{\kappa_u=\kappa_d=\kappa_s}\,, \quad y_{\pi\mathrm{K}} \equiv \frac{1}{2}y_{\pi} + y_{\mathrm{K}}\,. \tag{5.59}$$

Using eq. (5.56) we compute the value of y_{π} and y_{K} in nature

$$y_{\pi}^{\mathrm{phys}} = 0.005282(59)\,, \quad y_{\mathrm{K}}^{\mathrm{phys}} = 0.07105(74)\,, \quad y_{\pi\mathrm{K}}^{\mathrm{phys}} = 0.07369(74)\,. \tag{5.60}$$

5.2.3 ChPT in Finite Volume

Chiral Perturbation theory can be also set in a finite spatial volume L, while the temporal direction is taken to be infinite here. If periodic boundary conditions are assumed in the spatial directions, Goldstone particles running in the loops of a pion two-point function, for instance, can also wrap around the spatial direction by crossing the boundary. This

effect translates into a shift of the pion mass in the propagator and, by turning the arguments around, it can be used to compute quantities in infinite volume $A(\infty)$, from those obtained at finite L, $A(L)$,

$$R_A = \frac{A(\infty) - A(L)}{A(L)}\,, \quad A = m_\pi, m_{\rm K}, f_\pi, f_{\rm K}\,. \tag{5.61}$$

For a degenerate number of flavors the calculation has been carried out in Ref. [127] to one-loop, while in full $SU(3)$ ChPT, the shifts for the pion and kaon masses have been derived in Ref. [128]

$$\begin{aligned} R_{m_\pi} &= \frac{1}{4}G_\pi - \frac{1}{12}G_\eta\,, \\ R_{m_K} &= \frac{1}{6}G_\eta\,. \end{aligned} \tag{5.62}$$

Similarly the decay constants in finite volume are "distorted" as well

$$\begin{aligned} R_{F_\pi} &= -G_\pi - \frac{1}{2}G_K\,, \\ R_{F_K} &= -\frac{3}{8}G_\pi - \frac{3}{4}G_K - \frac{3}{8}G_\eta\,. \end{aligned} \tag{5.63}$$

Once the loop-level is fixed, it is sufficient to count the number of times the particles cross the boundaries to estimate their effects. In principle, an infinite summation is implied but these contributions fall off exponentially with $\exp(-|\vec{n}|m_X L)$, X being the particle traveling in the loop and $\vec{n}$ the vector counting the times this particle has crossed the three spatial boundaries. Hence, restricting to only one wrapping of the particle "around the world", the core function appearing in the previous equations becomes

$$G_X = \frac{48 m_X^2}{(4\pi f_{\pi{\rm K}})^2}\sqrt{\frac{\pi}{2(m_X L)^3}}e^{-m_X L} + O(e^{-\sqrt{2}m_X L})\,, \tag{5.64}$$

with $X = \pi, K, \eta$.

An alternative method has been devised by Lüscher in Refs. [109, 110], where the finite-volume shifts in masses are related to scattering amplitudes with the lightest particles in infinite volume. For example, a shift in the pion mass is related to the $\pi\pi$ scattering amplitude. If on the other hand, one wants to use this prediction to correct the measurements from finite L to infinite volume, an assumption on the scattering amplitudes, coming again from ChPT, must be used. Using the leading order ChPT expression of the scattering amplitudes (and one wrapping) the Lüscher formula gives eqs. (5.64) and eqs. (5.62).

5.2.4 $SU(2)$ ChPT, WChPT

ChPT, the effective theory of QCD can be constructed by integrating out some of the original fields, corresponding to heavy particles. Looking at the spread of the experimental

values of the quark masses, one wonders whether the strange quark can still be considered light and added to the effective description of QCD. The relevant scale in hadron physics is given by $\Lambda_{QCD} \simeq 300\,\mathrm{MeV}$ and up/down quarks certainly satisfy the condition $m_{u,d} \simeq 4\,\mathrm{MeV} \ll \Lambda_{QCD}$[10], while for $m_\mathrm{s} \simeq 100\,\mathrm{MeV}$ some doubts remain. The same picture is mirrored in ChPT, where the meson masses have to be compared to a typical chiral scale Λ_χ such as $\Lambda_\chi = 4\pi f_\pi \simeq 1\,\mathrm{GeV}$. Nevertheless a considerable debate can be found in the literature on one side on the applicability of $SU(3)$ ChPT, and on the other on the range of validity of $SU(2)$ ChPT (see for example Refs. [129, 130, 131]).

The problem in computations involving more than the 2 light flavors, is how to treat the strange quark. Starting from the $SU(3)$ formulae given before, we might consider the strange mass heavy enough, such that $m_\mathrm{ud}/m_\mathrm{s} \ll 1$ and m_ud is the only small parameter used in the expansions. Along this line, all the terms proportional to m_s can be expanded in m_ud and be completely absorbed in both existing and new low-energy constants. The result is that the expansions of f_π and f_K depend on a different set of low-energy constants and consequently $f_{\pi\mathrm{K}}$, at one-loop, is a function of three combinations of these LECs, instead of two. For these reasons and given our chiral trajectories, as a first step we decided to use $SU(3)$ ChPT as a guideline in our extrapolations.

Note that an independent derivation of the same $SU(2)$ formulae, can be obtained by appropriately adding a kaon field to the $SU(2)$ chiral Lagrangian: this method is called Heavy Kaon ChPT and one loop results can be found in Ref. [132]. Another possible extension of ChPT consists in adding suitable terms to the Lagrangian, whose effects mimic the chiral symmetry breaking given by the Wilson discretization [133]. In this derivation known as Wilson ChPT, lattice artifacts appear in the chiral expansions and can be modeled accordingly. However, from the chiral Lagrangian at order p^4 with the a terms [134], one can see that these effects should appear at next-to-next-to-leading-order in the decay constants and for an $O(a)$-improved theory. Since in this thesis we consider only NLO expansions, we neglect these effects.

5.3 Systematic effects

All numerical computations are affected by systematic errors. Nowadays the precision of the calculations achieved by the lattice community has become rather good, for some observables reaching the percent accuracy in the continuum. Most of the systematic uncertainties come from the extrapolation to the physical point in the quark masses and to the continuum limit. Another source of possible errors is related to algorithms, as discussed in Chapter 3: are simulations long enough for a correct estimate of the autocorrelations? Is the field space properly sampled?
Apart from these questions, precision physics requires also to take into account effects,

[10] We are here naively assigning a value to masses and Λ parameter, neglecting the complications of scale and scheme dependencies of these quantities.

which so far have been neglected due to the dominance of the statistical errors. The most relevant is given by the finiteness of the lattices, which have a finite spatial extent L. A second, by possible mistunings in the quark masses, as now all computations are carried out with at least up, down and strange quark fields.

5.3.1 Finite Volume corrections

Among the quantities studied in this thesis, only the PCAC masses are not expected to be affected by finite volume effects. They are defined through an operator identity, which must be valid independently from L, apart from cutoff effects.

In general, all other observables, t_0, meson masses and decay constants, do depend on the spatial extent. The common method to quantify possible finite volume effects is through the ChPT formulae introduced before.

As we have seen chiral perturbation theory is dominated by two scales, the quark mass (or the pion mass) and the strength of the interactions, given by the momentum in units of the pseudo-scalar decay constants. Therefore, the ChPT predictions in finite volume, are valid in the limits

$$m_\pi L \gg 1 \quad \text{and} \quad f_\pi L \gg 1\,. \tag{5.65}$$

In the left panel of Figure 5.8 we present a scatter plot of our ensembles, in the plane described by the two variables in eq. (5.65).

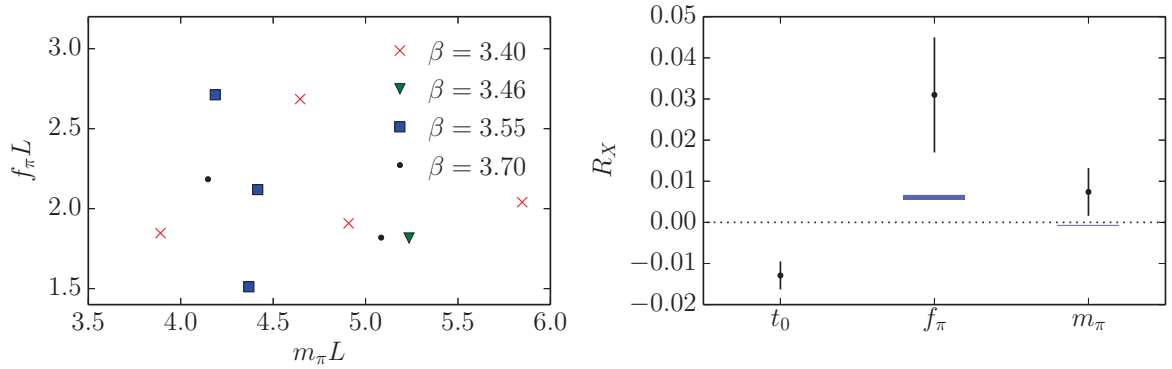

Figure 5.8: *Left*: scatter plot of the ensembles with constant tr$M$ in the plane $f_\pi L$ vs $m_\pi L$. The blue square point at the bottom of the figure corresponds to H200, which has $L \sim 2\,\text{fm}$. *Right*: Relative finite volume shifts, measured at $\beta = 3.4$ between $L \sim 2.7\,\text{fm}$ and $2\,\text{fm}$. The boxes show the ChPT predictions, eq. (5.62) and eq. (5.63), which underestimate the finite-volume corrections for the pseudo-scalar decay constant by two sigma.

Among all the points there is one evident outlier, H200, where the combination $m_\pi L$ satisfies the common lower bound of 4, but $f_\pi L$ is only 1.5 ($L \approx 2\,\mathrm{fm}$). For this point the corrections of finite-size effects from ChPT are, for example, $R_{f_\pi} \approx 1\%$ (eqs. (5.63)). To investigate this problem better, we decided to simulate a $L/a = 24$ ensemble at $\beta = 3.4$, thus corresponding to $L = 2\,\mathrm{fm}$. In the right panel of Figure 5.8 the relative corrections to the pion mass and decay constants are plotted, together with the ChPT predictions of eqs. (5.62) and eqs. (5.63). The latter underestimate the effect for f_π by a factor 2 or more. Direct simulations are important to reveal the effects.

Consequently the observables $X = t_0/a^2, am_\pi, am_\mathrm{K}, af_\pi$ and af_K have been corrected, under the assumption that the lattice artifacts of the corresponding shifts R_X are negligible,

$$\begin{aligned} R_X &= \frac{X(L = 2.7\,\mathrm{fm}, \beta = 3.4)}{X(L = 2\,\mathrm{fm}, \beta = 3.4)} - 1\,, \\ X(L = 2.7\,\mathrm{fm}, \beta = 3.55) &= X(L = 2\,\mathrm{fm}, \beta = 3.55)[1 + R_X]\,. \end{aligned} \tag{5.66}$$

Finally, using chiral perturbation theory, we apply the finite-volume corrections in eq. (5.62) and eq. (5.63), to the pion and kaon spectral quantities, for the ensembles with $m_\pi L \gtrsim 4$ and $f_\pi L \gtrsim 1.7$. In this case, the shifts turn out to be below the statistical accuracy for all points and we do not have to worry about inaccuracies of the ChPT prediction.

5.3.2 Mistunings

In Chapter 4 we have described the ensembles and the strategy used to choose the physical parameters. In the left panel of Figure 4.3 we have seen that, at the symmetric point where $\kappa_u = \kappa_d = \kappa_s$, the tuning of ϕ_4 to the target value 1.15, has been reached within 1%.

From previous studies [135] it emerges that the pion decay constant, from the chiral point to $m_\pi \approx 400\,\mathrm{MeV}$, varies (roughly) around 15-20%. Therefore, the effects of a mistuning at the symmetric point ($m_\pi = m_\mathrm{K} \approx 420\,\mathrm{MeV}$) on the percent level are expected to be about 0.1-0.2% in the chiral limit, hence well below our statistical uncertainties. To verify this expectation, we estimate the size of the corrections given by a mistuning in ϕ_4 at the symmetric point, by computing the derivatives of the observables under study w.r.t. ϕ_4. To this purpose we use the H40x series of ensembles, simulated at $\beta = 3.4$ and pion masses of 420, 450 and 550 MeV.

These ensembles, which have different values of $\mathrm{tr}M$, are not at constant lattice spacing because of chiral symmetry breaking effects (recall the discussion in Chapter 2). The difference between $\tilde{g}_0$ and g_0 amounts to $b_g a\mathrm{tr}M/N_\mathrm{f}$. To estimate the impact of the difference in the sum of the quark masses among the three H40x ensembles, we have used the 1-loop result [48] $b_g = 0.012 N_\mathrm{f} g_0^2 + O(g_0^4)$. The largest value of $a\mathrm{tr}M = 0.04165(8) + O(g_0^4)$ corresponds to the ensemble H401 and it is computed from the PCAC masses in

Table 5.1, using the one-loop result of $\tilde{Z}$ (see eq. (5.39)), $r_m = 1 + O(g_0^4)$ and eq. (5.73). For this ensemble we obtain

$$\text{H401}: \quad \frac{\tilde{g}_0^2}{g_0^2} = \frac{\beta}{\tilde{\beta}} = 1 + 9 \cdot 10^{-4} + O(g_0^4) \quad \to \frac{a(\beta)}{a(\tilde{\beta})} \approx 0.994\,. \tag{5.67}$$

In our estimates of the derivatives we will ignore these corrections, since their size, once translated in a relative change of the lattice spacing[11], is still relatively small compared to the statistical errors.

In Figure 5.9 (right panel) we plot the dependence of t_0 and f_π on ϕ_4. To estimate their derivatives we simply consider the difference between the two closest points on the left (index 1 corresponds to H400 and 2 to H402),

$$\frac{1}{A(\phi_4^1)} \frac{A(\phi_4^1) - A(\phi_4^2)}{\phi_4^1 - \phi_4^2} \approx \frac{\partial \log A}{\partial \phi_4} + O\Big(\frac{1}{2A}\frac{\partial^2 A}{\partial^2 \phi_4}\Big)\,, \tag{5.68}$$

and we use the third point, which has twice as large quark masses, to check for possible systematic errors. Our results for t_0 and f_π are

$$\frac{\partial \log f_\pi}{\partial \phi_4} = 0.24(5)\,, \quad \frac{\partial \log t_0}{\partial \phi_4} = -0.09(3)\,. \tag{5.69}$$

The shifts in ϕ_4 defined at the symmetric point, are common to all points belonging to a chiral trajectory (fixed g_0). In Table 5.2 we report our numerical results for the relative corrections due to mistunings in ϕ_4

$$\delta_{\phi_4}(A, \beta) = \frac{\partial \log A}{\partial \phi_4}(\phi_4^{\rm sym}(\beta) - 1.15)\,, \tag{5.70}$$

for our four lattice spacings. The shifts, for all observables, are below the statistical accuracy of our data points by at least a factor 2. The only point suffering from a significant correction is H400, where $\delta_{\phi_4}(f_{\pi\rm K}, 3.46) \approx 0.6\sigma_{f_{\pi\rm K}}$. From the data at $\phi_4 \approx 2$ we estimate the impact of a quadratic term on the derivative computed at the symmetric point by a fit. Given the size and the precision of the shifts in Table 5.2, this is a negligible effect.

In Figure 5.9 we show how the quantity $\sqrt{8t_0} f_{\pi\rm K}$, at the symmetric point ($m_\pi = m_{\rm K} \approx 420\,\text{MeV}$), changes after the finite-volume and mistuning corrections. The most relevant shift is given by the finite volume effect at $\beta = 3.55$, as described before. Without the leftmost point in the right panel of Figure 5.9 and before the several corrections, one might be lead to believe that there are no visible a^2 effects, as demonstrated by the fact

[11] To translate the shift in β into a shift of the lattice spacing we have fitted the ratio $R(\beta) = \sqrt{t_0(3.4)/t_0(\beta)} = a(\beta)/a(3.4)$ using the the three-loop β-function, with b_0 and b_1 fixed to their universal values.

	$\delta_{\phi_4}(A,\beta)$ [%]			
A	$\beta = 3.4$	$\beta = 3.46$	$\beta = 3.55$	$\beta = 3.7$
f_π	0.2(2)	-0.4(2)	-0.0(3)	-0.1(2)
t_0	-0.08(6)	0.15(8)	0.0(1)	0.05(7)
$\sqrt{8t_0}f_{\pi\mathrm{K}}$	0.2(1)	-0.3(2)	-0.0(3)	-0.1(2)
y_π	0.4(3)	-0.8(4)	-0.1(7)	-0.2(3)

Table 5.2: Results of the relative shifts δ_{ϕ_4}, eq. (5.70), for various observables A. Note that all the numbers in the table are percent relative shifts. The derivatives of $\sqrt{8t_0}f_{\pi\mathrm{K}}$ and y_π are linear combinations of those in eq. (5.69).

that a constant fit (which is only illustrative) describes the three coarsest points very well. However the presence of the ensemble at $\beta = 3.7$ is fundamental, as it reveals the size of the a^2 violations and raises the suspect on possible systematic effects at $\beta = 3.55$, which we correct.

5.4 Discretization effects

To avoid renormalization factors and reduce the number of free parameters, our renormalization condition has been defined through the quantity ϕ_4 at the symmetric point. Towards the chiral limit the sum of the bare subtracted quark masses has been kept fixed. From eq. (2.28) we know that up to $O(a)$ effects and the multiplicative Z_m factor, it corresponds to the renormalized $\mathrm{tr}M$. Hence, having $\mathrm{tr}M_{\mathrm{R}}$ not constant is a consequence of lattice artifacts and we investigate now this effect.

Let us start by considering the expansion of $\mathrm{tr}M^2$ appearing in eq. (2.28), where we replace bare subtracted quark masses with the corresponding bare PCAC masses m_{rs} using eq. (5.37), ($N_{\mathrm{f}} = 3$)

$$\frac{a\mathrm{tr}M^2}{\mathrm{tr}M} = -4\tilde{Z}r_m am_{12} + \Big[\frac{2r_m^2+1}{3}\Big]a\mathrm{tr}M + \frac{6\tilde{Z}^2 am_{12}^2}{\mathrm{tr}M} + O(a^2)\,. \tag{5.71}$$

Note that we have kept, when possible, the dependence on $\mathrm{tr}M$ explicit. The reason is clearly related to possible simplifications in the formulae due to the choice of the chiral trajectory, $\mathrm{tr}M = const.$ Plugging eq. (5.71) inside eq. (2.28) gives, up to higher orders which we drop,

$$\mathrm{tr}M_{\mathrm{R}} = Z_m r_m \mathrm{tr}M\Big[1 + \big(\bar{d}_m + \frac{2r_m^2+1}{3}d_m\big)a\mathrm{tr}M - 4\tilde{Z}r_m d_m am_{12} + \frac{6\tilde{Z}^2 d_m am_{12}^2}{\mathrm{tr}M}\Big]\,. \tag{5.72}$$

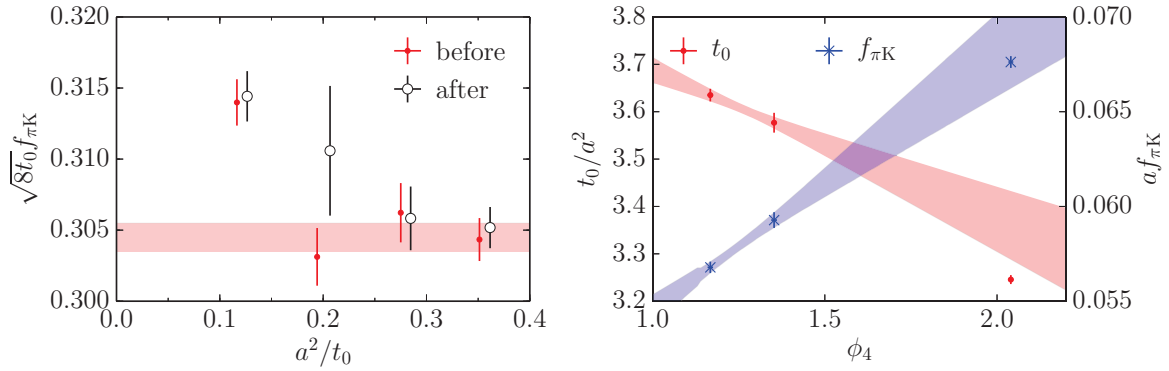

Figure 5.9: *Left*: $\sqrt{8t_0}f_{\pi K}$ at $m_{ud} = m_s$ before and after finite-volume and mistuning corrections. The shaded area represents a constant fit excluding the finest lattice. We show it, for illustrative purpose, to underline the importance of simulations at fine lattice spacings. Finite-volume corrections are essential in changing the point at $\beta = 3.55$. A linear a^2 behavior is now visible. *Right*: dependence of t_0 and $f_{\pi K}$ on ϕ_4. The data points correspond to the ensembles H40x. Shaded areas represent the derivatives computed at $\phi_4 = 1.15$. The points at twice as large quark masses, $\phi_4 \approx 2$, can not be used in the estimate of the derivatives as they seem to show some curvature.

A consequence of eq. (5.37) for our setup is that

$$\begin{aligned} \mathrm{tr}M = \frac{\tilde{Z}}{r_m}(m_{12}+2m_{13})(1+O(am_{12})) = \frac{\tilde{Z}}{r_m}3m_{\mathrm{sym}}(1+O(am_{12}))\,, \\ m_{\mathrm{sym}} \equiv m_{12}|_{\kappa_u=\kappa_d=\kappa_s} = m_{13}|_{\kappa_u=\kappa_d=\kappa_s}\,, \end{aligned} \tag{5.73}$$

where the last substitution ($m_{12}+2m_{13} \to 3m_{\mathrm{sym}}$) holds again up to $O(a)$ effects. In fact, also the sum of the renormalized PCAC masses is, in principle, not constant due to $\bar{b}_A - \bar{b}_P$ and $b_A - b_P$ terms in eq. (5.36). In this case, we obtain (always by replacing $m_{\mathrm{q},rs} \to m_{rs}$ but keeping $\mathrm{tr}M$ explicit)

$$\begin{aligned} m_{12,\mathrm{R}}+2m_{13,\mathrm{R}} = \frac{Z_A}{Z_P}(m_{12}+2m_{13})\Big\{1+\Big[(\bar{b}_A-\bar{b}_P)-(b_A-b_P)\frac{r_m-1}{N_f}\Big]a\mathrm{tr}M \\ +(\tilde{b}_A-\tilde{b}_P)am_{\mathrm{sym}}\Big[1+\frac{1}{2}\Big(1-\frac{m_{12}}{m_{\mathrm{sym}}}\Big)^2\Big]\Big\}\,, \end{aligned} \tag{5.74}$$

where we have used eq. (5.73) in the denominator of the term proportional to $\tilde{b}_A - \tilde{b}_P$. At this point, we have all the ingredients to investigate the deviations from the $\mathrm{tr}M_{\mathrm{R}} = const$ trajectory. To profit from cancellations from the fact that the trace of the bare mass

matrix is constant, it is convenient considering the following ratios

$$\frac{m_{12,\mathrm{R}} + 2m_{13,\mathrm{R}}}{3m_{\mathrm{sym,R}}} = \frac{\mathrm{tr}M_{\mathrm{R}}}{\mathrm{tr}M_{\mathrm{R,sym}}} + O(a^2)\,. \tag{5.75}$$

The l.h.s. can be evaluated using the expansion in eq. (5.74) where only the term proportional to $\tilde{b}_A - \tilde{b}_P$ contributes. The r.h.s., on the other hand, is obtained by replacing $\mathrm{tr}M$ with m_{sym}, according to eq. (5.73), in the denominator of the last term of eq. (5.72)

$$\begin{aligned}\mathrm{tr}M_{\mathrm{R}} = Z_m r_m \mathrm{tr}M\Big\{1 + \big(\bar{d}_m + \frac{2r_m^2+1}{3} d_m\big) a\mathrm{tr}M \\ + 2\tilde{Z} r_m d_m a m_{\mathrm{sym}} \Big[\Big(\frac{m_{12}}{m_{\mathrm{sym}}} - 1\Big)^2 - 1\Big]\Big\}\,.\end{aligned} \tag{5.76}$$

Therefore by isolating the am terms on one side, from eq. (5.75) we finally obtain

$$\frac{m_{12} + 2m_{13}}{3m_{\mathrm{sym}}} = 1 + \underbrace{\Big[2\tilde{Z} r_m d_m - \frac{(\tilde{b}_A - \tilde{b}_P)}{2}\Big]}_{b_R} a m_{\mathrm{sym}} \Big(\frac{m_{12}}{m_{\mathrm{sym}}} - 1\Big)^2 + O(a^2)\,. \tag{5.77}$$

From the measured values of the ratio on the l.h.s., plotted in Figure 5.10, it is possible to determine non-perturbatively b_R appearing in eq. (5.77).

However, let us stress that Figure 5.10 must be interpreted in the correct way: the limit where the up/down quark mass vanishes is at $(m_{12}/m_{\mathrm{sym}} - 1)^2 = 1$, while the origin corresponds to $m_{12} = m_{\mathrm{sym}}$ where the quark masses are all large. Moreover, by construction, the functional form in eq. (5.77) is forced to cross 1 at the origin and consequently fitting the data points with it, automatically implies its validity close to the symmetric point. As shown in the figure, this is not a good assumption at $\beta = 3.4$, where a fit of the function given in eq. (5.77) does not describe the data very well and returns large values of the product $\tilde{Z} r_m d_m$, beyond expectations. In fact, with only two degrees of freedom, we obtain $b_R \simeq -10.5(9)$, with $\chi^2 \simeq 9.6$ and a Q-value approximately 0.01. Compared to Ref. [119], where the combination $\tilde{Z} r_m$ has been computed for the two-flavor theory in a similar range of lattice spacings, this estimate of $\tilde{Z} r_m d_m$ is clearly too large and unreliable.

Consequently, we interpret this fact as the presence of discretization errors beyond the $O(am)$ corrections, which spoil the validity of eq. (5.77) at least for this value of β. For example there may be a term $a^2(m_{12} - m_{\mathrm{sym}})$ which will curve up steeply near $m_{12} = m_{\mathrm{sym}}$ in the plot. For our finer lattice spacings the situation looks already different, since the ratios of PCAC masses depend linearly on $(m_{12}/m_{\mathrm{sym}} - 1)^2$, symmetric point included. Hence, eq. (5.77) can be fitted through all points at $\beta = 3.55$ thus giving $b_R \simeq -3.2(1.1)$.

Beyond these considerations on $O(a)$-improvement, what is relevant for the chiral extrapolations of the decay constants, is the 5% relative difference of $\mathrm{tr}M_{\mathrm{R}}$ between the

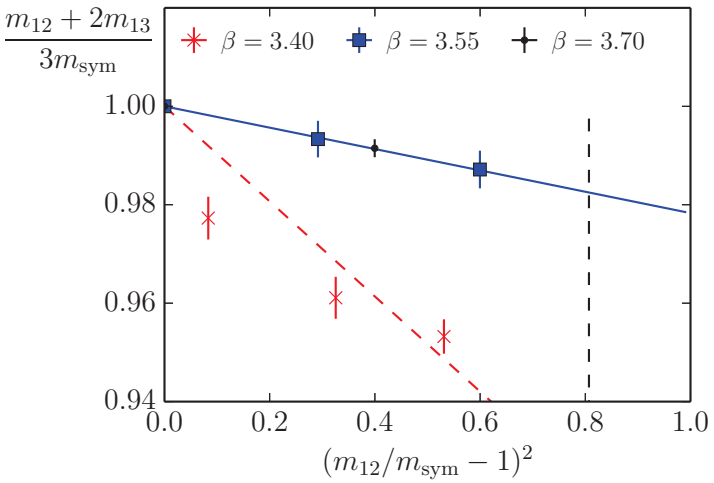

Figure 5.10: Ratio of the sum of bare PCAC masses over $3m_{\rm sym}$. The solid line represents a fit to the points at $\beta = 3.55$ of the form $f(x) = 1 - 0.022(8) \cdot x$, with $x = (m_{12}/m_{\rm sym} - 1)^2$. The dashed line is the result of the same fit, performed on the data points at $\beta = 3.4$, whose slope turns out to be $-0.096(8)$. The vertical line corresponds to physical quark masses, where the ratio $m_{\rm s}/m_{\rm ud}$ is 27.46(43) [104].

symmetric and the physical point at $\beta = 3.4$, which goes down to less than 2% for $\beta \geq 3.55$. In Figure 5.11 we plot the the pseudo-scalar decay constants normalized at the symmetric point. Given the accuracy of the measurements, discretization effects in the slope of $f_{\pi \rm K}$ w.r.t. the pion mass squared are not observed. Note that the values of the ratio at $\beta = 3.55$ exhibit large errors (almost 2%) simply because they are divided by $f_{\pi \rm K}$ at the symmetric point, which has been corrected for finite volume effects at the price of a loss in precision. Therefore the non-observation of cutoff effects in the slope of the ratio plotted in Figure 5.11 is not enough to exclude their presence. Indeed, this is not the case for t_0, which, being so precise, shows lattice artifacts in the ratio $t_0/t_0^{\rm sym}$. From the left panel of Figure 5.12 differences are visible on the 2-3% level. We remind the reader that t_0 is a dimension 2 quantity, so this translates into 1-1.5% effect in a scale.

A second source of systematic effects is t_0, since different discretizations of the smooth energy density lead to different cutoff effects in t_0. In Ref. [8] the plaquette action eq. (2.4) and the clover definition of the $F_{\mu\nu}$ tensor [46] have been studied numerically, and, relatively to r_0, the clover definition exhibits a milder dependence on a^2. In Figure 5.12 we plot the ratio of the two definitions, measured at $m_\pi = m_{\rm K} \approx 420\,\text{MeV}$. The ratio, profiting from the correlation between numerator and denominator, is extremely precise and clearly shows scaling violations beyond the leading a^2. Also for this quantity the importance of the finest lattice is evident: without the point at $\beta = 3.7$, the systematic

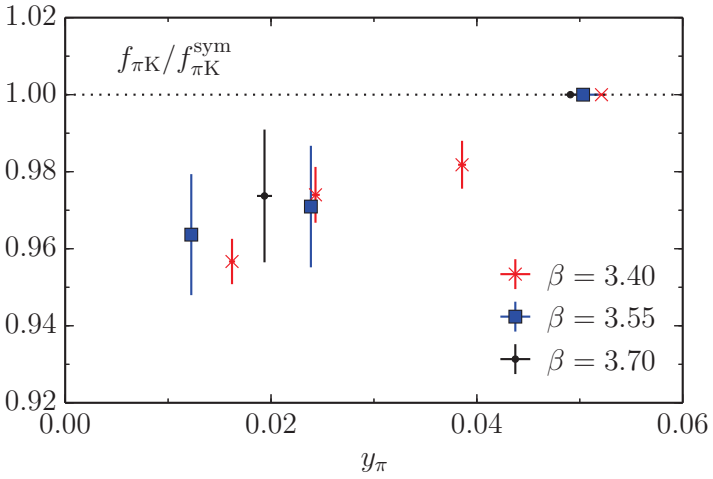

Figure 5.11: Ratio of the pseudo-scalar decay constants $f_{\pi K}$ normalized at the symmetric point.

error in the continuum limit would be about 2%.

The CLS tuning strategy, described in Chapter 4, is based on t_0. In the ϕ_4 vs. ϕ_2 plane[12], see Figure 5.13, we do not observe significant discretization effects, mostly because the lattices at different cutoffs have been matched through these variables. Therefore, to estimate the relation between ϕ_4 and ϕ_2 we have fitted the data with the linear function

$$f(\phi_2) = 1.15 + B(\phi_2 - 0.7667)\,, \quad B = 0.07(1)\,. \tag{5.78}$$

The result is plotted in the right panel of Figure 5.13 and, as we can see from the plot, the data extrapolate to the physical point, calculated using our determination of t_0, described in the next Chapter. Note that thanks to the corrections for mistunings in ϕ_4, Figure 5.13 shows a better scaling than Figure 4.3.

It is more convenient to re-express the mass combinations in ϕ_2 and ϕ_4 in terms of $f_{\pi K}$ for two reasons: on the one hand its value in physical units is known (from experiments) and on the other it is the natural parameter in ChPT (using t_0 would introduce another constant). The two variables y_π and y_K provide an alternative way to check the size of discretization effects for our chiral trajectories. In Figure 5.13 we plot the combination $y_{\pi K} = \frac{1}{2}y_\pi + y_K$, which is proportional to $\mathrm{tr}M$ to leading order in ChPT, as a function of y_π. Unlike t_0, their QCD-value is known, see eq. (5.60), and scaling violations, along the y-axis, are clearly visible on the level of 8%. The latter are essentially due to the relative cutoff effects between t_0 and $f_{\pi K}$. On top of this, however, we know that there

[12] In Figure 5.13 we have included the corrections discussed in Section 5.3. Figure 4.3 (right panel), presented in Chapter 4, refers to the un-corrected, raw data, listed in Table 5.1.

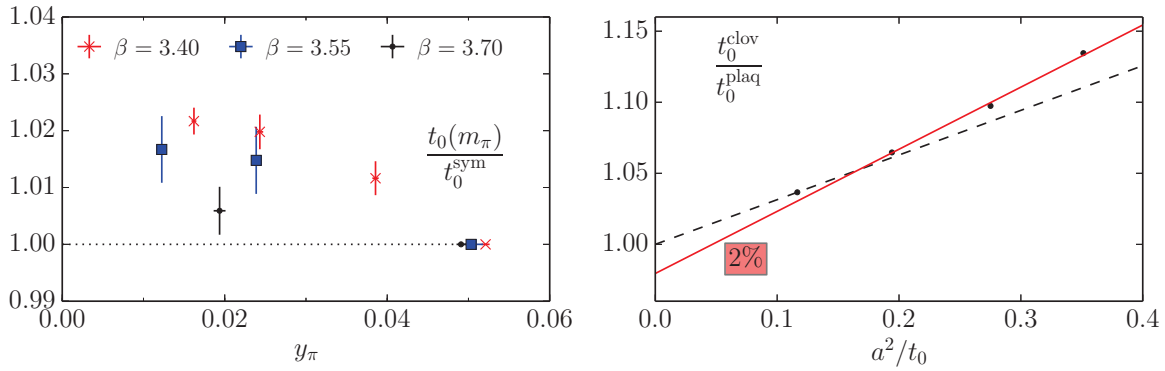

Figure 5.12: *Left*: ratio of the measured values of t_0 over $t_0^{\rm sym}$. The dependence of the three slopes on the lattice spacings is the sign of lattice artifacts of order a, which are visible within 2-3 standard deviations. *Right*: ratio of two values of t_0 computed with the clover and plaquette definitions (updated w.r.t. Ref. [12]). Profiting from correlations, the ratios turn out be extremely precise and reveal scaling violations beyond a^2. The dashed line is a fit involving the finest lattice and constrained to 1 in the continuum limit. The red solid line is fit through the points at $\beta \leq 3.55$, which does not extrapolate to 1 in the limit $a \to 0$. The importance of the ensembles at $\beta = 3.7$ is now evident.

are $O(a)$ ambiguities along our chiral trajectories. The ChPT expressions of the decay constants, and consequently our chiral extrapolations, depend on these two variables and we need to have their cutoff effects under control for a correct estimate of the systematic uncertainties. As a first attempt, we try now to parametrize them through a global fit.

From ChPT, the predicted continuum behavior of $y_{\pi\rm K}$ is (see eq. (5.52))

$$y_{\pi\rm K} \propto {\rm tr}M_{\rm R}(1 + B_0 y_\pi) + O(y^2)\,, \tag{5.79}$$

with B_0 a coefficient related to the ChPT low-energy constants. Along our chiral trajectories we know that the equation ${\rm tr}M_{\rm R} = const$ is violated by $O(a)$ terms. Therefore, to model these effects we start by replacing in eq. (5.77) all the quark masses with their corresponding y variables and we plug this result in eq. (5.79). Since we know that the coefficient b_R depends on g_0, through its one-loop expansion we make this dependence explicit also in eq. (5.79), thus obtaining

$$\begin{gathered} y_{\pi\rm K} = \left(A_0 + A_1\frac{a^2}{t_0}\right)\left[1 + B_0 y_\pi + B_1(g_0)\frac{a}{\sqrt{t_0}}\left(y_\pi - y_{\rm sym}\right)^2\right], \\ B_1(g_0) = B_1(1 + 0.0423 g_0^2)\,. \end{gathered} \tag{5.80}$$

We perform several fits to our measured values of $y_{\pi\rm K}$ by imposing $B_i = 0$ in eq. (5.80) in different ways. The results of these fits are reported in Table 5.3.

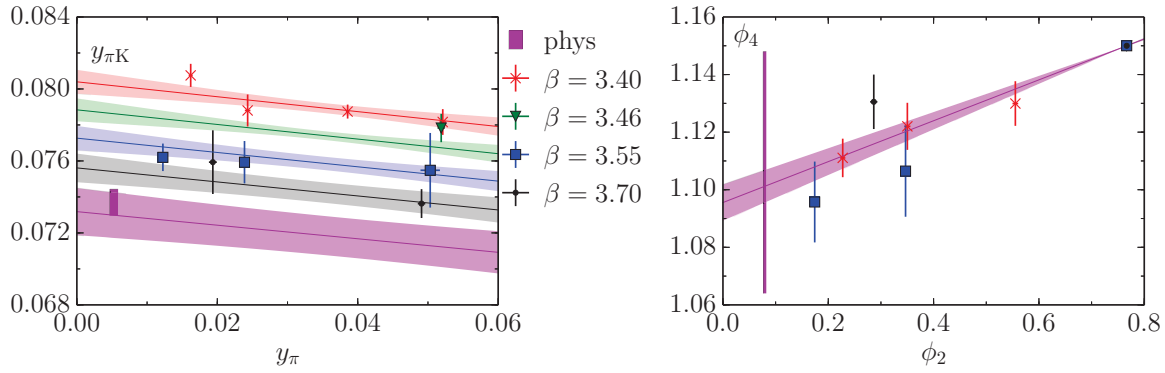

Figure 5.13: *Left*: $\frac{1}{2}y_\pi + y_K$ as a function of the pion mass in units of $f_{\pi K}$. The lines, together with their corresponding error bands, come from a global fit to eq. (5.80), with $B_1 = 0$, see Table 5.3. The extrapolations at $\beta = 3.4$ reveal approximately 8-9% discrepancy with the continuum value, represented by the magenta square. *Right*: scatter plot of the ϕ_4 and ϕ_2 variables after being corrected as described in Section 5.3. Cutoff effects are not visible given the precision of the data. The shaded area represent the result of the fit in eq. (5.78). The physical point value is based on our determination of $\sqrt{8t_0}$ in fm, see next Chapter.

In all cases, the extrapolations hit the physical point in the continuum limit within one standard deviation, thus confirming that the choice $\phi_4 = 1.15$ was a reasonable choice. Unfortunately, the statistical accuracy of our measurements does not allow to fit the function in eq. (5.80) with both B_0 and B_1 as free parameters, as they turn out to be undetermined. Indeed, as we evince from Table 5.3 it is not possible to distinguish a physical dependence on y_π from a cutoff effect, which we know is present. Therefore we opt for a different strategy consisting in changing the renormalization conditions and afterwards we proceed with the computation of the lattice spacing.

A_0	A_1	B_0	B_1	$\chi^2/\chi^2_{\rm exp}$	Q-value
0.0717(28)	0.027(10)	0.4(1.5)	-1.75(2.7)	6.1/5.6	0.36
0.0724(11)	0.0245(45)	—	-1.0(0.5)	6.5/6.6	0.41
0.0732(13)	0.0213(42)	-0.5(0.3)	—	6.8/6.6	0.38

Table 5.3: Results of various fit to $y_{\pi\rm K}$ using eq. (5.80). We used different combinations of the coefficients parametrizing the dependence on the pion mass, by setting some of them to zero. As we see from the errors on the B_i parameters, if we leave both unconstrained they are completely undetermined. The χ^2 and Q-value do not allow us to discriminate among the three fitting options. We remind the reader that the location of the physical point is $y^{\rm phys}_{\pi\rm K} = 0.0737(7)$, see eq. (5.60).

6 Scale setting

In this Chapter we present the main strategy used to compute the lattice spacing from the pseudo-scalar decay constants and t_0. Throughout this Chapter we will denote functions with capital letters and variables, or measured values, with lowercase letters, e.g. $Y_{\rm K}(y_\pi)$ is a function of the variable y_π while $y_{\rm K}$ denotes the measurement[1].

6.1 Renormalization conditions

Let us start with the description of the renormalization condition on the strange quark mass that we impose to cancel the order a lattice artifacts present along our chiral trajectories. As usual we translate the dependence on quark masses into y variables. The natural renormalization condition that we impose for all values of the light quark masses and β are

$$y_{\pi\rm K} \stackrel{!}{=} y_{\pi\rm K}^{\rm phys}\,, \quad \text{with} \quad y_{\pi\rm K} = \frac{1}{2}y_\pi + y_{\rm K}\,, \tag{6.1}$$

since it is proportional to tr$M$ in leading order ChPT. Eq. (6.1) defines a line of constant physics (LCP) in the y_π-$y_{\rm K}$ plane, which we denote with $Y_{\rm K}(y_\pi)$, thus removing the dependence on $y_{\rm K}$

$$Y_{\rm K}(y_\pi) = y_{\pi\rm K}^{\rm phys} - \frac{1}{2}y_\pi\,. \tag{6.2}$$

Our measured values of $f_{\pi\rm K}$ and t_0, which are on a somewhat different trajectory, need to be shifted to the one in eq. (6.1). Assuming that both observables are smooth functions of the quark masses, we can compute their new values by Taylor expanding to first order, meaning that the first derivatives of $f_{\pi\rm K}$ and t_0 w.r.t. to y_π and $y_{\rm K}$ are needed.

Eq. (6.2) is certainly not the optimal choice from the point of view of the absolute shifts. In fact one might find curves in the y_π-$y_{\rm K}$ plane which minimize more the distance from the points. The real advantage of eq. (6.1) is that $\tilde{g}_0$ remains fixed in the limit $m_\pi \to 0$. This condition would not be possible for a line with a slope different from the one in eq. (6.2), for example.

[1]Similarly we adopt the notation $F_{\pi\rm K}$ to indicate a function, not to be confused with the two normalizations of the decay constant in the chiral limit, used in the literature. In the thesis we always use the $f_\pi \approx 130\,\text{MeV}$.

6.1.1 Mass derivatives

To estimate the first derivative of a function $f(x)$ from two points we use the formula

$$\frac{1}{f(x_0)}\frac{f(x_0)-f(x_1)}{x_0-x_1} = \frac{\partial}{\partial x}\log f\Big|_{x_0} + O(x_1-x_0)\,. \tag{6.3}$$

Since we will determine the derivative for one lattice spacing and use it on all ensembles, we adopt the $1/f(x_0)$ normalization to get rid of possible conversion factors between different values of β, which in the limit of small step-sizes $(x_0 - x_1)$ corresponds to the derivative of $\log f$.

For the mass derivatives we can exploit two options with the set of ensembles that we have generated. The first one consists in using the measurements at $m_{\rm s} = const$ and $\beta = 3.4$, where the derivatives can be estimated at fixed y_π. More precisely, the ensembles C102 and C101 have been simulated at the same pion mass in units of $f_{\pi\rm K}$ (within one sigma the two ensembles have the same y_π and an additional interpolation is not needed) and their difference gives the smallest step-size in $y_{\rm K}$ for the derivative.

Unfortunately, from C102 and C101 the derivative turns out to be poorly estimated, since the measurements are relatively close to each other and the statistical accuracy is not sufficient to resolve their difference

$$\text{C102}\,,\text{C101}\quad \frac{\partial}{\partial y_{\rm K}}\log f_{\pi\rm K}(y_\pi, y_{\rm K}) = 5.6(4.7)\,, \frac{\partial}{\partial y_{\rm K}}\log t_0(y_\pi, y_{\rm K}) = -3.2(1.3)\,. \tag{6.4}$$

The second possibility is given by the H40x series of ensembles, which have a good statistics and are exactly on the symmetric line $y_\pi = y_{\rm K}$ (also in this case additional interpolations are not needed). Note that we have already performed a similar calculation to estimate the derivatives of t_0 and $f_{\pi\rm K}$ w.r.t. ϕ_4 in Chapter 5.

The three ensembles that we use here are spread on a relatively wide range of pion masses starting at $m_\pi \approx 420\,\text{MeV}$ up to 550 MeV. To give a safer estimate of the derivatives we use only the two closest points, see Figure 6.1. In this way the systematic uncertainties associated with the higher order terms in the Taylor expansion of eq. (6.3) are small and we obtain the derivatives with a 50% accuracy

$$\text{H400}\,,\text{H402}\quad \frac{d}{dy_\pi}\log f_{\pi\rm K}(y_\pi, y_\pi) = 10.4(4.7)\,, \quad \frac{d}{dy_\pi}\log t_0(y_\pi, y_\pi) = -3.8(1.3)\,. \tag{6.5}$$

In Chapter 5 we have already discussed the influence of chiral symmetry breaking effects due to the change in tr$M$ among the three H40x ensembles. Applying the same reasoning also here, we conclude that these effects are negligible, given the precision of the derivatives that we compute.

Since no additional ensembles are available at the moment within the CLS effort, we have to make an assumption on the dependence of the derivatives on the pion mass, to be able to apply them to all other points. We will comment on this later.

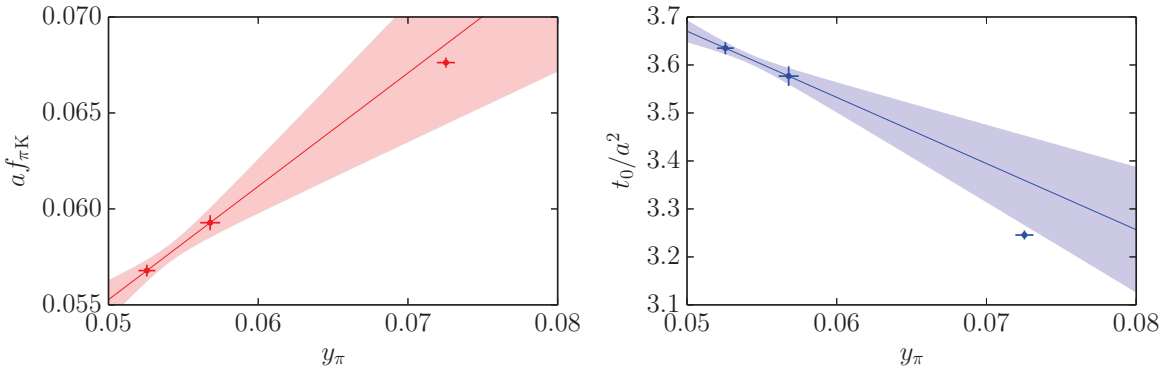

Figure 6.1: Plot of $af_{\pi K}$ and t_0/a^2 as a function of the pion mass. The lines are forced to cross the left-most point and their slope is given by the derivatives in eq. (6.5). The shaded areas show the corresponding error bands. Had we used all three available points, we would have obtained the derivatives with an accuracy about 10%. To really improve our estimate an additional point at smaller y_π, say $y_\pi \approx 0.049$ would be needed.

6.1.2 New chiral trajectory

Between the two options described above, we decide to take eq. (6.5). The reasons for this choice are the better precision on the one hand, and the smaller size of the shifts on the other. From the left panel of Figure 6.2 we see that, between the measured points and the target line $Y_K(y_\pi)$, the lines parallel to $y_\pi = y_K$ describe paths in the y_π-y_K plane shorter than the vertical shifts at $y_\pi = const.$

Having decided to use the derivatives computed in eq. (6.5) for all our ensembles, we have to shift our data points along a line parallel to $y_K = y_\pi$ until we hit the line of constant physics defined in eq. (6.2). Starting from the measured values of y_π and y_K, which we denote with superscript 0, we define the line parallel to the symmetric one and passing through this point with $Y'_K(y_\pi) = y_K^0 + (y_\pi - y_\pi^0)$. Its intersection with $Y_K(y_\pi)$

$$\begin{cases} Y'_K(y_\pi) = & y_K^0 - y_\pi^0 + y_\pi \\ Y_K(y_\pi) = & y_{\pi K}^{\text{phys}} - \frac{1}{2} y_\pi \end{cases} \quad \rightarrow \quad y_\pi^1 = \frac{2}{3}(y_{\pi K}^{\text{phys}} + y_\pi^0 - y_K^0) \tag{6.6}$$

defines the new point in the y_π-y_K plane (superscript 1) where the measured values of $f_{\pi K}$ have to be moved to. To first order in y, the new values of the pseudo-scalar decay constants can be obtained using the derivative computed along the symmetric line

$$af_{\pi K}(y_\pi^1, Y_K(y_\pi^1)) = af_{\pi K}(y_\pi^0, y_K^0)\left[1 + \frac{d}{dy_\pi} \log f_{\pi K} \cdot \Delta + O(\Delta^2)\right], \tag{6.7}$$

with

$$\Delta = \frac{2}{3}(y_{\pi K}^{\text{phys}} - \frac{1}{2} y_\pi^0 - y_K^0)\,. \tag{6.8}$$

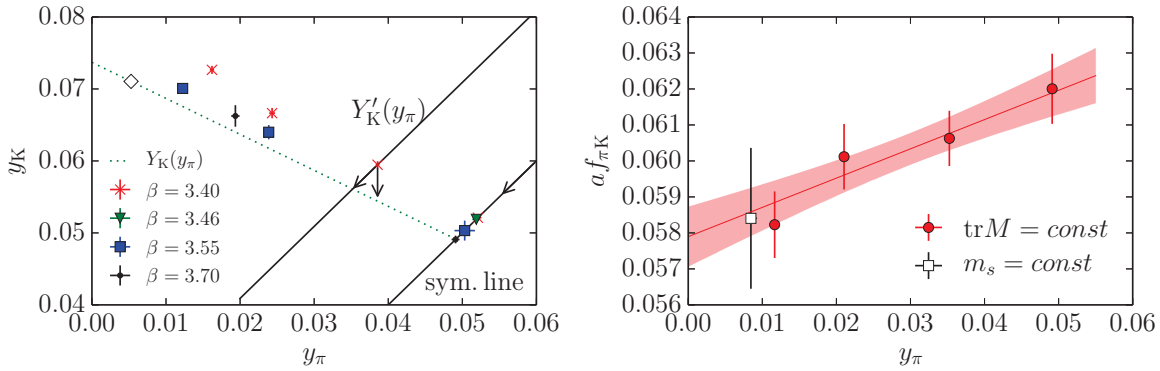

Figure 6.2: *Left*: scatter plot of the ensembles in the y_π-y_K plane. Starting from the measured points we move $f_{\pi K}$ along the symmetric lines passing through these points ($Y'_K(y_\pi)$), ending up on $Y_K(y_\pi)$. The diamond represents the physical point. *Right*: plot of the values of $af_{\pi K}$ shifted to the trajectory defined by eq. (6.1). The filled symbols correspond to the tr$M$ = *const* case, while the open one to the point shifted from m_s = *const*. The shaded curve is the result from the linear fit, performed in the next Section. All the points seem to fall on a universal curve.

The results of this calculation are reported in Table 6.1, with the values of the same quantities before applying the shifts.

Before continuing with the analysis, let us comment on the assumption that $\frac{d}{dy_K} \log f_{\pi K}$ does not depend on y_π. The ensembles at m_s = *const* can be used to show such a depedence: by shifting their values of $f_{\pi K}$ to the line $Y_K(y_\pi)$ according to eq. (6.6), we can check if they describe a universal curve with the other data points at $\beta = 3.4$. As we can see from the right panel of Figure 6.2 it seems to be the case at the level of precision that we can reach.

In principle, ChPT provides us with a second check on this assumption. Starting from the chiral expansion of the pseudo-scalar decay constants in eq. (5.55) and replacing the quark masses with y_π and y_K, we obtain the following expression (we use the superscript χ to denote that it is a prediction from ChPT)

$$F^\chi_{\pi K}(y_\pi, y_K) = f(1 + \bar{L}(y_\pi, y_K) + b y_{\pi K}) \,, \quad b = \frac{8(4\pi)^2}{3}(L_5 + 3L_4) \,, \tag{6.9}$$

with $\bar{L}$ summarizing the logarithmic contributions

$$\bar{L}(y_\pi, y_K) = -\frac{7}{6} y_\pi \log(y_\pi) - \frac{4}{3} y_K \log(y_K) - \frac{1}{2} y_\eta(y_\pi, y_K) \log(y_\eta(y_\pi, y_K)) \,. \tag{6.10}$$

To compute the dependence of the derivative in eq. (6.5) on m_π, we have to evaluate the previous expression along the line parallel to $y_\pi = y_K$ and passing through one of our

ensembles $(y_\pi^0, y_{\rm K}^0)$, namely along $Y'_{\rm K}(y_\pi)$. Schematically the steps are

$$F^\chi_{\pi{\rm K}}(y_\pi, Y'_{\rm K}(y_\pi)) \quad \to \quad \frac{d}{dy_\pi} F^\chi_{\pi{\rm K}}(y_\pi, Y'_{\rm K}(y_\pi)) \quad \to \quad \frac{1}{F^\chi_{\pi{\rm K}}} \frac{d}{dy_\pi} F^\chi_{\pi{\rm K}}(y_\pi, Y'_{\rm K}(y_\pi))\,, \tag{6.11}$$

where the last quantity,

$$\frac{d}{dy_\pi} \log F^\chi_{\pi{\rm K}}(y_\pi, Y'_{\rm K}(y_\pi)) = \frac{\frac{d}{dy_\pi}\bar{L}(y_\pi, Y'_{\rm K}(y_\pi)) + \frac{3}{2}b}{1 + \bar{L}(y_\pi, Y'_{\rm K}(y_\pi)) + b(\frac{1}{2}y_\pi + Y'_{\rm K}(y_\pi))} \tag{6.12}$$

if evaluated with the values of y_π and $y_{\rm K}$ measured on our ensembles (recall that $Y'_{\rm K}$ still depends on y_π^0 and $y_{\rm K}^0$), can be used to monitor the dependence of the derivative on the pion mass. The latter still depends on the parameter b which is expected to be $b \approx 0.4$, from previous lattice determinations of the low-energy constants taken from the FLAG report [104]. Hence, we can use this value of b to check if ChPT matches our non-perturbative calculation of the derivative or alternatively we can compute b directly by using the value in eq. (6.5) on the l.h.s. of eq. (6.12).

In Figure 6.3 we plot the derivative predicted from ChPT in eq. (6.12) for two values of the kaon mass corresponding to the smallest and largest ones in our simulations. We also vary the parameter b, which is still present in the derivative, from 0.4, the aforementioned "expected value", to $b = 12$ which is the solution we obtained by solving eq. (6.12). From Figure 6.3 we learn that the dependence of the derivative on the pion mass is relatively mild compared to the statistical accuracy of our determination. In particular, the parameter b has a very small influence on the dependence on y_π, but it basically controls the absolute normalization of the derivative. The value that we exctract by solving eq. (6.12) is practically undetermined since the error of the derivative in eq. (6.5) is large (50%). Nevertheless we observe some tension between the ChPT expectations, combined with FLAG estimates of LECs, and our measurements.

A second possibility to use ChPT on our data is to fit directly the measurements $af_{\pi{\rm K}}$ with eq. (6.9). From a first attempt we obtain a relatively good χ^2 but a negative value of b in disagreement with the previous findings. Since the set of points at ${\rm tr}M = const$ shows little sensitivity to the linear term in $y_{\pi{\rm K}}$, we add to the fit also the points at $m_{\rm s} = const$ and H402, the ensemble along the symmetric line with $m_\pi \approx 450\,{\rm MeV}$. Eventhough the parameter b is now in rough agreement with the expectations from the derivatives, the statistical description of the data is not satisfactory as $\chi^2/{\rm dof} \simeq 5$. Taking into account that the χ^2 is based on the error of the observables, we interpret this result as the fact that the NLO $SU(3)$ ChPT is not able to describe our measurements on their level of accuracy, which is about 1%, but only on the 2-3% level.

Certainly, the results shown in Figure 6.3 and Figure 6.2 confirm that, to this level of accuracy, the derivatives in eq. (6.5) can be safely applied to all our points.

Once the shifts are implemented, the question on the size of cutoff effects naturally arises. Therefore in Figure 6.4 we show the ratio of pseudo-scalar decay constants and t_0

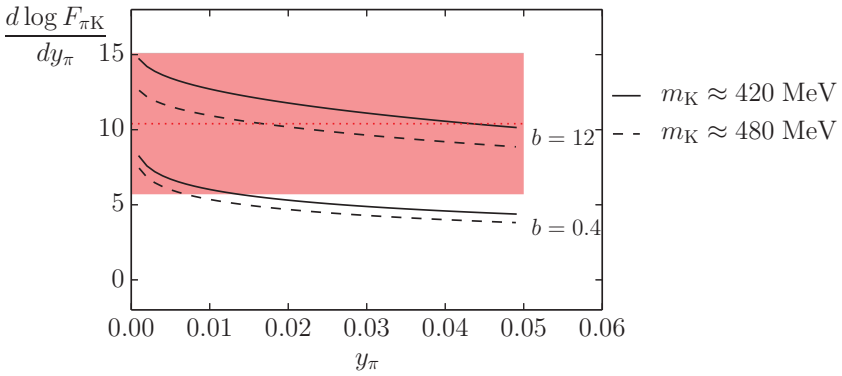

Figure 6.3: Taking the values of the low-energy constants appearing in eq. (6.9) from the FLAG report [104], $L_5 \simeq 10^{-3}$ and $L_4 \simeq 0$, we obtain $b \simeq 0.4$. From our non-perturbative estimate of the derivative we are not able to extract this coefficient. However, we notice that using the value taken from the literature, the derivative from ChPT is underestimated only by 1.5 sigma.

over their respective values at y_π^{sym}. In both cases the corrections decrease the precision of the measurements because of the error of the derivatives. However, thanks to the condition in eq. (6.1), it is possible to estimate the behavior of both quantities in ChPT. At next-to-leading order the low-energy constants drop out in the ratios and the curves are completely determined in terms of logarithms for $f_{\pi K}$ and a simple horizontal line for t_0 (see Ref. [136] and next Section)

$$\begin{aligned} \frac{F^\chi_{\pi K}(y_\pi, Y'_K(y_\pi))}{F^\chi_{\pi K}(y_\pi^{\text{sym}}, Y'_K(y_\pi^{\text{sym}}))} &= 1 + \bar{L}(y_\pi, Y'_K(y_\pi)) - \bar{L}(y_\pi^{\text{sym}}, Y'_K(y_\pi^{\text{sym}})) + O(y^2)\,, \\ \frac{t_0(y_\pi)}{t_0(y_\pi^{\text{sym}})} &= 1 + O(y^2)\,. \end{aligned} \tag{6.13}$$

For the pseudo-scalar decay constants we do not observe a particular change w.r.t. the un-shifted situation in Figure 5.11, mostly because the errors of the ratio at $\beta = 3.55$ are dominated by the finite-volume corrections described in Chapter 5. Instead, for t_0 the effect of the new renormalization condition is more evident, in particular for the point at $\beta = 3.7$. Before the shifts, cutoff effects were visible on the 2-3% level, whereas now the points fall on the same line within one standard deviation.

Apart from cutoff effects, from the plots in Figure 6.4 we learn that NLO $SU(3)$ ChPT does not seem to provide a satisfactory description of our measurements (in agreement with what we said before). In more quantitative terms, the χ^2 of the ChPT prediction of the ratio of $f_{\pi K}$ in eq. (6.13) is $\chi^2/\chi^2_{\text{exp}} \simeq 2$. Note that we account for the correlations

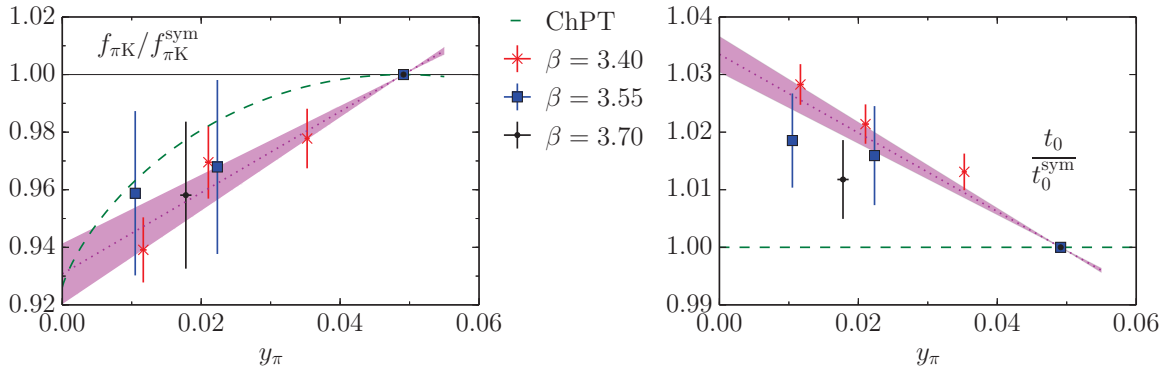

Figure 6.4: Plots of $f_{\pi K}$ and t_0 normalized at the symmetric point. Thanks to the renormalization condition $y_{\pi K} = const$, the NLO ChPT curves are now determined up to a^2 violations without the need of low-energy constants. For both observables the points do not seem to follow the ($SU(3)$) ChPT predictions, but to prefer a linear behavior in y_π. The latter is represented by the dotted lines, which are fits with only the slope as a free parameter. From the error band we can already guess that the lattice spacing can be exctrated from the linear fit with a 1.5-2% accuracy.

among the data points, introduced by the derivatives, by computing the effective number of degrees of freedom χ^2_{exp}, introduced in Chapter 5. Most of the contributions to the χ^2 come from the points at $\beta = 3.4$ which show a 2% discrepancy from the ChPT curve. For these points we are able to keep a good precision also after shifting to our LCP, but additional improvements to reduce the errors at $\beta = 3.55$ are possible and we describe them later.

For t_0 the discrepancy between the NLO $SU(3)$ ChPT and our measurements is more evident. The (shifted) points are more precise and a significant deviation (in particular at $\beta = 3.4$) from a flat behavior is observed. In both cases, our measurements taken along the line of constant $y_{\pi K}$ exhibit a clean linear behavior in the light quark mass. From linear fits to the ratios plotted in Figure 6.4 we obtain

$$\begin{aligned} \frac{f_{\pi K}}{f_{\pi K}^{sym}}(y_\pi) &= 1 + A y_\pi \,, \quad A = 1.4(4) \,, \\ \frac{t_0}{t_0^{sym}}(y_\pi) &= 1 + B y_\pi \,, \quad B = -0.70(11) \,, \end{aligned} \tag{6.14}$$

with good reduced χ^2 ($\chi^2/\chi^2_{exp} \leq 0.9$). Hence, in the rest of the analysis we will perform linear chiral extrapolations both for $f_{\pi K}$ and t_0, with the coefficients parametrizing the dependence on y_π independent of the lattice spacing.

ID	β	y_π^0	y_K^0	$y_{\pi\mathrm{K}}^0$	$af_{\pi\mathrm{K}}(y_\pi^0, y_\mathrm{K}^0)$	y_π^1	y_K^1	$af_{\pi\mathrm{K}}(y_\pi^1, y_\mathrm{K}^1)$
H101	3.40	0.05188(47)	0.05188(47)	0.07782(71)	0.06383(32)	0.04913(49)	0.04913(49)	0.06200(97)
H102		0.03839(23)	0.05921(48)	0.07840(32)	0.06267(22)	0.03525(37)	0.05606(36)	0.06063(77)
H105		0.02422(39)	0.06635(70)	0.07846(86)	0.06217(33)	0.02103(49)	0.06317(39)	0.06012(91)
C101		0.01614(28)	0.07233(53)	0.08040(61)	0.06107(24)	0.01166(48)	0.06786(39)	0.05823(93)
H106		0.02240(64)	0.0798(11)	0.0910(12)	0.06331(55)	0.01087(95)	0.06826(48)	0.0557(31)
H107		0.03508(36)	0.07830(67)	0.09584(82)	0.06760(31)	0.02032(56)	0.06353(28)	0.0572(40)
C102		0.01531(57)	0.0763(10)	0.0840(12)	0.06288(46)	0.00846(81)	0.06946(40)	0.0584(20)
H400	3.46	0.05232(56)	0.05232(56)	0.07847(85)	0.05691(31)	0.04913(49)	0.04913(49)	0.0550(12)
H200	3.55	0.0504(14)	0.0504(14)	0.0756(21)	0.04874(70)	0.04913(49)	0.04913(49)	0.0481(14)
N200		0.02392(35)	0.06411(90)	0.0761(11)	0.04733(25)	0.02233(59)	0.06253(52)	0.04654(70)
D200		0.01228(15)	0.07021(54)	0.07635(59)	0.04697(20)	0.01051(60)	0.06844(52)	0.04611(55)
N300	3.70	0.04921(61)	0.04921(61)	0.07381(92)	0.03799(22)	0.04913(49)	0.04913(49)	0.03796(49)
J303		0.01941(56)	0.0664(15)	0.0761(18)	0.03699(41)	0.01779(81)	0.06479(59)	0.03637(89)

Table 6.1: Values of the measured pion and kaon masses squared in units of $f_{\pi\mathrm{K}}$, together with their combination $y_{\pi\mathrm{K}}$. Note that finite-volume corrections have been applied, as discussed in the previous Chapter. For this reason the error of the ensemble H200 is larger compared to others. The superscripts 0 and 1 refer to the original measurements and to those shifted to the line of constant physics. Clearly we do not have a column for $y_{\pi\mathrm{K}}^1$.

6.2 Lattice spacing determination

Finally, before presenting the strategy adopted to compute the lattice spacing, we summarize the most relevant choices that we have taken so far:

- to account for finite-volume effects on the ensemble H200 we have performed a simulation at a coarser lattice spacing but with the same physical extent and we used it to correct the observables of H200. The price we pay is a loss of precision for this point;
- to keep the chiral behavior sufficiently constant, we use the combination of pion and kaon decay constants $f_{\pi\mathrm{K}}$;
- to remove the $O(a)$ lattice artifacts along our chiral trajectories, we imposed a new renormalization condition, given in eq. (6.1). Also in this case the error of our measurements increases.

Now the procedure is pretty standard. Firstly, we fit our measured values of $af_{\pi\mathrm{K}}$ with a few functional forms $F_{\pi\mathrm{K}}(\beta, y_\pi)$, which model the chiral behavior. Secondly we evaluate these functions at the physical pion mass and the lattice spacing is obtained according to

$$a(\beta)[\,\mathrm{fm}] = \frac{F_{\pi\mathrm{K}}(\beta, y_\pi^{\mathrm{phys}})}{f_{\pi\mathrm{K}}^{\mathrm{phys}}[\,\mathrm{fm}^{-1}]}\,. \tag{6.15}$$

Following the discussion in the previous Section, we formulate the following ansatz on the chiral dependence of $f_{\pi\mathrm{K}}$

$$\text{Fit A}: \quad F_{\pi\mathrm{K}}(\beta, y_\pi) = f_A(\beta)(1 + l_A y_\pi)\,, \tag{6.16}$$

which consits in a simple Taylor expansion in the quark masses, where the depedence on y_{K} is now completely fixed. The results of this fit are plotted in Figure 6.5. To quantify the systematic uncertainties from the truncation of the expansion, we fit our data also with a quadratic function in y_π

$$\text{Fit B}: \quad F_{\pi\mathrm{K}}(\beta, y_\pi) = f_B(\beta)(1 + l_B y_\pi + q_B y_\pi^2)\,. \tag{6.17}$$

Note that in each extrapolation, the coefficients l_X (and q_X) are the same for all values of β, thus leading to global fits to all our points. This assumption is correct up to terms of order $a^2 y_\pi$, which we do not see according to the left panel of Figure 6.4, and are parametrically small.

The original measurements of $f_{\pi\mathrm{K}}$ (corrected only for finite-volume effects and mistunings in ϕ_4, labeled with the superscript 0 in Table 6.1) can be used as well to extract the lattice spacing. The problem in this case is the presence of $O(a)$ lattice artifacts in

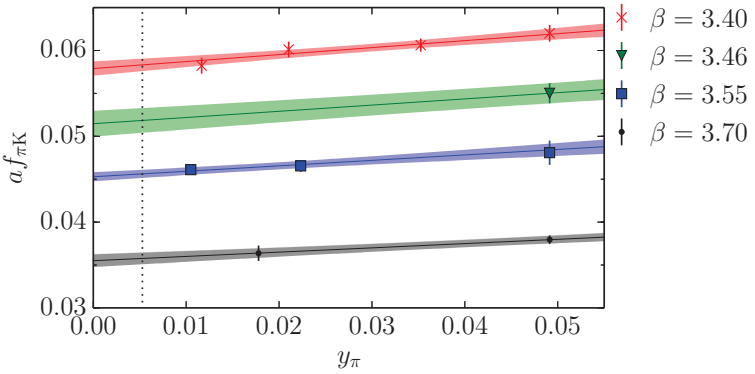

Figure 6.5: Linear fit (Fit A) performed on the set of data shifted to the LCP, $y_{\pi K} = y_{\pi K}^{\text{phys}}$, where order a effects have been corrected non-perturbatively.

the trace of the renormalized quark mass matrix, which is not constant. Choice A can consequently be generalized to the full y_π-y_K plane to

$$\text{Fit C}: \quad F_{\pi K}(\beta, y_\pi, y_K) = f_C(\beta)(1 + l_C y_\pi + q_C y_K)\,. \tag{6.18}$$

We report the lattice spacings computed from the different fits in Table 6.2 and we plot them also in Figure 6.6. We note immediately a discrepancy between the results obtained from the shifted and un-shifted values of $f_{\pi K}$. The former are free from $O(a)$ lattice artifacts and the differences of the pseudo-scalar decay constants at the physical point between the two sets of data is a cutoff effect, which disappears in the limit $a \to 0$. For this reason we do not use the values of the lattice spacing obtained with $O(a)$ ambiguities in our estimates of the systematic uncertainties.

Hence, restricting ourselves only to the points fulfilling eq. (6.1), we quote as our final estimates of the lattice spacings the results obtained from the quadratic fit eq. (6.16), which have a larger statistical error and cover the tiny differences with the results from the linear fit.

6.3 Future improvements

Before continuing with the determination of t_0 let us propose some possible (future) improvements to this thesis, which could improve the error of the lattice spacings down to 1%.

- An additional simulation at $\beta = 3.46$ and $y_\pi \approx 0.048 - 0.049$ would certainly improve the determination of the derivatives in eq. (6.5). It would not be expensive as a lattice with $L/a = 32$ would be sufficient and quark masses would be relatively

	a [fm]					
Fit	$\beta = 3.4$	$\beta = 3.46$	$\beta = 3.55$	$\beta = 3.7$	$\chi^2/\chi^2_{\rm exp}$	Q-value
A	0.0780(19)	0.0693(27)	0.06099(94)	0.0478(11)	1.1/2.7	0.88
B	0.0779(21)	0.0693(27)	0.0610(12)	0.0478(11)	1.0/2.2	0.83
C	0.0841(21)	0.0746(19)	0.06313(85)	0.04910(71)	0.40	0.90

Table 6.2: Values of the lattice spacings for our four values of β obtained from the chiral extrapolations of $af_{\pi\rm K}$. The first two rows correspond to fits performed to the shifted data, fulfilling the renormalization condition $y_{\pi\rm K} = y^{\rm phys}_{\pi\rm K}$, while the last one to the unshifted measurements. The naive number of degrees of freedom is 5 and 4, for the two choices respectively. The effects of correlations among the points are evident from the comparison with the value of $\chi^2_{\rm exp}$. We remind the reader that choice A and B correspond to linear and quadratic fits in y_π, while choice C to a linear fit in y_π and $y_{\rm K}$. The χ^2 are particularly small. We quote the results of Fit B as our final estimates of the lattice spacing.

large (around 30 MeV each). With a higher statistical accuracy of the derivative, say 10%, the errors of the shifted $f_{\pi\rm K}$ would remain about 1%.

- Having the possibility to measure these derivatives directly on the ensembles would free us from the assumption that they do not depend on the pion mass: this is certainly the most relevant one in our computation and with the available ensembles (and ChPT) we have demonstrated that it holds. Nevertheless if in the future a higher accuracy of the derivative will be achieved, this assumption will become more problematic and the only solution will be a direct measurement on every ensemble. Mass reweighting or a direct evaluation of the derivative w.r.t. tr$M$ are viable solutions.

- A second chiral trajectory with tr$M$ fixed to another constant for one β could help in resolving (and correcting) the $O(a)$ lattice artifacts present in tr$M_{\rm R}$. The optimal value of the coupling would be at $\beta = 3.55$, where simulations are not yet extremely expensive.

- Having a direct simulation of a lattice with $L = 2.7$ fm ($L/a = 48$) at $\beta = 3.55$ would decrease the error of the measurements at the symmetric point by at least a factor $1/\sqrt{3}$ (recall the discussion in Chapter 5 on finite-volume corrections). Consequently the chiral extrapolations would be more precise and stable.

- In general adding ensembles at small pion masses would reduce the systematic uncertainties of the chiral extrapolations and would provide a more reliable ground

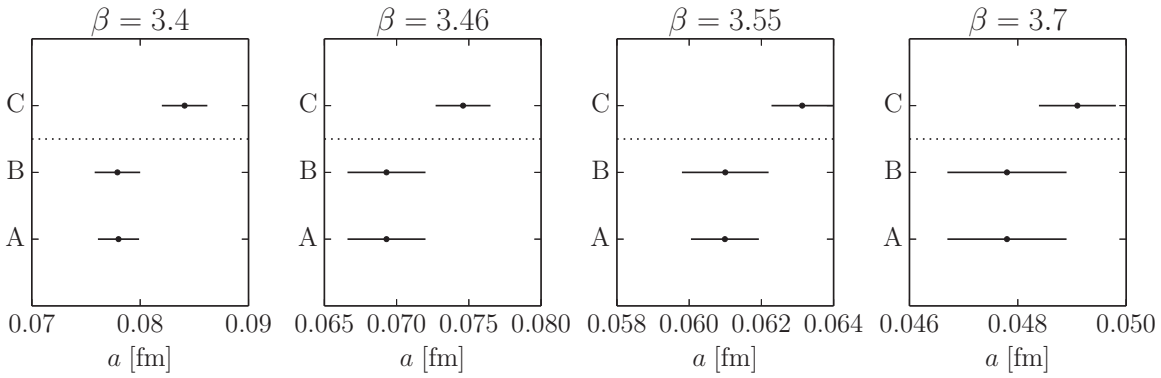

Figure 6.6: The results of the lattice spacings computed from the chiral extrapolations of the pseudo-scalar decay constants. The choices concerning the fit functions are: A linear, B quadratic, C linear to un-shifted data. The horizontal dotted line separates the fit performed on the original measurements (above) and those shifted to the LCP (below). The differences between the two sets of data are cutoff effects which vanish towards the continuum limit (left to right) as the figures indicate.

to test ChPT. In our case, the statistical accuracy of the extrapolations is large enough to incorporate also the differences among the various fits. However, if the target precision for the lattice spacing is 1%, these differences suddenly become important and need to be systematically studied. Moreover, further clarifications on the validity of $SU(3)$ ChPT would be possible: with a couple of ensembles at small pion masses, below 200 MeV or so, we would be able to allow cuts on the fit ranges and check if in the limit $m_\pi \to 0$ $SU(2)$ ChPT gives a better description of the data (remember that our simulations are a bit peculiar, from this point of view, since in the limit $m_\pi \to 0$ kaons become heavier and $SU(3)$ ChPT is consequently disfavored). $\beta = 3.46$ would be an ideal value of the coupling for such simulations, because physical pion masses could be reached with $L/a = 48$ and $L/a = 64$ lattices[2].

- Increasing the statistics and the number of points along the the trajectory $m_\mathrm{s} = const$ could be a second method to probe $SU(2)$ against $SU(3)$ ChPT. Indeed, one has to be careful in using the appropriate expansion, since the aforementioned Heavy Kaon ChPT is not optimal for our simulations at $\mathrm{tr}M = const$, but suitable for the trajectories at $m_\mathrm{s} = const$. With only three points, all at the same (coarse) lattice spacing, we have not been able to perform additional tests in this direction.

[2]Note that the requirements on the spatial extent of the lattices come from the inequality $m_\pi L \gtrsim 4$.

6.4 Flow scales

In this last Section we describe the computation of t_0 in the continuum limit, where we use $f_{\pi\mathrm{K}}$ as a reference scale. As underlined many times, this "artificial" quantity can be computed only through numerical simulations, as it is not accessible to experiments, and we use two approaches. The first one, based on the analysis that we developed in the two-flavor theory in Ref. [137], consists in extrapolating t_0/a^2 to the physical point and use the previous determination of the lattice spacing. In the second one we compute the quantity $\sqrt{8t_0}f_{\pi\mathrm{K}}$ and we perform a combined (global) fit.

The same procedure that we used to shift the pseudo-scalar decay constants to $y_{\pi\mathrm{K}} = y_{\pi\mathrm{K}}^{\mathrm{phys}}$ is applied also to t_0, using the derivative in eq. (6.5). From Figure 6.4 it is evident that t_0 has a (leading) linear dependence on the pion mass squared, on the level of a few percent accuracy. Assuming the slope independent from β, we fit the data using

$$T_0(\beta, y_\pi) = t_0^{\mathrm{chir}}(\beta)\Big[1 + k_1 y_\pi + k_2 y_\pi^2\Big]\,, \tag{6.19}$$

where we fix k_2 to zero in one case.

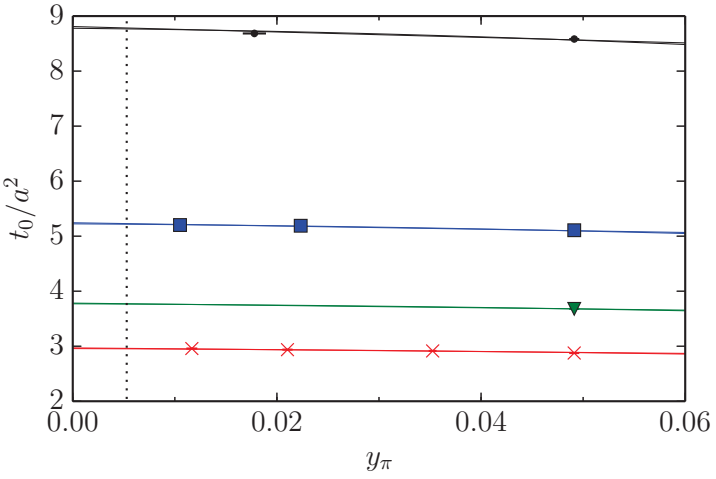

Figure 6.7: Plot of the chiral extrapolations of the measurements of t_0/a^2, fulfilling the renormalization condition in eq. (6.1).

We have already mentioned that a ChPT prediction for this quantity exists as well. More precisely, in Ref. [136] ChPT has been developed also for "flow observables". Below we report the $SU(3)$ chiral expansion up to next-to-leading order (in the formula below we use $\tilde{k}_1$ to distinguish it from the coefficient k_1 in eq. (6.19))

$$t_0 \propto 1 + \tilde{k}_1 y_{\pi\mathrm{K}} + O(y_\pi^2) + O(y_{\mathrm{K}}^2)\,. \tag{6.20}$$

$t_0^{\rm chir}(\beta)$							
$\beta = 3.4$	$\beta = 3.46$	$\beta = 3.55$	$\beta = 3.7$	k_1	k_2	$\chi^2/\chi^2_{\rm exp}$	Q-value
2.970(20)	3.783(39)	5.244(22)	8.810(54)	-0.56(10)	—	2.1/2.2	0.50
2.957(24)	3.771(41)	5.224(31)	8.778(62)	-0.21(41)	-5.8(7.0)	1.9/1.9	0.44

Table 6.3: Results of the fits to t_0/a^2 using eq. (6.19). The quality of both fits is good. The number of degrees of freedom is 5 and 4 for the linear and quadratic fits respectively. The presence of correlations among the points, introduced by the derivative, effectively reduces the d.o.f. to about 2. The data points do not seem to be sensitive to a quadratic term.

Along the line of constant physics, $Y_{\rm K}(y_\pi)$, eq. (6.20) is constant (up to and including linear terms in y_π) as stated in eq. (6.13). Therefore, the functional form that we provided in eq. (6.19) already incorporates part of the chiral behavior at NNLO, which we do not write explicitly, since more low-energy constants would appear (together with the usual logarithmic terms). From results of the fits to eq. (6.19), reported in Table 6.3, we see that the quadratic coefficient k_2 is undetermined. Hence it is hopeless to fit the full NNLO $SU(3)$ ChPT prediction to our points.

The values of $t_0^{\rm chir}(\beta)$ are spread within one sigma and no significant deviations are observed among the various choices that we considered. Therefore, we quote again the results of the quadratic fit, which incorporates the little systematic uncertainties given by the truncation in the linear fit

$$\begin{aligned} T_0(3.4, y_\pi^{\rm phys}) &= 2.953(20)\,, \quad T_0(3.46, y_\pi^{\rm phys}) = 3.766(38)\,, \\ T_0(3.55, y_\pi^{\rm phys}) &= 5.217(23)\,, \quad T_0(3.7, y_\pi^{\rm phys}) = 8.767(52)\,. \end{aligned} \tag{6.21}$$

Now, we continue with the description of the second approach and we discuss the extrapolations to the continuum limit of the two methods together. Thanks to the absence of logarithms in the NLO chiral expansion of t_0, we can re-use the same functional forms that we introduced to compute the lattice spacing from $f_{\pi\rm K}$ (previous Section). The only difference is a redefinition of the parameter proportional to $y_{\pi\rm K}$. Along the lines of what has already been discussed, we use the results of t_0 and $f_{\pi\rm K}$ satisfying $y_{\pi\rm K} = y_{\pi\rm K}^{\rm phys}$ to compute the quantity $\sqrt{8t_0}f_{\pi\rm K}$.

To perform a combined extrapolation to the chiral and continuum limit, we modify Fit A in eq. (6.16) according to

$$\Big(c_0 + c_1 T_0^{-1}(\beta, y_\pi^{\rm phys})\Big)\Big(1 + h y_\pi\Big)\,. \tag{6.22}$$

In a similar way, also choice B can be extended from $f_{\pi\rm K}$ to $\sqrt{8t_0}f_{\pi\rm K}$. We do not write the corresponding equation to avoid to introduce too many parameters and constants. Instead

Fit	$\sqrt{8t_0}$ [fm]	t_0 [fm^2]	$\chi^2/\chi^2_{\rm exp}$	Q-value
A	0.4135(60)	0.02137(62)	1.2/3.9	0.98
B	0.4124(67)	0.02126(69)	1.3/3.3	0.96
	0.4122(78)	0.02124(80)	0.17/0.48	0.65

Table 6.4: The first two rows list the results of the combined chiral and continuum fits to $\sqrt{8t_0}f_{\pi\rm K}$. The data is extremely correlated, as we can see by comparing the values of $\chi^2_{\rm exp}$ with the number of degrees of freedom 10 and 9, for Fit A and B respectively. The data points are not sensitive to the quadratic term which is undetermined from the fit. The last row corresponds to the continuum extrapolation of $T_0(\beta, y_\pi^{\rm phys})$ using the values of the lattice spacings calculated in the previous Section. We quote these numbers as our final estimates. χ^2 and Q-value refer only to the extrapolation in a^2, which has 2 degrees of freedom. We quote as our final results the values with largest statistical error.

in Table 6.4 we list the results of $\sqrt{8t_0}$ and t_0 in physical units, while in Figure 6.8 we plot the result of the quadratic fit (corresponding to Fit B).

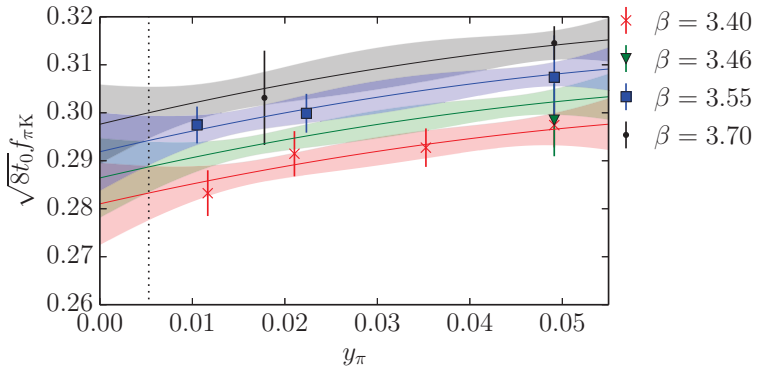

Figure 6.8: Plot of the chiral extrapolation of $\sqrt{8t_0}f_{\pi\rm K}$ with a quadratic function in y_π.

Finally, in Figure 6.9 we show the convergence, in the continuum limit, of the different extrapolations, including the first approach, where we extrapolated t_0/a^2 to physical quark masses and we multiplied it with the lattice spacing. The latter method produces larger statistical uncertainties in the continuum limit, which safely cover the discrepancies with the other two fits. Therefore we quote this result for our definitive estimate of the flow observable t_0 and we do not add additional systematic errors

$$\sqrt{8t_0} = 0.4122(78)\,\text{fm}\,, \quad t_0 = 0.02124(80)\,\text{fm}^2\,. \tag{6.23}$$

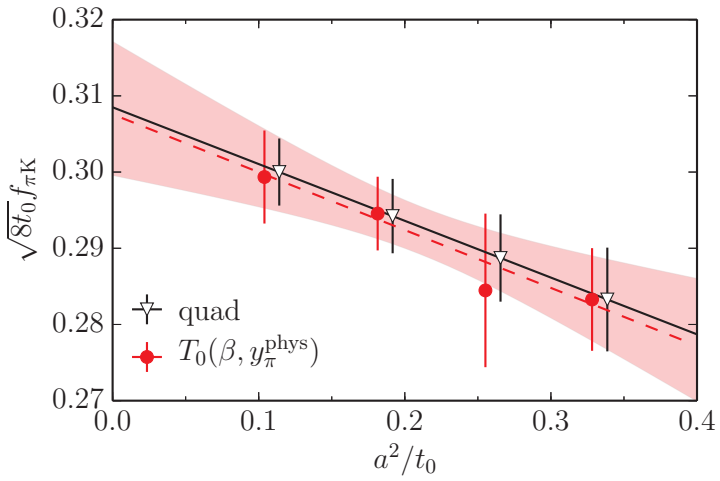

Figure 6.9: Continuum extrapolation of $\sqrt{8t_0}f_{\pi K}$. The open triangles are the result of the combined (chiral+continuum) quadratic fit, while the filled circles correspond to the case where chiral and continuum extrapolations are separate. In the latter case, the continuum extrapolation with a linear fit in a^2 is shown together with its error band, represented by the shaded area. In the continuum limit $\sqrt{8t_0}$ is obtained with 1.9% precision.

To obtain t_0 in fm^2 we have used the physical value of $f_{\pi K}$ reported in eq. (5.56), where isospin breaking effects have been removed. Our determination of t_0 for QCD with $2+1$ flavors is compatible with the value present in the literature, $\sqrt{8t_0} = 0.4144(70)$ fm, obtained by the BMW collaboration [75]. The precision, around 1.9%, is similar.

The improvements that we listed at the end of the previous Section, if pursued will affect also the determination of t_0, since its error is dominated by the precision of the reference scale $f_{\pi K}$. Nevertheless, our computation of t_0 demonstrates that the set of ensembles analyzed in this thesis allows the determination of observables in the continuum limit with (at least) a few percent accuracy, in terms of the reference scale that we have studied.

7 Conclusions

In this thesis we have computed a reference scale for a new set of ensembles generated within the CLS effort over the last two years. Open boundary conditions in the time direction and twisted-mass reweighting have been adopted for the first time in a large-scale project and in our analysis we demonstrated that pseudo-scalar spectral quantities and flow observables can be safely exctracted with percent and sub-percent precision respectively.

The sampling of the HMC algorithm in the region where the Dirac operator becomes singular is enhanced with a positive twisted-mass. In this situation the configurations have to be reweighted and we have discussed the difficulties which one might encounter in the computation of the reweighting factors. Nevertheless, for our choices of the twisted masses, the fluctuations of observables (particularly) sensitive to the fermionic modes are brought under control, without reducing their final precision.

Simulations with open BC cure the problem of topology freezing and are now feasible also below 0.05 fm, as autocorrelations are under control and show the expected scaling behavior with a^{-2}. With the set of ensembles analyzed in this thesis we have not been able to see the point where the topological charge becomes the slowest observable, but we expect future simulations at $a \approx 0.03\,\text{fm}$ to be able to finally prove (numerically) that the freezing problem is solved, also in presence of the fermion determinant.

We have analyzed the effects of the boundaries on the observables, which are particularly pronounced on coarse lattices, but we could identify plateaus for all observables without particular problems. As expected from the Transfer Matrix, we verified that boundary effects vanish towards the middle of the lattices, where vacuum expectation values can be computed, thus discarding 40-50% of the lattices only in a few worst cases and for observables particularly sensitive to the sea quark effects.

Finally we computed the lattice spacing from the pseudo-scalar decay constants. Given the choice of the original chiral trajectory ($\text{tr}M = const$), we have considered the combination of pion and kaon decay constants showing a mild dependence on the quark masses in NLO $SU(3)$ ChPT. Unfortunately, chiral symmetry breaking effects turned out to be more relevant than expected. Along our trajectories we found cutoff effects in the trace of the renormalized PCAC mass matrix beyond linear order in a, at $\beta = 3.4$. In general

we observed violations from 5 to 2%, which we decided to correct non-perturbatively by defining a new renormalization condition.

By shifting our measurements to a new chiral trajectory, defined by $y_{\pi\mathrm{K}} = \frac{1}{2}y_\pi^2 + y_\mathrm{K}^2 = const$, passing through the physical point, we fixed the sum of the renormalized quark masses, up to terms of order m_π^4 in ChPT, and removed the $O(a)$ effects, since y_π and y_K are not influenced by the $O(a)$ terms in the quark masses. To compute the shifts we had to rely on the estimate of the derivatives computed at $\beta = 3.46$ and at the symmetric point, where $m_\mathrm{ud} = m_\mathrm{s}$. At the level of accuracy that we reached, we showed that our assumptions on these derivatives are correct and therefore we computed the decay constants and t_0 along this line of constant physics. Unfortunately, the original (good) precision of our measurements deteriorated to 2-3% and, given the ensembles at our disposal at the moment, we have not been able to improve the situation.

From the pseudo-scalar decay constants shifted on the line of constant physics, we have computed the lattice spacing for our four values of the coupling, by performing chiral extrapolations. Using a simple Taylor expansion in the quark masses we have estimated the systematic uncertainties of our determination, which turned out to be below their statistical accuracy. We have verified that on the level of 1% statistical accuracy, the NLO $SU(3)$ ChPT predictions fail to describe the behavior of the pseudo-scalar decay constants that we considered. This is not extremely surprising since as soon as kaons are present (with masses around 450 MeV), the $SU(3)$ flavor symmetry is broken more badly compared to the case of up and down quarks alone and consequently the applicability of $SU(3)$ ChPT is even more questioned. We outlined many improvements, consistings both in new simulations and different quantities to measure, which could increase the accuracy of the pseudo-scalar decay constants corrected from $O(a)$ discretization effects. With these improvements, many applicable in the near future, further clarifications on the issues concerning the ChPT expansions will be also possible.

In the end, we have provided a scale with an accuracy of about 2% and in terms of this scale we have also determined t_0 at physical quark masses and in the continuum limit. Using two approaches and various fit functions, we have obtained for QCD with 2 degenerate light flavors and the strange quark field $\sqrt{8t_0} = 0.4122(78)\,\mathrm{fm}$. Our determination is in good agreement with the other calculation present in the literature (for $N_\mathrm{f} = 2+1$), performed by the BMW collaboration. At this point, new observables, more interesting from the physics point of view, can be computed from the CLS ensembles and extrapolated to the continuum limit using the reference scale that we provided in this thesis.

In addition to that, the pseudo-scalar decay constants, defining a hadronic renormalization scheme, can be used to compute the Λ parameter of QCD with three flavors. In

particular, at the symmetric point, where no additional extrapolations are needed, they can be used to convert the Λ parameter from a Schrödinger Functional renormalization scheme to the $\overline{\rm MS}$ scheme, as explained in the first Chapter. For this particular purpose, let us stress the importance (among the several improvements that we mentioned) of a direct simulation at $\beta = 3.55$ of a $L = 2.7\,\mathrm{fm}$ lattice. Due to the finite-volume corrections, this is the only point reducing the precision of $f_{\pi\mathrm{K}}^{\mathrm{sym}} L_{\mathrm{max}}$ in the continuum limit and direct simulations (with even less statistics than H200) would reduce the error by a factor $\sqrt{3}$. From the study pursued in this thesis, we estimate the contribution of $f_{\pi\mathrm{K}}^{\mathrm{sym}}$ to the error of the Λ parameter to be about 1%, by looking at the continuum extrapolation of $\sqrt{8t_0} f_{\pi\mathrm{K}}$ at degenerate quark masses. Together with the (presently) 2% uncertainty in

$$f_{\pi\mathrm{K}}^{\mathrm{phys}} / f_{\pi\mathrm{K}}^{\mathrm{sym}} = 0.939(18)\,, \tag{7.1}$$

there will be an about 2-3% uncertainty due to scale setting in the Λ-parameter. This is already a very good precision for this fundamental parameter of QCD.

Acknowledgments

The support, knowledge and help of many people contributed to the completion of this thesis. Firstly, I would like to thank my supervisor Rainer for the huge amount of time that he spent with me. His continuous encouragement throughout all my time in Berlin has been fundamental for the conclusion of this thesis.

Secondly I would like to thank Stefan. Working with him has been an exciting experience and I am grateful also to him for his infinite patience with me.

I thank all the people at DESY who contributed to create a really pleasant and nice environment. In particular I am indebted to Hubert, Stefano, Alberto, Fabio, Patrick, Piotr, Felix and Mattia for the great time that we had in Zeuthen and in Berlin. Thanks to all the members of the ALPHA collaboration for the many interesting discussions and projects that we had together. I am grateful also to Michele and Marco for our ongoing stimulating scientific collaboration and to Valentina, Lorenzo and Marco for the involvement in their project beyond Lattice QCD.

Finally, special thanks go to my family for the endless support and encouragement over the last years and to Veronica for her continuous confidence in me and patience, which have been essential for my scientific endeavors.

A Topology of Yang-Mills theories

In this Appendix we briefly sketch the basic concepts on the vacuum structure of Yang-Mills theories appearing in a few points of the thesis. We refer for a more rigorous treatment to 't Hooft's and Coleman's lectures [138, 139].

We start by listing a few relevant properties of the homotopy group and then we explain the presence of disconnected sectors in the field space of non-abelian gauge theories. Finally, we conclude with a comment on the fact that these sectors are labeled by the topological charge, which is integer-valued.

A.1 Homotopy group

Let us consider two manifolds $\mathcal{M}$ and $\mathcal{G}$. Given two mappings ϕ_1 and ϕ_2, with $\phi_i : \mathcal{M} \to \mathcal{G}$, they are defined *homotopic* if they are continuously deformable one into another. This is an equivalence relation and accordingly the set of all mappings $\phi : \mathcal{M} \to \mathcal{G}$ can be divided into *classes*.

Through the action between two equivalence classes we can construct the *homotopy group* $\pi_n(\mathcal{G})$, defined to be the set of homotopy classes of the mappings

$$\phi : S^n \to \mathcal{G} \,. \tag{A.1}$$

Note that we have restricted the choices of manifolds $\mathcal{M}$ to the n-spheres. The first homotopy group π_1 is called fundamental group and it basically counts the loops and holes of $\mathcal{G}$, e.g. $\pi_1(S^2) = 0$ since any closed loop on a 2-sphere can always be deformed to a point, while for a torus[1] $\pi_1(T^2) = \mathbb{Z}^2$. For our discussion we are interested in the theorem

$$\pi_n(S_n) = \mathbb{Z} \,, \quad \forall n \,. \tag{A.2}$$

A.2 n vacua

Consider the theory defined on a 4D torus $L_0 \times L_1 \times L_2 \times L_3$. Imposing the boundary conditions $A_\mu(x + \hat{\mu} L_\mu) = A_\mu(x)$ in all directions evidently constrains the gauge degrees

[1] The 2D Torus can be always mapped to $\mathbb{R}^2$ by identifying the points $(x_0, x_1) = (x_0 + 2\pi m, x_1 + 2\pi n)$, $m, n \in \mathbb{Z}$.

of freedom too much. In fact at least in one direction periodicity must be satisfied up to a gauge transformation $\Lambda(\vec{x})$

$$A_\mu(x + \hat{0}\, L_0) = \Lambda(\vec{x})\big[A_\mu(x) + \partial_\mu\big]\Lambda^\dagger(\vec{x})\,, \tag{A.3}$$

which can only depend on the three remaining coordinates. Let us consider the gauge group $SU(2)$. It can be parametrized as 3-sphere embeded in $\mathbb{R}^4$

$$U = a_0\mathbb{1} + ia_i\sigma^i\,, a_0^2 + \sum_i a_i^2 = 1 \quad \to \quad U \in SU(2) \sim S^3\,. \tag{A.4}$$

Therefore the gauge transformations $\Lambda(\vec{x})$ are continuous mappings

$$\Lambda : S^3 \to S^3\,, \quad \pi_3(S^3) = \mathbb{Z}\,, \tag{A.5}$$

which can be classified in classes labeled by integers, according to eq. (A.2). Hence periodic boundary conditions in all directions imply the presence of disconnected sectors. Using the embeddings of $SU(2)$ in $SU(N)$ groups ($N > 2$), the same conclusion can be drawn for them too.

The gauge transformations in eq. (A.5) correspond to solutions of minimal (finite) action. The latter are obtained if the field strength tensor vanishes at infinity, assuming now to have taken the infinite volume limit. Such configurations are not realized by $A_\mu = 0$ but a gauge transform of it, often called pure-gauges

$$A_\mu(x) = \Lambda(x)\partial_\mu\Lambda(x)\,. \tag{A.6}$$

Imposing the gauge condition $A_0 = 0$ eliminates[2] the dependence on x_0 of Λ, reproducing again the situation in eq. (A.5). Hence these configurations of minimal action, corresponding to the classical vacua of the theory, can not be continuously deformed one in another while maintaining the action finite.

With these few lines we have seen how the field space of non-abelian gauge theories is divided in disconnected sectors, labeled by integer numbers and separated by barriers of infinite action. In general, the solutions of the (classical) equations of motion are classified by an integer number, called the topological charge, and those with non-trivial topology (non-zero charge) are called *Instantons*. We leave this topic to the reader and we conclude this Appendix with a few comments on the charge.

[2]Note that a gauge transformation must preserve the gauge-fixing condition $A_0^\Lambda = \Lambda\big[A_0 + \partial_0\big]\Lambda^\dagger$, which means $\partial_0\Lambda = 0$.

A.3 Topological charge

Inside the group $SU(2) \sim S^3$ the following integral

$$\nu = -\frac{1}{24\pi^2} \int da_1 da_2 da_3 \, \mathrm{tr}\, \varepsilon^{ijk} U \partial_i U^\dagger U \partial_j U^\dagger U \partial_k U^\dagger \tag{A.7}$$

is invariant under continuous transformations of the group elements U. From its homotopic invariance we deduce that it is an integer number, corresponding to the sector of the given gauge-field configuration.

The topological charge Q in eq. (2.53) is equivalent to ν and consequently it is integer-valued as well. Firstly we note that it can be re-expressed as a total divergence

$$\mathrm{tr}\, F_{\mu\nu} \tilde{F}_{\mu\nu} = \partial_\mu K_\mu \tag{A.8}$$

of a local Chern-Simons current K_μ. Thanks to Stoke's theorem, the integral over the whole volume is replaced by an integral over the boundary Σ (with normal vector $\hat{n}^\mu$)

$$\int d^4x \, \mathrm{tr}\, F_{\mu\nu} \tilde{F}_{\mu\nu} = \int d\Sigma \hat{n}^\mu K_\mu \, . \tag{A.9}$$

Replacing the "pure-gauges" given in eq. (A.6) into K_μ concludes the proof that $Q = \nu$. Hence, given a gauge-field configuration, the topological charge computed from the space-time integral of $\mathrm{tr}\, F\tilde{F}$ labels the corresponding the sector and it is integer (with the appropriate normalization). Finally, we note from eq. (A.9) that the topological charge is completely fixed by the boundary conditions on the vector potential. This consideration is particularly interesting in light of the open boundary conditions defined in Chapter 3 and used throughout the thesis.

B Renormalization Factor Z_A

The finite renormalization factor Z_A, appearing in the definition of the pseudo-scalar decay constants, is generally computed through Ward Identities [39]. The method adapted in Refs. [140, 141] to the Schrödinger Functional, has been recently applied to compute Z_A for the action (and number of flavors) that we used [142]. These computations involve four-point functions which are usually more noisy than the corresponding two-point correlators, often leading to few percent accuracy (given the level of statistics which is reached by nowadays calculations).

In the last years, the Schrödinger Functional has been extended by the introduction of new boundary conditions, which define the so-called Chirally-Rotated Schrödinger Functional [28, 29]. Within this setup, the renormalization factor Z_A is obtained only from two-point functions. This is one of the reasons why the results of Z_A turn out to be much more precise than the standard SF, well below the percent level. We would like to thank Mattia Dalla Brida and Tomasz Korzec for sharing un-published results on the computation of Z_A with 2+1 $O(a)$-improved Wilson fermions.

β	Z_A
3.4	0.7547(3)
3.46	0.7608(2)
3.55	0.7685(4)
3.7	0.7832(2)

Table B.1: The values of Z_A at $\beta = 3.46$ have been obtained from the fit in eq. (B.1), while the other three numbers have been computed from indepedent simulations performed exactly at those values of β and (approximately) zero quark masses. The method, developed and presented in Ref. [143], has been tested in the two-flavor theory and the values that we show above are un-published results for the 2+1 case.

In Refs. [144, 143] the full computation is described in the $N_{\rm f} = 2$ case and two definitions of Z_A are tested, called Z_A^g and Z_A^l, to check for the size of lattice artifacts. In this thesis we use the values corresponding to Z_A^l, which exhibits smaller scaling violations according to Ref. [144]. Note that only the two light quarks are "chirally-rotated", while the third (strange) quark field is treated with the RHMC algorithm and satisfies the standard SF boundary conditions.

We fit the results of the Chirally-Rotated SF with the following functional form

$$Z_A(g_0) = 1 - 0.090491 g_0^2 + p_0 g_0^4 + p_1 g_0^6 \tag{B.1}$$

and we obtain $p_0 = -0.0170(14)$ and $p_1 = -0.00596(83)$. To describe the SF data points we use a Padé fit, as in Ref. [142], with the one-loop coefficient fixed to the known perturbative value

$$Z_A(g_0) = \frac{1 + (p_2 - 0.090491) g_0^2 + p_3 g_0^4}{1 + p_2 g_0^2}\,. \tag{B.2}$$

From the fit we obtain $p_2 = -0.0424(19)$ and $p_3 = 0.0108(12)$. With respect to Ref. [116], the one-loop coefficent that we quote is much more precise. Indeed, it comes from a new computation performed by P. Vilaseca and M.Dalla Brida, who we thank for sharing (yet) un-published numbers. In Figure B.1 we plot the results obtained from the standard and the Chirally-Rotated Schrödinger Functional. The values of Z_A that we use throughout the thesis are also given in Table B.1.

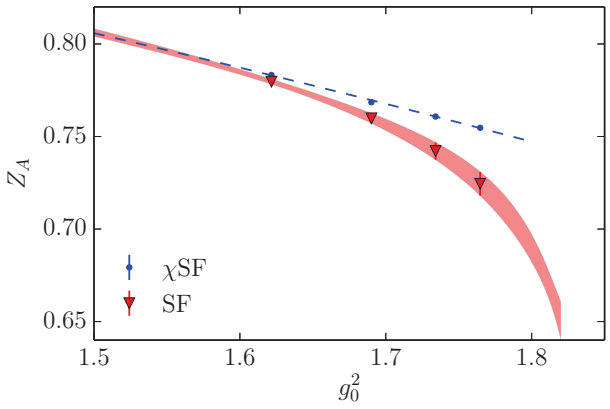

Figure B.1: Plot of the finite renormalization factor Z_A as a function of g_0^2 obtained from the standard SF [142] and un-published results by M.Dalla Brida and T.Korzec with the Chirally-Rotated SF. For an explanation of the method based on chirally-rotated SF see Ref. [143]. The points corresponding to the SF method have been obtained from the fit function described in the text and are plotted for (visual) comparison between the two methods. In the original publication, Ref. [142], Z_A has been measured for values of g_0 different from those corresponding to the SF points.

Bibliography

[1] F. Englert and R. Brout, *Broken Symmetry and the Mass of Gauge Vector Mesons*, *Phys.Rev.Lett.* **13** (1964) 321–323.

[2] P. W. Higgs, *Broken Symmetries and the Masses of Gauge Bosons*, *Phys.Rev.Lett.* **13** (1964) 508–509.

[3] P. W. Higgs, *Broken symmetries, massless particles and gauge fields*, *Phys.Lett.* **12** (1964) 132–133.

[4] **ATLAS** Collaboration, G. Aad et al., *Observation of a new particle in the search for the Standard Model Higgs boson with the ATLAS detector at the LHC*, *Phys.Lett.* **B716** (2012) 1–29, [arXiv:1207.7214].

[5] **CMS** Collaboration, S. Chatrchyan et al., *Observation of a new boson at a mass of 125 GeV with the CMS experiment at the LHC*, *Phys.Lett.* **B716** (2012) 30–61, [arXiv:1207.7235].

[6] **ALPHA** Collaboration, S. Schaefer, R. Sommer, and F. Virotta, *Critical slowing down and error analysis in lattice QCD simulations*, *Nucl.Phys.* **B845** (2011) 93–119, [arXiv:1009.5228].

[7] R. Narayanan and H. Neuberger, *Infinite N phase transitions in continuum Wilson loop operators*, *JHEP* **0603** (2006) 064, [hep-th/0601210].

[8] M. Lüscher, *Properties and uses of the Wilson flow in lattice QCD*, *JHEP* **1008** (2010) 071, [arXiv:1006.4518].

[9] M. Bruno, S. Schaefer, and R. Sommer, *Topological susceptibility and the sampling of field space in $N_f = 2$ lattice QCD simulations*, *JHEP* **1408** (2014) 150, [arXiv:1406.5363].

[10] M. Lüscher and S. Schaefer, *Lattice QCD without topology barriers*, *JHEP* **1107** (2011) 036, [arXiv:1105.4749].

[11] M. Lüscher and S. Schaefer, *Lattice QCD with open boundary conditions and twisted-mass reweighting*, *Comput.Phys.Commun.* **184** (2013) 519–528, [arXiv:1206.2809].

[12] M. Bruno, D. Djukanovic, G. P. Engel, A. Francis, G. Herdoiza, et al., *Simulation of QCD with $N_f = 2 + 1$ flavors of non-perturbatively improved Wilson fermions*, *JHEP* **1502** (2015) 043, [arXiv:1411.3982].

[13] R. Sommer, *Introduction to Non-perturbative Heavy Quark Effective Theory*, pp. 517–590, Modern perspectives in lattice QCD: Quantum field theory and high performance computing. Proceedings, International School, 93rd Session, Les Houches, France, August 3-28, 2009, 2010. arXiv:1008.0710.

[14] **ALPHA** Collaboration, M. Bruno, J. Finkenrath, F. Knechtli, B. Leder, and R. Sommer, *Effects of Heavy Sea Quarks at Low Energies*, *Phys.Rev.Lett.* **114** (2015), no. 10 102001, [arXiv:1410.8374].

[15] J. Callan, Curtis G., *Broken scale invariance in scalar field theory*, *Phys.Rev.* **D2** (1970) 1541–1547.

[16] K. Symanzik, *Small distance behavior in field theory and power counting*, *Commun.Math.Phys.* **18** (1970) 227–246.

[17] D. J. Gross and F. Wilczek, *Ultraviolet Behavior of Nonabelian Gauge Theories*, *Phys.Rev.Lett.* **30** (1973) 1343–1346.

[18] H. D. Politzer, *Reliable Perturbative Results for Strong Interactions?*, *Phys.Rev.Lett.* **30** (1973) 1346–1349.

[19] R. Sommer, *A New way to set the energy scale in lattice gauge theories and its applications to the static force and alpha-s in SU(2) Yang-Mills theory*, *Nucl.Phys.* **B411** (1994) 839–854, [hep-lat/9310022].

[20] C. W. Bernard, T. Burch, K. Orginos, D. Toussaint, T. A. DeGrand, et al., *The Static quark potential in three flavor QCD*, *Phys.Rev.* **D62** (2000) 034503, [hep-lat/0002028].

[21] R. Sommer, *Scale setting in lattice QCD*, *PoS* **LATTICE2013** (2014) 015, [arXiv:1401.3270].

[22] M. Lüscher, P. Weisz, and U. Wolff, *A Numerical method to compute the running coupling in asymptotically free theories*, *Nucl.Phys.* **B359** (1991) 221–243.

[23] A. Gonzalez Arroyo and C. Korthals Altes, *The Spectrum of Yang-Mills Theory in a Small Twisted Box*, *Nucl.Phys.* **B311** (1988) 433.

[24] S. Sint, *On the Schrodinger functional in QCD*, *Nucl.Phys.* **B421** (1994) 135–158, [hep-lat/9312079].

[25] M. Lüscher, S. Sint, R. Sommer, and P. Weisz, *Chiral symmetry and O(a) improvement in lattice QCD*, *Nucl.Phys.* **B478** (1996) 365–400, [hep-lat/9605038].

[26] K. Symanzik, *Schrodinger Representation and Casimir Effect in Renormalizable Quantum Field Theory*, *Nucl.Phys.* **B190** (1981) 1.

[27] M. Lüscher, R. Narayanan, P. Weisz, and U. Wolff, *The Schrodinger functional: A Renormalizable probe for nonAbelian gauge theories*, *Nucl.Phys.* **B384** (1992) 168–228, [hep-lat/9207009].

[28] S. Sint, *The Schrodinger functional with chirally rotated boundary conditions*, *PoS* **LAT2005** (2006) 235, [hep-lat/0511034].

[29] S. Sint, *The Chirally rotated Schródinger functional with Wilson fermions and automatic O(a) improvement*, *Nucl.Phys.* **B847** (2011) 491–531, [arXiv:1008.4857].

[30] P. Weisz, *Renormalization and lattice artifacts*, pp. 93–160, Modern perspectives in lattice QCD: Quantum field theory and high performance computing. Proceedings, International School, 93rd Session, Les Houches, France, August 3-28, 2009, 2010. arXiv:1004.3462.

[31] M. Lüscher, *Advanced lattice QCD*, pp. 229–280, Probing the standard model of particle interactions. Proceedings, Summer School in Theoretical Physics, NATO Advanced Study Institute, 68th session, Les Houches, France, July 28-September 5, 1997. Pt. 1, 2, 1998. hep-lat/9802029.

[32] R. Sommer, *Non-perturbative QCD: Renormalization, O(a)-improvement and matching to Heavy Quark Effective Theory*, Workshop on Perspectives in Lattice QCD, 2006. hep-lat/0611020.

[33] S. Sint, *Lattice QCD with a chiral twist*, Workshop on Perspectives in Lattice QCD, 2007. hep-lat/0702008.

[34] K. G. Wilson, *Confinement of Quarks*, *Phys.Rev.* **D10** (1974) 2445–2459.

[35] H. B. Nielsen and M. Ninomiya, *No Go Theorem for Regularizing Chiral Fermions*, *Phys.Lett.* **B105** (1981) 219.

[36] J. C. Ward, *An Identity in Quantum Electrodynamics*, *Phys.Rev.* **78** (1950) 182.

[37] Y. Takahashi, *On the generalized Ward identity*, *Nuovo Cim.* **6** (1957) 371.

[38] K. Fujikawa, *Path Integral Measure for Gauge Invariant Fermion Theories*, *Phys.Rev.Lett.* **42** (1979) 1195–1198.

[39] M. Bochicchio, L. Maiani, G. Martinelli, G. C. Rossi, and M. Testa, *Chiral Symmetry on the Lattice with Wilson Fermions*, *Nucl.Phys.* **B262** (1985) 331.

[40] K. Symanzik, *CUTOFF DEPENDENCE IN LATTICE phi**4 in four-dimensions THEORY*, p. 0313, Cargèse Lectures, 1979.

[41] K. Symanzik, *SOME TOPICS IN QUANTUM FIELD THEORY.* Mathematical Problems In Theoretical Physics, 1981.

[42] T. Appelquist and J. Carazzone, *Infrared Singularities and Massive Fields*, *Phys.Rev.* **D11** (1975) 2856.

[43] M. Lüscher and P. Weisz, *On-Shell Improved Lattice Gauge Theories*, *Commun.Math.Phys.* **97** (1985) 59.

[44] M. Lüscher and P. Weisz, *Computation of the Action for On-Shell Improved Lattice Gauge Theories at Weak Coupling*, *Phys.Lett.* **B158** (1985) 250.

[45] B. Sheikholeslami and R. Wohlert, *Improved continuum limit lattice action for QCD with Wilson fermions*, *Nucl. Phys.* **B259** (1985) 572.

[46] M. Lüscher, S. Sint, R. Sommer, and P. Weisz, *Chiral symmetry and O(a) improvement in lattice QCD*, *Nucl. Phys.* **B478** (1996) 365–400, [hep-lat/9605038].

[47] T. Bhattacharya, R. Gupta, W. Lee, S. R. Sharpe, and J. M. Wu, *Improved bilinears in lattice QCD with non-degenerate quarks*, *Phys.Rev.* **D73** (2006) 034504, [hep-lat/0511014].

[48] S. Sint and R. Sommer, *The Running coupling from the QCD Schrodinger functional: A One loop analysis*, *Nucl.Phys.* **B465** (1996) 71–98, [hep-lat/9508012].

[49] R. Frezzotti, P. A. Grassi, S. Sint, and P. Weisz, *A Local formulation of lattice QCD without unphysical fermion zero modes*, *Nucl.Phys.Proc.Suppl.* **83** (2000) 941–946, [hep-lat/9909003].

[50] **Alpha** Collaboration, R. Frezzotti, P. A. Grassi, S. Sint, and P. Weisz, *Lattice QCD with a chirally twisted mass term*, *JHEP* **0108** (2001) 058, [hep-lat/0101001].

[51] M. Lüscher, *Construction of a Selfadjoint, Strictly Positive Transfer Matrix for Euclidean Lattice Gauge Theories*, *Commun.Math.Phys.* **54** (1977) 283.

[52] **ALPHA** Collaboration, R. Frezzotti, S. Sint, and P. Weisz, *O(a) improved twisted mass lattice QCD*, *JHEP* **0107** (2001) 048, [hep-lat/0104014].

[53] J. B. Kogut and L. Susskind, *Hamiltonian Formulation of Wilson's Lattice Gauge Theories*, *Phys.Rev.* **D11** (1975) 395–408.

[54] D. B. Kaplan, *A Method for simulating chiral fermions on the lattice*, *Phys.Lett.* **B288** (1992) 342–347, [hep-lat/9206013].

[55] Y. Shamir, *Chiral fermions from lattice boundaries*, *Nucl.Phys.* **B406** (1993) 90–106, [hep-lat/9303005].

[56] V. Furman and Y. Shamir, *Axial symmetries in lattice QCD with Kaplan fermions*, *Nucl.Phys.* **B439** (1995) 54–78, [hep-lat/9405004].

[57] R. Narayanan and H. Neuberger, *A Construction of lattice chiral gauge theories*, *Nucl.Phys.* **B443** (1995) 305–385, [hep-th/9411108].

[58] R. Narayanan and H. Neuberger, *Chiral fermions on the lattice*, *Phys.Rev.Lett.* **71** (1993) 3251–3254, [hep-lat/9308011].

[59] P. H. Ginsparg and K. G. Wilson, *A Remnant of Chiral Symmetry on the Lattice*, *Phys.Rev.* **D25** (1982) 2649.

[60] H. Neuberger, *Exactly massless quarks on the lattice*, *Phys.Lett.* **B417** (1998) 141–144, [hep-lat/9707022].

[61] H. Neuberger, *More about exactly massless quarks on the lattice*, *Phys.Lett.* **B427** (1998) 353–355, [hep-lat/9801031].

[62] H. Neuberger, *Vector - like gauge theories with almost massless fermions on the lattice*, *Phys.Rev.* **D57** (1998) 5417–5433, [hep-lat/9710089].

[63] M. Lüscher, *Exact chiral symmetry on the lattice and the Ginsparg-Wilson relation*, *Phys.Lett.* **B428** (1998) 342–345, [hep-lat/9802011].

[64] P. Hernandez, K. Jansen, and M. Lüscher, *Locality properties of Neuberger's lattice Dirac operator*, *Nucl.Phys.* **B552** (1999) 363–378, [hep-lat/9808010].

[65] W. A. Bardeen, *Anomalous Ward identities in spinor field theories*, *Phys.Rev.* **184** (1969) 1848–1857.

[66] S. L. Adler and W. A. Bardeen, *Absence of higher order corrections in the anomalous axial vector divergence equation*, *Phys.Rev.* **182** (1969) 1517–1536.

[67] M. Atiyah and I. Singer, *The Index of elliptic operators. 5.*, *Annals Math.* **93** (1971) 139–149.

[68] P. Hasenfratz, V. Laliena, and F. Niedermayer, *The Index theorem in QCD with a finite cutoff*, *Phys.Lett.* **B427** (1998) 125–131, [hep-lat/9801021].

[69] M. Lüscher, *Topology of Lattice Gauge Fields*, *Commun.Math.Phys.* **85** (1982) 39.

[70] L. Giusti, G. Rossi, M. Testa, and G. Veneziano, *The U(A)(1) problem on the lattice with Ginsparg-Wilson fermions*, *Nucl.Phys.* **B628** (2002) 234–252, [hep-lat/0108009].

[71] L. Giusti, G. Rossi, and M. Testa, *Topological susceptibility in full QCD with Ginsparg-Wilson fermions*, *Phys.Lett.* **B587** (2004) 157–166, [hep-lat/0402027].

[72] M. Lüscher, *Topological effects in QCD and the problem of short distance singularities*, *Phys.Lett.* **B593** (2004) 296–301, [hep-th/0404034].

[73] M. Lüscher and P. Weisz, *Perturbative analysis of the gradient flow in non-abelian gauge theories*, *JHEP* **1102** (2011) 051, [arXiv:1101.0963].

[74] M. Lüscher, *Chiral symmetry and the Yang–Mills gradient flow*, *JHEP* **1304** (2013) 123, [arXiv:1302.5246].

[75] S. Borsanyi, S. Dürr, Z. Fodor, C. Hoelbling, S. D. Katz, et al., *High-precision scale setting in lattice QCD*, *JHEP* **1209** (2012) 010, [arXiv:1203.4469].

[76] M. Müller-Preussker, *Recent results on topology on the lattice (in memory of Pierre van Baal)*, arXiv:1503.0125.

[77] N. Metropolis, A. Rosenbluth, M. Rosenbluth, A. Teller, and E. Teller, *Equation of state calculations by fast computing machines*, *J.Chem.Phys.* **21** (1953) 1087–1092.

[78] W. Hastings, *Monte Carlo Sampling Methods Using Markov Chains and Their Applications*, *Biometrika* **57** (1970) 97–109.

[79] S. Duane, A. Kennedy, B. Pendleton, and D. Roweth, *Hybrid Monte Carlo*, *Phys.Lett.* **B195** (1987) 216–222.

[80] I. P. Omelyan, I. M. Mryglod, and R. Folk, *Symplectic analytically integrable decomposition algorithms: classification, derivation, and application to molecular dynamics, quantum and celestial mechanics simulations*, *Computer Physics Communications* **151** (2003), no. 3 272 – 314.

[81] J. Sexton and D. Weingarten, *Hamiltonian evolution for the hybrid Monte Carlo algorithm*, *Nucl.Phys.* **B380** (1992) 665–678.

[82] D. Weingarten and D. Petcher, *Monte Carlo Integration for Lattice Gauge Theories with Fermions*, *Phys.Lett.* **B99** (1981) 333.

[83] M. Lüscher, *Computational Strategies in Lattice QCD*. Les Houches Summer School: Session 93: Modern perspectives in lattice QCD: Quantum field theory and high performance computing, 2010.

[84] M. Hasenbusch, *Speeding up the hybrid Monte Carlo algorithm for dynamical fermions*, *Phys.Lett.* **B519** (2001) 177–182, [hep-lat/0107019].

[85] M. Hasenbusch and K. Jansen, *Speeding up lattice QCD simulations with clover improved Wilson fermions*, *Nucl.Phys.* **B659** (2003) 299–320, [hep-lat/0211042].

[86] M. Lüscher, *Schwarz-preconditioned HMC algorithm for two-flavour lattice QCD*, *Comput.Phys.Commun.* **165** (2005) 199–220, [hep-lat/0409106].

[87] S. Schaefer, *Status and challenges of simulations with dynamical fermions*, *PoS* **LATTICE2012** (2012) 001, [arXiv:1211.5069].

[88] M. Clark, B. Joo, A. Kennedy, and P. Silva, *Improving dynamical lattice QCD simulations through integrator tuning using Poisson brackets and a force-gradient integrator*, *Phys.Rev.* **D84** (2011) 071502, [arXiv:1108.1828].

[89] A. Kennedy, P. Silva, and M. Clark, *Shadow Hamiltonians, Poisson Brackets, and Gauge Theories*, *Phys.Rev.* **D87** (2013), no. 3 034511, [arXiv:1210.6600].

[90] N. Madras and A. D. Sokal, *The Pivot algorithm: a highly efficient Monte Carlo method for selfavoiding walk*, *J.Statist.Phys.* **50** (1988) 109–186.

[91] **ALPHA** Collaboration, U. Wolff, *Monte Carlo errors with less errors*, *Comput.Phys.Commun.* **156** (2004) 143–153, [hep-lat/0306017].

[92] A. Kennedy and B. Pendleton, *Cost of the generalized hybrid Monte Carlo algorithm for free field theory*, *Nucl.Phys.* **B607** (2001) 456–510, [hep-lat/0008020].

[93] M. Lüscher and S. Schaefer, *Non-renormalizability of the HMC algorithm*, *JHEP* **1104** (2011) 104, [arXiv:1103.1810].

[94] J. Zinn-Justin, *Renormalization and Stochastic Quantization*, *Nucl.Phys.* **B275** (1986) 135.

[95] A. M. Horowitz, *A Generalized guided Monte Carlo algorithm*, *Phys.Lett.* **B268** (1991) 247–252.

[96] G. P. Engel and S. Schaefer, *Testing trivializing maps in the Hybrid Monte Carlo algorithm*, *Comput.Phys.Commun.* **182** (2011) 2107–2114, [arXiv:1102.1852].

[97] M. Lüscher, *The Schrodinger functional in lattice QCD with exact chiral symmetry*, *JHEP* **0605** (2006) 042, [hep-lat/0603029].

[98] M. Lüscher and F. Palombi, *Fluctuations and reweighting of the quark determinant on large lattices*, *PoS* **LATTICE2008** (2008) 049, [arXiv:0810.0946].

[99] A. Ferrenberg and R. Swendsen, *New Monte Carlo Technique for Studying Phase Transitions*, *Phys.Rev.Lett.* **61** (1988) 2635–2638.

[100] A. Hasenfratz, R. Hoffmann, and S. Schaefer, *Reweighting towards the chiral limit*, *Phys.Rev.* **D78** (2008) 014515, [arXiv:0805.2369].

[101] M. Clark and A. Kennedy, *Accelerating dynamical fermion computations using the rational hybrid Monte Carlo (RHMC) algorithm with multiple pseudofermion fields*, *Phys.Rev.Lett.* **98** (2007) 051601, [hep-lat/0608015].

[102] A. Kennedy, I. Horvath, and S. Sint, *A New exact method for dynamical fermion computations with nonlocal actions*, *Nucl.Phys.Proc.Suppl.* **73** (1999) 834–836, [hep-lat/9809092].

[103] W. Bietenholz, V. Bornyakov, N. Cundy, M. Göckeler, R. Horsley, et al., *Tuning the strange quark mass in lattice simulations*, *Phys.Lett.* **B690** (2010) 436–441, [arXiv:1003.1114].

[104] S. Aoki, Y. Aoki, C. Bernard, T. Blum, G. Colangelo, et al., *Review of lattice results concerning low-energy particle physics*, *Eur.Phys.J.* **C74** (2014), no. 9 2890, [arXiv:1310.8555].

[105] A. Ramos and S. Sint, *On $O(a^2)$ effects in gradient flow observables*, arXiv:1411.6706.

[106] M. Lüscher, *Signatures of unstable particles in finite volume*, *Nucl.Phys.* **B364** (1991) 237–254.

[107] **UKQCD** Collaboration, C. Michael and J. Peisa, *Maximal variance reduction for stochastic propagators with applications to the static quark spectrum*, *Phys.Rev.* **D58** (1998) 034506, [hep-lat/9802015].

[108] **ALPHA** Collaboration, M. Guagnelli, J. Heitger, R. Sommer, and H. Wittig, *Hadron masses and matrix elements from the QCD Schrodinger functional*, *Nucl.Phys.* **B560** (1999) 465–481, [hep-lat/9903040].

[109] M. Lüscher, *Volume Dependence of the Energy Spectrum in Massive Quantum Field Theories. 1. Stable Particle States*, *Commun.Math.Phys.* **104** (1986) 177.

[110] M. Lüscher, *Volume Dependence of the Energy Spectrum in Massive Quantum Field Theories. 2. Scattering States*, *Commun.Math.Phys.* **105** (1986) 153–188.

[111] S. Weinberg, *Pion scattering lengths*, *Phys.Rev.Lett.* **17** (1966) 616–621.

[112] G. Colangelo, J. Gasser, and H. Leutwyler, *$\pi\pi$ scattering*, *Nucl.Phys.* **B603** (2001) 125–179, [hep-ph/0103088].

[113] M. Bruno, P. Korcyl, T. Korzec, S. Lottini, and S. Schaefer, *On the extraction of spectral quantities with open boundary conditions*, *PoS* **LATTICE2014** (2014) 089, [arXiv:1411.5207].

[114] R. Sommer and S. Lottini, "Data analysis in lattice field theory." https://indico.desy.de/conferenceDisplay.py?confId=9420, 2014. Lattice Practices.

[115] B. Bunk. Private communication with Sommer R.

[116] Y. Taniguchi and A. Ukawa, *Perturbative calculation of improvement coefficients to O(g**2a) for bilinear quark operators in lattice QCD*, *Phys.Rev.* **D58** (1998) 114503, [hep-lat/9806015].

[117] J. Bulava, M. Della Morte, J. Heitger, and C. Wittemeier, *Non-perturbative improvement of the axial current in $N_f = 3$ lattice QCD with Wilson fermions and tree-level improved gauge action*, arXiv:1502.0499.

[118] S. Aoki, K.-i. Nagai, Y. Taniguchi, and A. Ukawa, *Perturbative renormalization factors of bilinear quark operators for improved gluon and quark actions in lattice QCD*, *Phys.Rev.* **D58** (1998) 074505, [hep-lat/9802034].

[119] P. Fritzsch, F. Knechtli, B. Leder, M. Marinkovic, S. Schaefer, et al., *The strange quark mass and Lambda parameter of two flavor QCD*, *Nucl.Phys.* **B865** (2012) 397–429, [arXiv:1205.5380].

[120] O. Bär and M. Golterman, *Excited-state contribution to the axial-vector and pseudoscalar correlators with two extra pions*, *Phys.Rev.* **D87** (2013), no. 1 014505, [arXiv:1209.2258].

[121] C. Vafa and E. Witten, *Restrictions on Symmetry Breaking in Vector-Like Gauge Theories*, *Nucl.Phys.* **B234** (1984) 173.

[122] S. Weinberg, *Phenomenological Lagrangians*, *Physica* **A96** (1979) 327.

[123] M. Golterman, *Applications of chiral perturbation theory to lattice QCD*, pp. 423–515, Modern perspectives in lattice QCD: Quantum field theory and high performance computing. Proceedings, International School, 93rd Session, Les Houches, France, August 3-28, 2009, 2009. arXiv:0912.4042.

[124] S. Sharpe, *Applications of Chiral Perturbation theory to lattice QCD*, hep-lat/0607016.

[125] J. Gasser and H. Leutwyler, *Chiral Perturbation Theory to One Loop*, *Annals Phys.* **158** (1984) 142.

[126] J. Gasser and H. Leutwyler, *Chiral Perturbation Theory: Expansions in the Mass of the Strange Quark*, *Nucl.Phys.* **B250** (1985) 465.

[127] J. Gasser and H. Leutwyler, *Light Quarks at Low Temperatures*, *Phys.Lett.* **B184** (1987) 83.

[128] G. Colangelo, S. Dürr, and C. Haefeli, *Finite volume effects for meson masses and decay constants*, *Nucl.Phys.* **B721** (2005) 136–174, [hep-lat/0503014].

[129] **Budapest-Marseille-Wuppertal** Collaboration, S. Dürr et al., *Lattice QCD at the physical point meets SU(2) chiral perturbation theory*, *Phys.Rev.* **D90** (2014), no. 11 114504, [arXiv:1310.3626].

[130] **JLQCD, TWQCD** Collaboration, J. Noaki et al., *Convergence of the chiral expansion in two-flavor lattice QCD*, *Phys.Rev.Lett.* **101** (2008) 202004, [arXiv:0806.0894].

[131] H. Wittig, *Low-energy particle physics and chiral extrapolations*, *PoS* **LATTICE2011** (2011) 025, [arXiv:1201.4774].

[132] A. Roessl, *Pion kaon scattering near the threshold in chiral SU(2) perturbation theory*, *Nucl.Phys.* **B555** (1999) 507–539, [hep-ph/9904230].

[133] S. R. Sharpe and J. Singleton, Robert L., *Spontaneous flavor and parity breaking with Wilson fermions*, *Phys.Rev.* **D58** (1998) 074501, [hep-lat/9804028].

[134] O. Bär, G. Rupak, and N. Shoresh, *Chiral perturbation theory at O(a**2) for lattice QCD*, *Phys.Rev.* **D70** (2004) 034508, [hep-lat/0306021].

[135] **ALPHA** Collaboration, S. Lottini, *Chiral behaviour of the pion decay constant in $N_f = 2$ QCD*, *PoS* **LATTICE2013** (2014) 315, [arXiv:1311.3081].

[136] O. Bär and M. Golterman, *Chiral perturbation theory for gradient flow observables*, *Phys.Rev.* **D89** (2014), no. 3 034505, [arXiv:1312.4999].

[137] **ALPHA** Collaboration, M. Bruno and R. Sommer, *On the N_f-dependence of gluonic observables*, *PoS* **LATTICE2013** (2014) 321, [arXiv:1311.5585].

[138] S. R. Coleman, *The Uses of Instantons*, *Subnucl.Ser.* **15** (1979) 805.

[139] G. 't Hooft, *Monopoles, instantons and confinement*, hep-th/0010225.

[140] M. Luscher, S. Sint, R. Sommer, and H. Wittig, *Nonperturbative determination of the axial current normalization constant in O(a) improved lattice QCD*, *Nucl.Phys.* **B491** (1997) 344–364, [hep-lat/9611015].

[141] M. Della Morte, R. Hoffmann, F. Knechtli, R. Sommer, and U. Wolff, *Non-perturbative renormalization of the axial current with dynamical Wilson fermions*, *JHEP* **0507** (2005) 007, [hep-lat/0505026].

[142] J. Bulava, M. Della Morte, J. Heitger, and C. Wittemeier, *Non-perturbative improvement and renormalization of the axial current in $N_f = 3$ lattice QCD*, *PoS* **LATTICE2014** (2014) 283, [arXiv:1502.0777].

[143] M. Dalla Brida and S. Sint, *A dynamical study of the chirally rotated Schrödinger functional in QCD*, arXiv:1412.8022.

[144] M. Dalla Brida, "A dynamical study of the chirally rotated Schrödinger functional in lattice QCD." PhD thesis. Trinity College Dublin, 2015.

Eigenständigkeitserklärung

Ich erkläre, dass ich die vorliegende Arbeit selbständig und nur unter Verwendung der angegebenen Literatur und Hilfsmittel angefertigt habe.

Mattia Bruno
Berlin, den 26 May 2015

List of Publications

[1] M. Bruno, D. Djukanovic, G. P. Engel, A. Francis, G. Herdoiza, et al., *Simulation of QCD with $N_f = 2 + 1$ flavors of non-perturbatively improved Wilson fermions*, *JHEP* **1502** (2015) 043, [arXiv:1411.3982].

[2] **ALPHA** Collaboration, M. Bruno, J. Finkenrath, F. Knechtli, B. Leder, and R. Sommer, *Effects of Heavy Sea Quarks at Low Energies*, *Phys.Rev.Lett.* **114** (2015), no. 10 102001, [arXiv:1410.8374].

[3] M. Bruno, M. Caselle, M. Panero, and R. Pellegrini, *Exceptional thermodynamics: the equation of state of G_2 gauge theory*, *JHEP* **1503** (2015) 057, [arXiv:1409.8305].

[4] **ALPHA** Collaboration, M. Bruno, S. Schaefer, and R. Sommer, *Topological susceptibility and the sampling of field space in $N_f = 2$ lattice QCD simulations*, *JHEP* **1408** (2014) 150, [arXiv:1406.5363].

[5] M. Bruno, P. Korcyl, T. Korzec, S. Lottini, and S. Schaefer, *On the extraction of spectral quantities with open boundary conditions*, *PoS* **LATTICE2014** (2014) 089, [arXiv:1411.5207].

[6] F. Knechtli, A. Athenodorou, M. Bruno, J. Finkenrath, B. Leder, et al., *Physical and cut-off effects of heavy sea quarks*, *PoS* **LATTICE2014** (2014) [arXiv:1411.1239].

[7] M. Bruno and R. Sommer, *On the N_f-dependence of gluonic observables*, *PoS* **LATTICE2013** (2013) 321, [arXiv:1311.5585].